N° d'ordre : 331/2021

UNIVERSITE SULTAN MOULAY SLIMANE

Faculté des Sciences et Techniques

Béni-Mellal

Centre d'Études Doctorales : Sciences et Techniques
Formation Doctorale : **Ressources Naturelles Environnement et santé**

THÈSE

Présentée par

Mlle Hafsa BOUAMRI

Pour l'obtention du grade de

Docteur

Spécialité ***:*** *Géologie*

Option ***: Hydrologie et Télédétection***

Investigating the effect of Radiation and Temperature-index Models to simulate Snowmelt and Snow Water Equivalent from local to basin scale in the Moroccan High Atlas

Soutenue le 02/ Avril /2021 à 15h devant la commission d'examen :

Dr. Abdelghani CHEHBOUNI	Directeur de Recherche, Institut de Recherche pour le développement, Montpellier, France	Président
Pr. Lhoussaine BOUCHAOU	Professeur, Faculté des Sciences, Agadir	Rapporteur
Pr. Adil SALHI	Professeur, Faculté des Sciences, Tétouan	Rapporteur
Dr. Yves TRAMBLAY	HDR, Institut de Recherche pour le développement, Université de Montpellier, France	Rapporteur
Pr. Lahoucine HANICH	Professeur, Faculté des Sciences et Techniques-Guéliz, Marrakech	Examinateur
Pr. Abdelkrim ARIOUA	Professeur, Faculté des Sciences et Techniques, Béni Mellal	Examinateur
Pr. Christophe KINNARD	Professeur, Université du Québec à Trois Rivières, Canada	Co-Directeur de thèse
Pr. Abdelghani BOUDHAR	Professeur, Faculté des Sciences et Techniques, Béni Mellal	Directeur de thèse

ACKNOWLEDGMENTS

First of all, I would like to thank my institutional supervisor, Professor Abdelghani BOUDHAR who guided me throughout my Ph.D thesis and allowed me to be her first Ph.D student. I am incredibly grateful for everything he has done in favor of my personal and intellectual growth, also for his constant encouragement to complete the research work.

A very special acknowledgment goes to my co-supervisor, Professor Christophe KINNARD from the University of Quebec in Trois-Rivieres (UQTR), the leader of the GlacioLAB research unit, with whom I worked closely, thank you for your guidance, support, and availability. Thank you for giving me the opportunity to be a member of your team, and to ensure my two fellowships in UQTR.

I would like to express my deepest appreciation to all my committee members for their motivation and for reviewing my thesis.

I would like also to thank LMI-TREMA for providing meteorological data.

Huge thanks are going also to my colleagues at both teams, (1) the GEVARET at University of Sultan Moulay Slimane in Morocco, for sharing their technical support and encouragement, and (2) the GlacioLAB at the University of Quebec in Trois-Rivieres (UQTR) for sharing their experience and knowledge, also for their kindness and motivation.

I would like to express my gratitude to my friends for their emotional support Nejwa, Sara, and Noor.

I really want to thank my family for their endless support, patience and love. “ Papa et Maman, je ne vous remercierai jamais pour tous vos efforts, sacrifices et prieres. C’est grace à vous que j’ai accoumpli ce travail. Je remercie tendrement ma chère sœur Hanane et mon cher frère Badr pour leurs soutien et amour. Que Dieu vous garde et vous protège! ”.

ABSTRACT

In the Moroccan High Atlas Mountains, snowpack constitutes a vital source of water for the surrounding population. Its melting plays an important role in the water balance by providing freshwater to irrigate large arid plains downstream, drinking water, and hydropower production. A good estimate of snowmelt contribution to runoff is, therefore, highly relevant for water management purposes. In this context, assessment of snowmelt and snow water equivalent (SWE) using modeling techniques provides useful guidance to decision-makers and managers about water budget calculation and runoff prediction.

Due to the large spatiotemporal variability of the seasonal snow cover and the lack of field observations, estimating snowmelt remains a challenging task. In this sense, the use of simple conceptual snow models combined with remote sensing data constitutes a useful approach for snow studies. In this thesis, four empirical snowmelt models were tested and compared to simulate snowmelt and snow water equivalent (SWE) at both scales: (i) local at Oukaimeden-SM station and (ii) spatial at Rheraya basin. These models are the classical temperature-index model (TI) and three enhanced temperature index models that respectively include the potential clear-sky direct radiation (HTI), the incoming solar radiation (ETI-A), and net solar radiation (ETI-B). The key aspects of the methodology implemented in this thesis include: (a) the use of different model calibration and validation approaches, (b) model parameter sensitivity analysis, (c) distribution of forcing meteorological data over the Rheraya basin through a combined interpolation method, (d) the merge of both Moderate-Resolution Imaging Spectroradiometer (MODIS) snow cover area (SCA) products (Terra and Aqua), (e) the sensibility analysis of SWE-SCA conversion threshold.

The results, at the local scale, revealed that snowmelt models enhanced with solar radiation outperformed the simple temperature-index (TI) model and were also more transferable between years, when model parameters were calibrated over a single year. However, model performances were more similar when models were calibrated for a longer period. At the basin scale, differences in model performance were overall small, as were the differences in basin averaged simulated SWE and melt rates. This occurs because topographically-induced variations in melt rates simulated by the enhanced models tend to average out, and the aggregation of model outputs to MODIS resolution, which suppresses key spatial variability related to solar radiation. This highlights the need for caution when using medium resolution satellite products to validate spatially distributed snow models, a widely used practice in snow hydrological modeling. Our results addresses central considerations about model performances, scale-dependent processes and model validation. This research should be of particular interest for the snow and hydrology communities.

Keywords: snowmelt, snow water equivalent (SWE), snow cover area (SCA), temperature-index models, solar radiation, MODIS, High Atlas, Morocco.

RÉSUMÉ

En montagnes du Haut Atlas Marocain, le manteau neigeux constitue une source d'eau vitale pour la population avoisinante. Sa fonte joue un rôle incontournable dans l'approvisionnement en eau; tout en fournissant de l'eau douce, pour l'irrigation des plaines arides en aval, de l'eau potable, et pour la production d'énergie hydroélectrique. Cependant, une bonne estimation de la contribution de la fonte des neiges au ruissellement est pertinente pour la gestion de l'eau. Dans ce contexte, l'évaluation de la fonte des neiges et de son équivalent en eau à l'aide des techniques de modélisation représente une approche utile pour le calcul du bilan hydrique ainsi que la prévision du ruissellement.

En raison de la grande variabilité spatiotemporelle de la couverture neigeuse et du manque d'observations sur le terrain, l'estimation de la fonte des neiges reste une tâche complexe. Dans ce sens, l'utilisation de modèles conceptuels simples de la neige combinée à des données de télédétection constitue une approche fructueuse pour les études de neiges. Dans cette thèse, quatre modèles empiriques de neige sont testés et comparés pour simuler la fonte et l'équivalent en eau de la neige (EEN) sur deux échelles : (i) local à la station Oukaimeden-SM et (ii) spatial sur le bassin de Rheraya. Ces modèles sont : le modèle classique d'indice de température (TI) et trois modèles d'indice de température amélioré qui incluent respectivement le rayonnement potentiel en ciel dégagé (HTI), le rayonnement solaire incident (ETI-A) et le rayonnement solaire net (ETI-B). Les principaux aspects de la méthodologie mise en œuvre dans cette thèse sont les suivants (a) l'utilisation de différentes approches de calibration et de validation des modèles, (b) l'analyse de la sensibilité des paramètres des modèles, (c) la distribution des données météorologiques de forçage sur le bassin de Rheraya par une méthode d'interpolation combinée, (d) la combinaison des deux produits de surfaces de neige 'Terra et Aqua' du spectroradiomètre imageur à résolution modérée (MODIS), (e) l'analyse de la sensibilité du seuil de conversion SWE-SCA.

Les résultats obtenus à l'échelle locale, soulignent que les modèles améliorés par le rayonnement solaire sont plus performants du simple modèle d'indice de température (TI), en outre, qu'ils sont plus transférables d'une année à l'autre, lorsque les paramètres du modèle sont calibrés sur une seule année. Toutefois, les performances de l'ensemble des modèles sont plutôt similaires, quand ils sont calibrés sur une période plus longue. À l'échelle du bassin, les différences de performance du modèle sont globalement faibles, tout comme les différences de l'équivalent en eau et des taux de fonte simulés moyen du bassin. Cela s'explique par le fait que les variations topographiques des taux de fonte simulées par les modèles améliorés ont tendance à s'estomper, en plus de l'agrégation des sorties des modèles à la résolution MODIS, qui supprime la variabilité spatiale liée au rayonnement solaire. Cela souligne la nécessité de faire preuve de prudence lors de l'utilisation de produits satellitaires à moyenne résolution pour valider des modèles de neige spatialement distribués, une pratique largement utilisée dans la modélisation hydrologique de la neige. Nos résultats abordent des considérations centrales sur les performances des modèles, les

processus dépendant de l'échelle et la validation des modèles. Cette recherche devrait alors présenter un intérêt particulier pour les communautés de la neige et de l'hydrologie.

Mots clés : fonte de neige, équivalent en eau de neige (EEN), surfaces enneigées, modèles d'indice de température, rayonnement solaire, MODIS, Haut Atlas, MAROC.

ملخص

في جبال الأطلس الكبير المغربية، تشكل الثلوج مصدرًا حيويًا للمياه للسكان المحيطين. بحيث يلعب ذوبانه دورًا مهمًا في توازن المياه من خلال توفير المياه العذبة لري السهول القاحلة الكبيرة في اتجاه مجرى النهر، ومياه الشرب، وإنتاج الطاقة الكهرومائية. لذلك فإن التقدير الجيد لمساهمة ذوبان الجليد في الجريان السطحي له صلة وثيقة بأغراض إدارة المياه. في هذا السياق، يوفر تقييم ذوبان الجليد ومكافئ مياه الثلج (SWE) باستخدام تقنيات النمذجة إرشادات مفيدة لصانعي القرار والمديرين حول حساب ميزانية المياه وتنبؤ الجريان.

نظرًا للتغير الزماني والمكاني الكبير للغطاء الثلجي الموسمي ونقص الملاحظات الميدانية، فإن تقدير عمليات ذوبان الجليد تظل مهمة صعبة. وفي هدا المعنى، فإن استخدام نماذج مفاهيمية بسيطة للثلج مع بيانات الاستشعار عن بعد يشكل نهجًا مفيدًا لدراسات الثلوج. في هذه الأطروحة، تم اختبار أربعة نماذج ذوبان الجليد التجريبية ومقارنتها لمحاكاة ذوبان الجليد ومكافئ ماء الثلج (SWE) على كلا المقياسين: (1) محلي في محطة Oukaimeden-SM و (2) فضائي في حوض Rheraya. هذه النماذج هي نموذج مؤشر درجة الحرارة الكلاسيكي (TI) وثلاثة نماذج مُحسّنة لمؤشر درجة الحرارة والتي تشمل على التوالي إشعاع السماء الصافية المباشر المحتمل (HTI)، والإشعاع الشمسي الوارد (ETI-A)، والإشعاع الشمسي الصافي (ETI-B). تشمل الجوانب الرئيسية للمنهجية المطبقة في هذه الأطروحة ما يلي: (أ) استخدام أساليب المعايرة والتحقق من النموذج المختلفة، (ب) تحليل حساسية معلمة النموذج، (ج) توزيع بيانات الأرصاد الجوية فوق حوض Rheraya من خلال طريقة الاستيفاء المشتركة، (د) دمج كل من منتجات منطقة الغطاء الجليدي Aquaو Terra لمقياس طيف التصوير ذي الدقة المتوسطة (MODIS) ، (هـ) تحليل حساسية عتبة تحويل SWE-SCA.

تشير النتائج على المستوى المحلي إلى أن نماذج ذوبان الجليد المعززة بالإشعاع الشمسي تفوقت على نموذج مؤشر درجة الحرارة البسيط (TI) وكانت أيضًا أكثر قابلية للنقل بين السنوات، خاصة عندما تمت معايرة معلمات النموذج على مدار عام واحد. ومع ذلك، كان أداء النموذج أكثر تشابهًا عندما تمت معايرة النماذج لفترة أطول. من ناحية أخرى، فإن إدراج أنماط الإشعاع، على مقياس الحوض، له تأثير ضئيل بشكل عام على المتوسط المحاكي على مستوى الحوض ومنطقة الغطاء الثلجي (SCA) مقارنة بنموذج TI المرجعي. يحدث هذا بسبب حساب متوسط التغيرات الطبوغرافية في الإشعاع الشمسي وتجميع مخرجات النموذج إلى دقة MODIS، والتي تمنع التباين المكاني الرئيسي المتعلق بالإشعاع الشمسي. تستدعي نتائجنا توخي الحذر عند استخدام منتجات الأقمار الصناعية ذات الدقة المتوسطة لمعايرة أو التحقق من صحة نماذج الثلج الموزعة مكانيًا. وبالتالي، فإن النتائج تؤكد على توخي الحذر عند استخدام منتجات الأقمار الصناعية متوسطة الدقة للتحقق من صحة نماذج الثلج الموزعة مكانيًا، وهي ممارسة مستخدمة على نطاق واسع في نمذجة الثلج الهيدرولوجي. تتناول نتائجنا الاعتبارات المركزية المتعلقة بأداء النموذج والعمليات المعتمدة على المقياس والتحقق من صحة النموذج. بهذا يجب أن يكون هذا البحث ذا أهمية خاصة لمجتمعات الثلج والهيدرولوجيا.

. **الكلمات المفتاحية**: ذوبان الجليد، مكافئ مياه الثلج (SWE)، منطقة الغطاء الثلجي (SCA)، نماذج مؤشر درجة الحرارة، الإشعاع الشمسي، MODIS ، الأطلس الكبير ، المغرب.

TABLE OF CONTENTS

LIST OF FIGURES

LIST OF TABLES

LIST OF ACRONYMS

AWS	Automatic Weather Station
AVHRR	Advanced Very High Resolution Radiometer
CMG	Climate Modeling Grid
CAF	Club Alpin Français
C5	Collection 5
C6	Collection 6
DEM	Digital Elevation Model
EB	Energy balance
ETI	Enhanced temperature-index
FSC	Fractional Snow Cover
IDW	Inverse Distance Weighting
MAE	Mean Absolute Error
MODIS	MOderate Resolution Imaging Spectroradiometer
NSE	Nash-Sutcliffe Efficiency
NOHRSC	National Operational Hydrologic Remote Sensing Center
NDSI	Normalized Difference Snow Index
OA	Overall Accuracy
QA	Quality Assessement
QIR	Quantitative Image Restoration
SWIR	Shortwave near-infrared
SCA	Snow Cover Area
SCE	Snow cover Extent
SWE	Snow Water Equivalent
TREMA	Télédétection et Ressources en Eau en Méditerranée semi-Aride
TI	Temperature-index
RMSE	the root mean squared error
UTM	Universal Transverse Mercator
VIS	Visible
WGS84	World Geodetic System 1984

LIST OF SYMBOLS

Td	Dew point temperature
d	day
DPLR	Dew point temperature lapse rate
LW_{IN}	Incoming longwave radiation
SW_{IN}	Incoming shortwave radiation
K	Kelvin
LW_{OUT}	Outgoing longwave radiation
SW_{OUT}	Outgoing shortwave radiation
Pa	Pascal
P	Precipitation
PLR	Precipitation lapse rate
RH	Relative humidity
TLR	Temperature lapse rate

INTRODUCTION

Snow constitutes a key element in determining water availability in mountainous catchments, especially in arid and semiarid regions, where water stress, drought, and chronic water shortages are the most common problems. In such contexts, hydrological processes are extremely heterogeneous, due to the marked temporal variability in hydro-climatic conditions, combined with the strong topographic gradients (Cudennec et al. 2007, De Jong et al. 2008, Muñoz et al. 2012, Fayad et al. 2017). According to model projections, future climate conditions in these areas will strongly affect water availability due to: (i) a reduction of snowfall and rainfall amounts, and (ii) snowpack depletion driven mainly by warmer temperatures (Barnett et al. 2005, López-Moreno et al. 2009, López-Moreno et al. 2017). A good understanding of snowpack processes is therefore crucial to support water management strategies in these arid and semiarid regions (Barnett et al. 2005, Viviroli and Weingartner 2008, De Jong et al. 2009, Vicuña et al. 2011).

In Morocco, the Atlas mountain range plays an important role in socio-economic development. It is considered as a water tower for the surrounding arid plains, producing a large proportion of the water supply for agriculture activities, dam storage, hydropower production, and groundwater recharge (Chehbouni et al. 2008, Jarlan et al. 2015). In the headwater basins of this mountain range, streamflow is largely generated from meltwater supplied by the snowpack during spring and early summer (Schulz and de Jong 2004, Boudhar et al. 2009, Hajhouji et al. 2018, Boudhar et al. 2020). In winter, 20 to 80 % of precipitation is stored temporarily as snow (Boudhar et al. 2009) that controls river runoff during the snowmelt period (Chehbouni et al. 2008). Moreover, in the Tensift River basin, which is the region of interest in this study, snowmelt was found to contribute about 15 to 50 % of the annual river discharge in the main headwater catchments, this proportion varying between hydrological years and among catchments (Boudhar et al. 2009). As in other semiarid mountain ranges of the world, the snow cover in the Atlas range is highly variable at annual and inter-annual time scales (Boudhar et al. 2011, Marchane et al. 2015), which greatly affects the storage capacity of catchments and the hydrological contribution of snowmelt to total runoff.

Various prior studies have used the High Atlas Range as an experimental site for mountain hydrological studies, particularly on snow hydrology. Schulz and de Jong (2004) highlighted the impact of the sublimation process on the snowpack energy balance in the mountain of M'Goun during cold and dry seasons by quantifying 44 % of losses simulated with the Utah Energy Balance (UEB) model. In the northern side of the High Atlas, numerous studies have been conducted in the framework of the International Mixt Laboratory (LMI-TREMA) (https://www.lmi-trema.ma/). These were focused specifically on snowpack evolution and monitoring through either satellites data (Chaponnière et al. 2005, Boudhar et al. 2009, Marchane et al. 2015), or modeling techniques (Boudhar et al. 2009, Boudhar et al. 2016, Bouamri et al. 2018, Baba et al. 2019) to assess snow water equivalent (SWE) and snowmelt for water budget calculation and runoff prediction. Although all these studies, it is worth noting that the lack of ground observations along with the high temporal and spatial heterogeneity of snow cover driven by highly variable temperatures, orographic precipitation, and complex topography still represent challenging limitations for snow studies in the Atlas range (Chaponnière et al. 2005, Boudhar et al. 2010, Marchane et al. 2015, Boudhar et al. 2016). In this context, the use of simple conceptual snow models is highly relevant and useful for water managers.

The traditional approaches used to calculate snowmelt range from simple empirical models using simplified process representations with lower data requirements (e.g. Hock 2003, Kustas and Rango, 1994) to more sophisticated, physically-based models that resolve the full energy balance at the snow surface (Tarboton and Luce 1996, Liston and Elder 2006, DeWalle and Rango 2008, Herrero and Polo 2016). These latter models describe all major processes controlling snowpack evolution and quantify melt as the residual of the energy balance equation. They require a large amount of input meteorological variables, usually at an hourly time step, which are typically either not available or scarce in high mountain catchments. In such conditions, conceptual models with lower data requirements than physically based models, are thus preferred and widely used for large-scale applications in high mountain catchments (Singh and Bengtsson 2003, Schneider et al. 2007, Fassnacht et al. 2017).

Several previous studies have shown that temperature-index models, the most commonly used type of models which depend solely on air temperature, provide satisfactory estimates of melting rates in various locations and climates (Singh and Jain 2003, Schneider et al. 2007, Boudhar et al. 2016, Fassnacht et al. 2017). The strong correlation between air temperature and snowmelt can be

explained by the dependence of the sensible heat and atmospheric long-wave radiation fluxes to air temperature (Ohumura 2001, Hock 2003). Despite their simplicity, these models can perform generally well both at the point scale and within distributed or lumped hydrological models (Vincent 2002, Abudu et al. 2012, Kampf and Richer 2014, Senzeba et al. 2015, Hublart et al. 2016, Réveillet et al. 2017).

The net solar radiation is one of the main components of the surface energy balance, representing between 50 and 90 % of the energy available for snowmelt (e.g.Willis et al. 2002, Mazurkiewicz et al. 2008). As such, air temperature and solar radiation have been the two main meteorological variables used to predict snowmelt rates (Brubaker et al. 1996, Richard and Gratton 2001, Hock 2003). Many attempts have been made to improve the physical foundation of empirical melt models and enhance their performance, by incorporating additional predictive variables such as wind speed, vapor pressure or radiation (e.g. Zuzel and Cox 1975, Willis et al. 1991, Kustas and Rango 1994, Rango and Martinec 1995, Franz et al. 2010). These models have been broadly referred to as 'enhanced' temperature-index (ETI) models and represent a trade-off between simple degree-day models and explicit energy balance models (Hock 2003). Most enhanced melt models include a solar radiation term, either in the form of potential clear-sky direct (Hock 1999), global (Kustas and Rango 1994), or net (Pellicciotti et al. 2005) solar radiation. These enhanced temperature-index models including solar radiation can outperform classical degree-day models on a daily or even hourly basis (Hock 1999, Pellicciotti et al. 2005, Carenzo et al. 2009, Homan et al. 2011, Raleigh and Lundquist 2012, Gabbi et al. 2014, Bouamri et al. 2018).

In the semiarid, subtropical context of the Atlas Range, solar radiation is expected to be significant especially for spatial SWE modeling (López-Moreno et al. 2017) considering that; (i) solar radiation strikes the Earth surface at a large elevation angle during spring over subtropical regions, delivering more heat per unit area; (ii) the arid climate favors the transmissivity of solar radiation and the sparse vegetation favors high absorption of solar irradiance by the surface; (iii) the pronounced topographic variability should cause heterogeneous radiation loading on slopes (Baba et al. 2019). However, the seasonal variability of solar radiation is less pronounced than at higher latitudes. In this context, the use of enhanced temperature-index (ETI) including solar radiation, combined with remote sensing data constitutes a useful approach to assess and quantify snowmelt and SWE distribution at the basin scale.

There have been few studies that have looked at the respective performance of empirical models in semiarid mountainous areas, particularly no study have been carried in High Atlas to explore the added value of including different treatments of solar radiation within temperature-index (TI) models to predict snowmelt and snow water equivalent (SWE). Such models could become most useful in the operational framework of water management given the lack of ground data in the High Atlas to run energy-balance models. In this sense, a detailed study on investigating the contribution of solar radiation components on snowmelt and SWE simulations in the Atlas range is needed.

1. Main objectives

This research has been done at both scales: (1) local at the Oukaimeden-SM automatic weather station (AWS), and (2) spatial at the Rheraya sub-basin in the High Atlas range.

Within the aforementioned context, the purpose of this thesis is:

- Estimate and quantify snowmelt and snow water equivalent (SWE) in both Oukaimeden-SM (AWS) and Rheraya sub-basin, through different snowmelt modeling approaches.

The following two objectives were defined to pursue the mentioned purpose.

1. Assess the performance of four simplified approaches, ranging from simple temperature-index (TI) method to enhanced temperature-index (ETI) methods that include the incoming radiation and albedo to simulate snowmelt and snow water equivalent (SWE) at 'Oukaimeden-SM' station.

This first objective looked at (a) the respective performance of empirical models through two different cross calibration-validation methods: annual and multiannual over the period 2003-2010. (b) The parameter sensitivities for each model were further examined to investigate their transferability in time and their dependency on climate conditions. In addition, (c) the influence of mean sublimation rate on yearly calibrated model coefficients is explicitly investigated.

2. Benchmark the performance of enhanced models (ETI) including different treatments of solar radiation, relative to the reference temperature-index (TI) model to simulate spatially-distributed snowmelt, snow water equivalent (SWE), and snow cover area (SCA) within the Rheraya basin from 2003 to 2016.

We hypothesized that including solar radiation would explain more of the snow cover spatial heterogeneity; i.e. allows to explicitly include the effect of topography on melt and as such to better represent the snow cover heterogeneity. Therefore, it is important to assess their relevance for estimating snowmelt with conceptual models allowing to later improve hydrological forecasts.
This second objective aims to answer the following research questions:

a) *How temperature-index models enhanced with different solar radiation components impact the simulated spatiotemporal variability of SWE and snowmelt?*

b) *Are the available MODIS SCA maps suitable for snow model validation?*

2. Content of report

The various steps and methods to fulfill the above-defined objectives are described in this Ph.D. dissertation which is composed of four chapters as follow:

The *first chapter* provides a review of theoretical notions and literature on which the Ph.D. thesis is based. It introduces the snow mass balance components with a focus on ablation processes, .i.e. snowmelt, sublimation, and resulting changes in snow water equivalent. A short description of the radiative theory is also included to underline the necessity of energy budget knowledge in snowmelt modeling. The comparison between simple conceptual models, physically based, and energy balance models are reviewed and compared, in the perspective of identifying and highlighting the interest of using the simplest models in a scarce data context. Finally, a brief review of the importance of snow monitoring for hydrologic applications is presented.

The *second chapter* describes the High Atlas Mountain context, particularly the Rheraya catchment case study and the dataset we have used in this Ph.D. thesis. A full description and more details about in-situ and satellite data are presented. The pre-and post-processing, analyses are also given in this chapter.

The *third chapter* is based on results published article in the H*ydrological Science Journal (HSJ)*, introduced by an introduction of a key point in which the elements of novelty are highlighted. This chapter addresses the evaluation of the performance of four conceptual snowmelt models at the locale scale of the Oukaimeden-SM AWS station. The methodology and the obtained results are also presented and discussed.

The *fourth chapter* is also introduced by the key points of research. This chapter investigates the added value of solar radiation using the same conceptual snowmelt models used in the previous chapter, but this time at the basin scale, showing and discussing all obtained results. Finally, the overall conclusion of this work and perspectives are given.

CHAPTER I.
THEORETICAL BACKGROUND

A good understanding of snow characteristics, physical and optical, is crucial to hydrological snow modeling, and also in many practical applications of snowpack monitoring and modeling. A short discussion of main snow priorities is presented here.

1. Snow mass-balance

One of the most common priorities of snowpack monitoring and modeling, and the most important snow metric is the snow water equivalent (SWE). It is considered a key parameter in snow hydrology and highly relevant for water management purposes. SWE is defined as the amount of liquid water present in the snowpack that would be released upon complete melting of the snowpack (Singh 2001, DeWalle and Rango 2008, Egli et al. 2009). It can be measured (i) directly by specific instrumentation, or (ii) retrieved through different remote-sensing techniques, or (iii) computed from measurements of depth and density of the snowpack, as presented in equation (1).

$$\mathrm{SWE} = (\rho_s/\rho_w) \times d \quad (1)$$

Where SWE is the snow water equivalent (mm), ρ_w is the density of liquid water (1000 kg m^{-3}), d is snowpack depth (mm) and ρ_s is snowpack density, (kg m^{-3}).

The snow-mass balance represents the difference between snow accumulation (gains) and snow ablation (losses) throughout a time period. It consists to quantify and analyse the main processes determining snow accumulation, evaporation, and melting within a snowpack. Quantifying snow-mass balance processes remains crucial for predicting current and future water supply rates. Therefore, the snow mass-balance can be expressed by the following equation (e.g. King et al. 2008, Herrero et al. 2009).

$$\mathrm{dSWE}/\mathrm{d}t = P - M - E \pm W \quad (2)$$

Where $\mathrm{dSWE}/\mathrm{d}t$ is the change in snow mass per unit time (d), P is the snow precipitation rate (accumulation), M is the melt rate, E is the sum of sublimation and evaporation rates at the surface,

and *W* is an advective wind transport term, which can be positive (deposition) or negative (erosion).

Snow accumulation and ablation are two main hydrological processes for any hydrological study in snow-affected basins. A detailed outline of these processes is given on the following sections.

1.1. Accumulation processes

Generally, precipitation occurs as snow when the air temperature over the surface is below the freezing point. The snow will accumulate on the surface as long as the air temperature remains below the freezing point. Then, several transformations occur on the snowpack depending on time and local parameters and climatic conditions, especially, diurnal air temperature fluctuations. However, it is worth noting that the accumulated snowfall on a site can be quite variable on a microscale, i.e. as weather conditions change, the snowpack can change as well.

1.2. Ablation processes

Ablation is the process of removing snow-mass from a snowpack surface, due to a combination of processes : melting, sublimation, and wind erosion. The ablation rates are largely controlled by the energy budget at the snowpack surface. Thus, the processes characterized the snow ablation in arid regions are:

- ***Snowmelt process***: Defined as the phase transition of solid snow into liquid water with energy transfer expressed as latent heat. It is determined by the energy balance of the snowpack, which basically depends on atmospheric and climatic conditions. The necessary energy quantity, to raise the snow temperature to the melting point, corresponds to the cold content of the snowpack. After satisfying this cold content the snowpack reaches isothermal (0°C) conditions, each further energy input causes melt.
- ***Sublimation process:*** Defined as the phase transition of solid ice or/and snow into water vapor with consuming energy. It is mainly driven by a vapor pressure deficit in the air above the snow layer, i.e. an imbalance between the saturation vapor pressure at a given temperature, and the vapor pressure of the air above the snow surface. When the former exceeds the latter, snow sublimates to eliminate the imbalance (Neumann et al. 2009). Sublimation is considered an important component of the ablation process, especially in mountain areas with dry climates, where high elevations provide favorable conditions for

sublimation due to a decrease in vapor pressure and an increase in wind speed with elevation (Ginot et al. 2001, Schulz and de Jong 2004, Gascoin et al. 2013, MacDonell et al. 2013).

1.3. Wind transport

Because of its density, snow is often transported or redistributed by wind (*W* in equation (2)) for a long distance, before its sublimates or/and deposited in a snowpack surface (DeWalle and Rango 2008). Thus, the wind has a strong effect on snow distribution in mountainous terrain, most likely in dry climates (Liston et al. 2007, Gascoin et al. 2013). The probability of blowing snow increases with wind speed and decreases with snow age and air temperature (Li and Pomeroy 1997).

Three modes of wind transport are commonly distinguished for transported snow or as called 'blowing snow': (a) creep, in which snow particles simply move by sliding, rolling, or creeping at the surface due to the force of the wind. (b) Saltation occurs when snow particles move with repeated leaping up and colliding with a snow surface, and (c) suspension when particles are transported upwards by turbulent eddies and transported far downwind, and generally involves the transport of smaller ice and snow particles (Figure 1). Generally, the dominant mode and the magnitude of blowing-snow transport depends upon the interaction of climate, snow surface conditions, and topographic features, but in general, transport is dominated by the suspension.

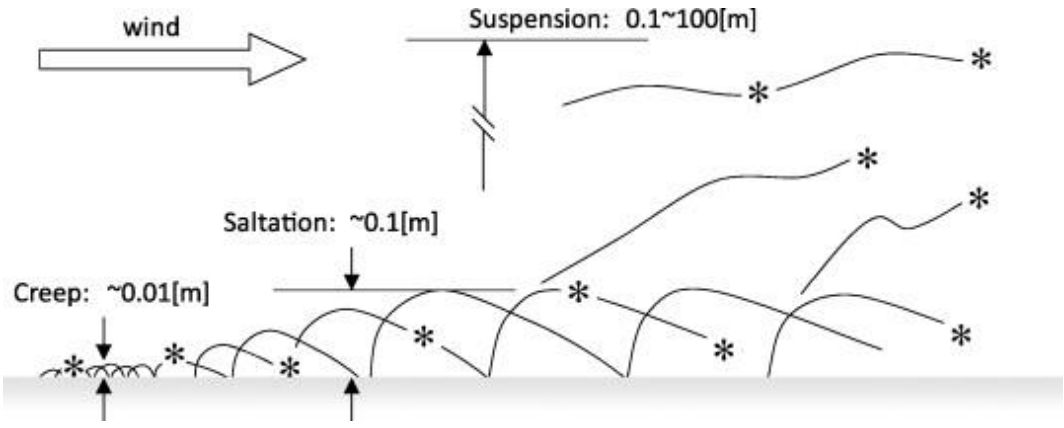

Figure 1: Transport modes for blowing snow (Tominaga et al. 2011)

2. Energy balance

All physical processes within a snowpack are considered highly complex, including mass and energy balances as well as heat (Tarboton and Luce 1996, Singh 2001, DeWalle and Rango 2008). Accordingly, to determine the rate of snowpack losses; including melt or sublimation, a good understanding of the energy exchanges between snowpack and the snow-atmosphere interface is crucial for our work. The energy exchanges primarily occur at the snowpack surface through the exchange of shortwave and longwave radiations, turbulent or convective transfer of latent heat due to vapor exchange, and sensible heat due to differences in temperature between the air and snow. The sum of all these energy exchanges over a determined time period constitute the energy balance for the snowpack and can be written as the algebraic sum of energy gains and losses as:

$$Q_M = SW_{IN} + SW_{OUT} + LW_{IN} + LW_{OUT} + Q_S + Q_L + Q_R + Q_G \quad (3)$$

Where Q_M is the energy at the surface available for melt (W m^{-2}), SW_{IN} and SW_{OUT} are incoming and outgoing shortwave solar radiation, respectively; LW_{IN}, LW_{OUT} are longwave radiation, incoming and outgoing respectively; Q_S is the sensible-heat flux, Q_L is the latent-heat flux, Q_R is the energy supplied by rain on snowpack and Q_G is the ground heat flux. All fluxes are positive toward the snowpack surface and calculated in W m^{-2}.

2.1. Shortwave radiation

The net shortwave radiation is the major source of energy for snowmelt. The incoming solar radiation (SW_{IN}) emits ~1368 W m^{-2} at the top of the atmosphere (TOA). Although not all amount of this solar radiation from the Sun reaches the snowpack, some of this is reflected off clouds, some is absorbed by atmospheric constituents (water vapor, aerosols, gases), and some passes through the snowpack surface (Figure 2). Thus, various variables control the amount of solar radiation reaching a snowpack surface such as the slope and aspect of the surface, the solar angle, cloud cover, aerosols content of the atmosphere.

The incoming shortwave radiation received on horizontal surfaces is ideally obtained by direct measurement using radiometers at nearby index stations. Pyranometers are radiometers used to measured total incoming shortwave radiation. Generally, the shortwave instruments respond to

wavelengths between 0.2 - 4 μm, which includes the majority of solar radiant energy received at the Earth-surface. However, empirical methods are available for the estimation of incoming shortwave radiation when direct measurements are unavailable.

2.1.1. Net shortwave radiation

The net shortwave radiation (SW_{NET}) is an important component of the energy balance, which is equal to the incoming shortwave radiation (SW_{IN}) received at the snowpack-surface minus the amount reflected by the snowpack-surface; thus SW_{NET} would be:

$$SW_{NET} = SW_{IN}\,(1 - \alpha) \tag{4}$$

Where α is the albedo or the fraction reflected by the snowpack-surface that will be described in the next section.

2.1.2. Albedo

Albedo is defined as the fraction of shortwave radiation reflected by the snowpack-surface. It ranges from above 0.95 for a fresh snowfall down to below 0.40 for shallow, dirty snow as presented in Table 1. Generally, fresh snow has a high albedo of 0.75 to 0.98, while darker materials have lower values of 0.6 to 0.30 depending on the material. Albedo is considered a crucial variable in climatology; i.e. its characteristics related to atmospheric parameters, solar radiation and the properties of the Earth's surface makes it special for the detection of spatial and temporal climate changes. The snowpack albedo is affected by many factors (Warren 1982, Kustas and Rango 1994, Hock 1998, DeWalle and Rango 2008) that make a precise prediction of snowpack albedo difficult, such as grain size, impurity content, and surface roughness. Although it is worth mentioning that low albedo supports, consequently, the absorbed shortwave radiation available for melt, which is increasingly important for energy budget (Pomeroy and Brun 2001).

Table 1: Characteristic values for snow albedo (Marshall and Oglesby 1994)

Surface Type	Recommended	Minimum	Maximum
Fresh dry snow	0.85	0.75	0.98
Old clean dry snow	0.80	0.70	0.85
Old clean wet snow	0.60	0.46	0.70
Old debris-rich dry snow	0.50	0.30	0.60
Old debris-rich wet snow	0.40	0.30	0.50

2.2. Longwave radiation

The heat resulting from the absorption of incoming shortwave radiation by aerosol particles in the atmosphere is emitted as longwave radiation (LW_{IN}) to the Earth. It is infrared thermal radiation (4 - 100 μm) that occurs both days and night which greatly contributes to accelerate the melting process (Figure 2). Net longwave radiation at a snow surface is largely controlled by overhead back radiation from the earth's atmosphere, clouds, and forest canopies. The snowpack emit infrared radiation (LW_{OUT}) depending on its surface temperature.

Unlike shortwave radiation, measurements of longwave radiation are much less common, but in recent years radiometers have been developed that can be used for routine monitoring. Regardless, computations of longwave exchange are often using the Stefan–Boltzmann equations (DeWalle and Rango 2008).

Figure 2: Descriptive schema of net SW and LW (source (https://science.nasa.gov/))

2.3. Turbulent energy fluxes

The sensible heat flux (Q_S) corresponds to the transfer of heat between the atmosphere and snowpack surface whenever a temperature difference exists between both. The transfer direction depends primarily on the sign (±) of the temperature difference, i.e. positive if the atmosphere is warmer than snowpack-surface and negative in the opposite case. In addition to temperature difference, wind speed, surface roughness and the stability of the air also influence the direction and magnitude of this heat transfer (Figure 3).

The latent-heat (Q_L) is associated with the energy used or released during water phase changes; i.e. water vapor exchange between the snowpack and atmosphere also occurs due to turbulent mixing in the boundary layer. Transfer of vapor from the snowpack to the atmosphere constitutes a loss of latent heat of vaporization if the liquid water is present at the snowpack surface, and a loss of latent heat of sublimation if subfreezing temperatures prevail.

The transfer of turbulent heat on the snowpack can be expressed by the bulk aerodynamic equations (Kustas and Rango 1994): as follow:

$$Q_S = \rho_a \, c_p \, C_h \, u_a (T_a - T_s) \tag{5}$$

$$Q_L = (\rho_a \, 0.622 \; L/P) \; C_e \, u_a (e_a - e_s) \tag{6}$$

Where ρ_a is the density of air in kg m^{-3}, c_p specific heat of the air in J kg^{-1} K^{-1}, C_h bulk transfer coefficient for sensible heat, and C_e the bulk coefficient for vapor exchange, u_a wind speed in m s^{-1}, T_a is the air temperature in Kelvin (K), T_s is the air temperature at the snowpack surface (K), L is the latent heat of vaporization or sublimation in J kg^{-1}, e_a is the atmospheric vapor pressure in pascals (Pa) and e_s is vapor pressure at the snowpack surface (Pa), and finally, P is the total atmospheric pressure (Pa).

It is worth underlying here, that the snowmelt process is determined by the energy balance at the snowpack-atmosphere interface, which is controlled mainly by the meteorological conditions above the snowpack and the physical proprieties of the snowpack. The amount of energy required, in order to raise the snow temperature to the melting point, corresponds to the cold content of the snowpack. After reaching isothermal conditions within the regarded snowpack at 0°C, any surplus

of energy causes melt.

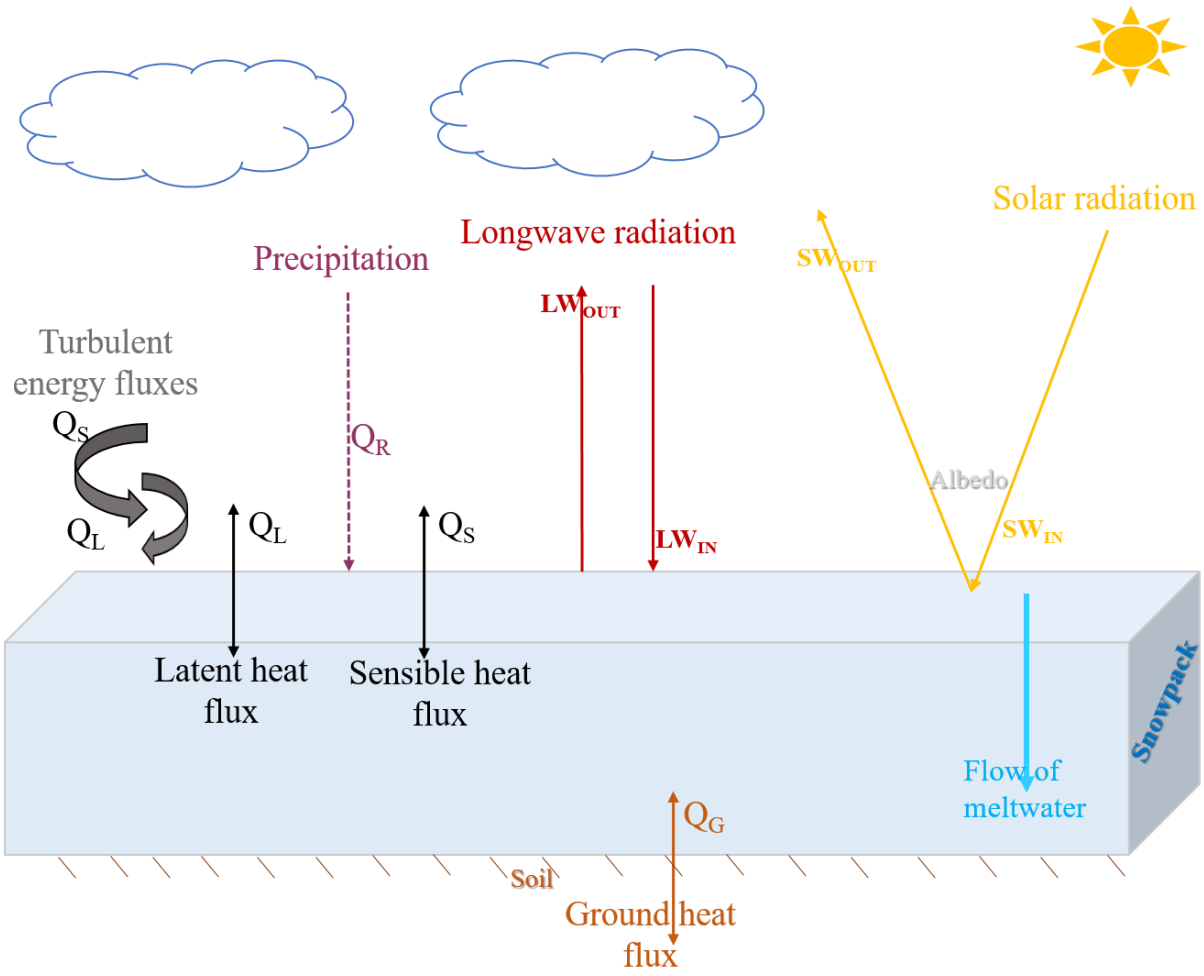

Figure 3: Energy and snow-mass balance

3. Snowmelt Modeling

A model is a simplified representation of the real-world system, and the ideal model is the one that generates results very close to reality. Each model requires specific parameters and variables (inputs) to generate simulated variables (outputs).

Modeling differs from one context to others and depends on purpose and field of study. In our case, snow modeling is used to provide decision-makers and managers the amounts of snowmelt contribution to water balance for a better preventive and forecast of floods, through estimating the hydrological variables (SWE, melt). On the other hand, they are used to assess the influence and direct impact of climate change on water availability in mountain regions. Generally, various

modeling approaches may be used as follow:

- ***Punctual approach***: it consists of modeling all snowpack characteristics at a specific location which is usually a weather station. Generally, this type performs well taking into account that all forcing parameters at forced in the same location of measurements. However, the extrapolating of simulated results over a large area remains difficult taking into account the snowpack variability.

- ***Semi-distributed***: Consists in splitting the study area into different elevation ranges which are assumed to have the same characteristics (for instance; altitudes, slopes, and aspects). This modeling approach is suitable for capture snowpack variability in mountainous areas.

- ***Distributed***: the study area is subdivided into several grid points, each grid is characterized by its specific properties (e.g. altitude, slope, orientation, and land use). This discretization makes it possible to take into account more explicitly the spatial variability of physical processes related to topography in particular.

3.1. Snow models

Over the last decade, a wide variety of snow models have been developed with many levels of complexity for different purposes. Therefore, the choice of a model remains critical and depends mainly on (i) the availability of data which is today the most limiting factor, (ii) the objective of the study, and (iii) computer power; i.e. each model has its specific characteristics depending on the degree of complexity and the degree of accuracy desired. These approaches range from simple empirical models (e.g. Kustas and Rango 1994, Hock 2003), to more sophisticated, physically-based models (e.g. Liston and Elder 2006, Herrero and Polo 2016) , and thus they can be organized into categories, as follow;

3.1.1. Temperature-index models

The temperature-index (TI) models or so-called degree-day models remain the most classical and simplest conceptual models used for snowmelt modeling, due to the widespread availability of air temperature data and their computational simplicity (Hock 1999, Hock 2003). They use simplified process representations with lower data requirements than physically-based models and are thus widely used for large-scale applications, i.e. they depend solely on air temperature and use it as a

proxy for the energy available above the snowpack. The reason for the success of air temperature as the sole index of melt energy is related to the strong correlation between air temperature and snowmelt, which can be explained by the dependence of the sensible heat and atmospheric longwave radiation fluxes to air temperature (Ohumura 2001, Hock 2003). It is worth mentioning that most operational runoff models use temperature-index methods for melt modeling, e.g. HBV model (Bergström 1976), SRM-model (Martinec and Rango 1986), and UBC-model (Quick and Pipes 1977).

3.1.2. Enhanced temperature-index (ETI)

The enhanced temperature-index (ETI) models have an 'intermediate complexity' between both TI and energy balance models (Hock 1999, Pellicciotti et al. 2005). They have been developed to improve the physical foundation of empirical melt models and enhance their performance, by incorporating additional predictive variables such as wind speed, vapor pressure or radiation (e.g. Zuzel and Cox 1975, Willis et al. 1991, Kustas and Rango 1994, Rango and Martinec 1995, Franz et al. 2010). These models have been broadly referred to as 'enhanced' temperature-index models and represent a trade-off between simple degree-day models and explicit energy balance models (Hock 2003). Most enhanced melt models include a solar radiation term, either in the form of potential clear-sky direct (Hock 1999), global (Kustas and Rango 1994), or net (Pellicciotti et al. 2005) solar radiation.

3.1.3. Energy balance models

Energy balance (EB) models resolve the full energy balance at the snow surface and describe all major processes controlling snowpack evolution (Tarboton and Luce 1996, Liston and Elder 2006, DeWalle and Rango 2008, Herrero and Polo 2016). The melt is quantified as residual from the balance of heat flux exchanged between snowpack-surface and the atmosphere as well as between the base of the snowpack and the ground. They account for all the processes that produce spatial and temporal variability of snowmelt and thus can be argued to be the most appropriate approaches for simulating snowmelt. However, for operational applications, these models present some disadvantages; (i) they require a large amount of input meteorological variables than routinely available (air temperature, precipitation relative humidity wind speed, and incoming solar radiation) and usually at an hourly time step, (ii) difficulties in interpolation and/or extrapolation of some meteorological variable at the catchment scale, such as wind speed and incoming radiative

fluxes that especially require sophisticated and expensive sensors to measure, which hinder their applicability on larger scales.

3.2. Models benchmark review

Many studies have compared the performance between empirical and physical models (Pellicciotti et al. 2005, Carenzo et al. 2009, Gabbi et al. 2014) and highlighted that physical models are more accurate at the point scale than empirical models (Pellicciotti et al. 2008). However, at the catchment scale, their performance is questioned depending on required and available data (Carenzo 2012).

Despite their simplicity, several previous studies have shown that temperature-index (TI) models, provide satisfactory estimates of melting rates in various locations and climates (Singh and Jain 2003, Schneider et al. 2007, Boudhar et al. 2016, Fassnacht et al. 2017), and perform generally well both at the point scale and within distributed or lumped hydrological models (Vincent 2002, Li and Williams 2008, Abudu et al. 2012, Kampf and Richer 2014, Senzeba et al. 2015, Hublart et al. 2016, Réveillet et al. 2017). On the other hand, it has been demonstrated that enhanced temperature-index (ETI) models including solar radiation can outperform classical degree-day models on a daily or even hourly basis (Pellicciotti et al. 2005, Carenzo et al. 2009, Homan et al. 2011, Raleigh and Lundquist 2012, Gabbi et al. 2014, Bouamri et al. 2018).

4. Snow remote sensing

Snow is considered the second natural surface after clouds which is well captured, suited, or mapped by satellites, due to its physical proprieties, presenting a good contrast. Therefore, it has opened up possibilities of exploiting widely different parts of the electromagnetic spectrum to learn more about the snowpack proprieties (DeWalle and Rango 2008). The importance of monitoring snow cover, duration, and melt at local, regional, and global scales for climate and hydrologic applications have been documented in many studies worldwide (Romanov 2003, Dozier and Painter 2004, Song et al. 2008, Pimentel et al. 2015, Dozier et al. 2016). The spatially explicit snow cover information can support either modeling of runoff or can help to understand the influence of climate change on snow cover dynamics (Dressler et al. 2006).

Snow typically has a very high reflectance in visible wavelengths (VIS) across the 0.3 - 1.0 μm spectrum and very low reflectance in the shortwave infrared wavelengths (SWIR) to ~ 1.6 μm. This characteristic is used to detect snow on the landscape, by distinguishing between snow and cloud using satellite sensors with spectral bands in these cited wavelength regions. However, the reflectance of snow may decreases over time, because of natural aging or/and other factors (e.g. atmospheric conditions, snow metamorphism, solar elevation angle) (Riggs et al. 2015).

4.1. Normalized Difference Snow Index

The Normalized Difference Snow Index (NDSI) is generally used to indicate the presence of snow cover on the surface (Hall et al. 1995, Gupta et al. 2007). It measures the difference in reflectance between VIS and SWIR bands, ideally under sunlight conditions of fresh snow and high solar elevation angle and clear atmosphere to avoid lower reflectance as possible. NDSI is defined as:

$$NDSI = \frac{VIS\ (band\ 4) - SWIR\ (band\ 6)}{VIS\ (band\ 4) + SWIR\ (band\ 6)} \quad (7)$$

The NDSI values range from -1 to 1, which is the theoretically possible range for snow. A pixel with $NDSI > 0$ is considered to have some snow present, while a pixel with $NDSI \leq 0$ is a snow-free land surface (Riggs and Hall 2015). In general, an NDSI threshold value of 0.4 has been the consensus value for making SCA maps, first suggested by Dozier (1989) based on visual inspection of imagery. However recent research has demonstrated that the selection of an NDSI threshold for SCA can vary depends on many factors (Yin et al. 2013, Riggs and Hall 2015).

4.2. Snow cover area

Snow cover area (SCA) is considered an important variable for understanding, modeling, and predicting hydrological processes in snowmelt-dominated regions (Tekeli et al. 2005). It is a useful means of tracking spatiotemporal patterns in snowpack across variable mountain terrain. Additionally, the application of SCA for snowmelt modeling studies becomes indispensable for inaccessible and large basins particularly where meteorological data are scarce or not available (Singh and Jain 2003). SCA is one of the three fundamental features, along with snow water equivalent (SWE) distribution and melt rate, required to describe the spatial evolution of snow cover from the end of accumulation through melt (Liston 1999). Moreover, SCA is considered as a major and sensitive input into operational snowmelt runoff models since knowledge of the snow-

covered area is crucial for these models (Martinec and Rango 1986). This is exactly why the daily snow cover information is very valuable also for model calibration and validation purposes (Franz and Karsten 2013, He et al. 2014). Accordingly, such information can be extremely helpful when modeling available water resources in mountainous areas where snowmelt in spring or summer becomes a valuable source for energy production.

4.3. Fractional snow cover

The fractional snow cover (FSC) is considered as the viewable fraction of snow in a pixel (Nolin 2010). Considered as a more useful measure of snow cover, FSC ranges from 0 to 100 % and conveys information about the amount of snow visible on the landscape. Various methods have been used to estimate FSC including; spectral mixture analysis primarily for alpine landscapes; (Dozier and Painter 2004, Painter et al. 2009, Rittger et al. 2013), semi-empirical modeling of snow reflectance (Metsämäki et al. 2005), and regression of empirical relationship between a low-resolution sensor and a higher resolution sensor such as MODIS with Landsat TM (Salomonson and Appel 2004, Salomonson and Appel 2006) to estimate snow fraction based on the NDSI.

CHAPTER II.
SITE DESCRIPTION, DATA AND METHODS

1. Study area

The study area considered in this work is the Rheraya sub-basin located in the headwater part of the Tensift River basin. It covers an area of 228 km² with elevations from 1060 to 4174 meters above sea level (a.s.l). The latter was selected due to the data availability at a set of weather stations, in terms of both temporal and spatial scales. Also, it has been used as an experimental site for mountain hydrological studies in the Tensift River basin (Jarlan et al. 2015), leading to a concentration of studies on snow and hydrology in this basin (Boudhar et al. 2016, Baba et al. 2018, Bouamri et al. 2018, Hajhouji et al. 2018, Baba et al. 2019).

The Rheraya basin is located in the Western part of the High Atlas Mountain chain in central Morocco, between latitudes 30° 10' and 30° 20', and longitudes 7° 40' and 8° (Figure 4). The Atlas range extends over 60 km in width and 800 km in length aligned along a NE–SW axis. It reaches a maximum elevation at the summit of Jbel Toubkal, the highest summit of North Africa, which culminates at 4167 m a.s.l. This mountainous zone constitutes the water tower of the Haouz plain and all surrounding downstream regions (Chaponnière et al. 2005, Rochdane et al. 2012, Hajhouji et al. 2018).

The area has a semiarid climate with two contrasting seasons: a wet season from October to May and a dry season from June to September. Characterized by a mixed snow-rain regime, annual cumulative precipitation can exceed 800 mm at high elevations, due to orographic uplift of cold and moist air masses from the North Atlantic Ocean. 50% of precipitation events, during 1989 - 2010 period, occurred as snow during the winter months (Boudhar et al. 2016). The snow cover is highly variable at annual and inter-annual time scales, and the snowmelt was found, between 2002 and 2005, to contribute from 28 to 48% of the of total streamflow volume (Boudhar et al. 2009). According to a long-term analysis of snow-covered area using remote sensing data (Marchane et al. 2015), snow cover dynamics in the High Atlas mountains is strongly heterogeneous and exhibits marked annual, seasonal and even weekly variability in response to meteorological variability.

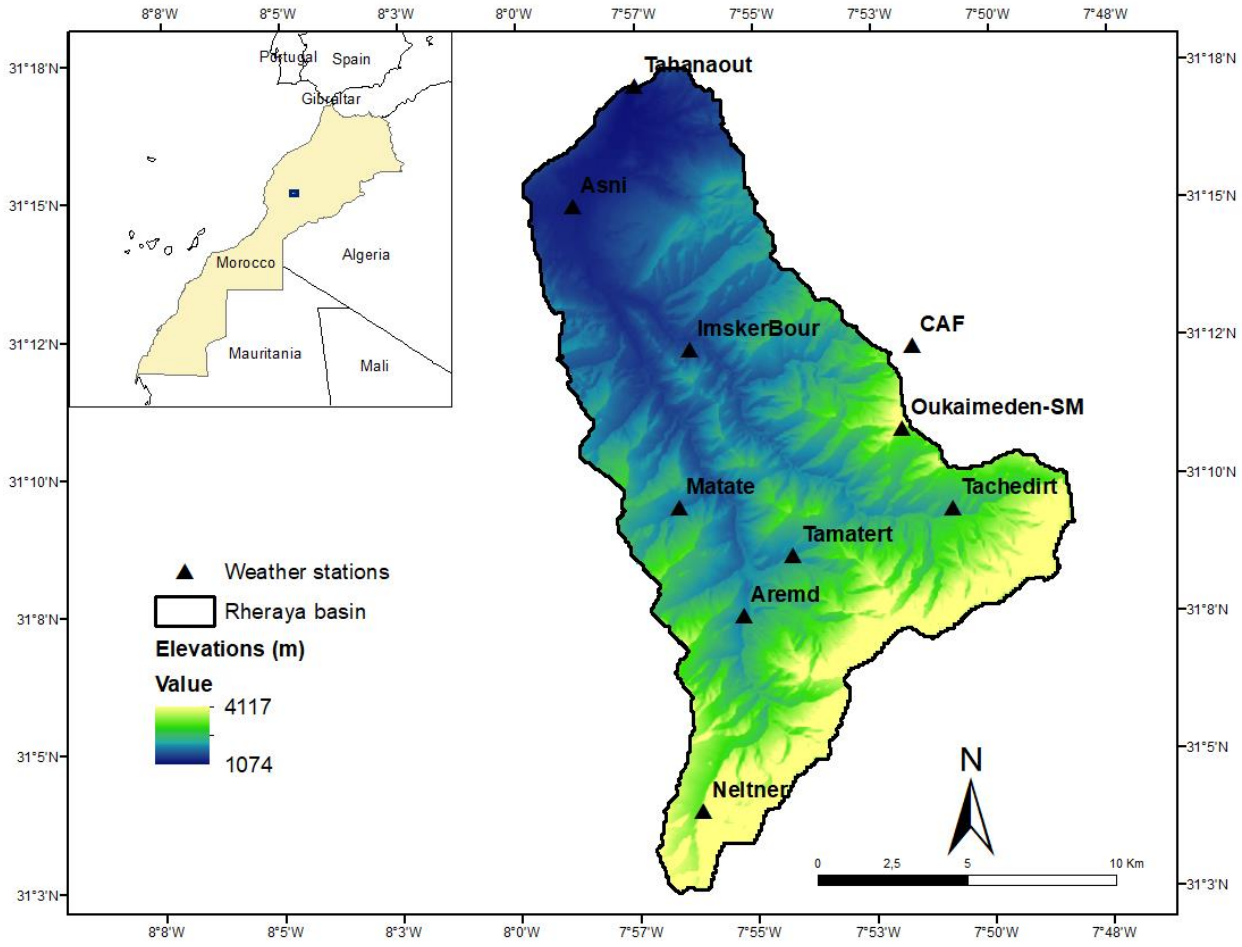

Figure 4: Geographical location of the Rheraya basin and weather stations network

In terms of topography, the slopes are steep with a mean of ~24 degree from a 100 m resolution DEM. Additionally, the Rheraya, has sparse vegetation especially during spring, located in the lowest elevations, which quickly disappear due to aridity.

2. Experimental and spatial datasets

2.1. Meteorological data

2.1.1. Data availability

All meteorological data used in this thesis were provided by the International Mixt Laboratory (LMI-TREMA). The available meteorological series were obtained from ten stations at various locations within the Rheraya watershed (Figure 4). The type of variable measured and record length of available observations varied between the stations over the studied period 2003-2016,

set for this work, taking into account the availability of all meteorological data (Figure 5). Further data availability details are summarized in Figure 5, Table 2. All main pre-processing and filters applied to original observations are described in the "3.1.1 Filters and pre-processing " section.

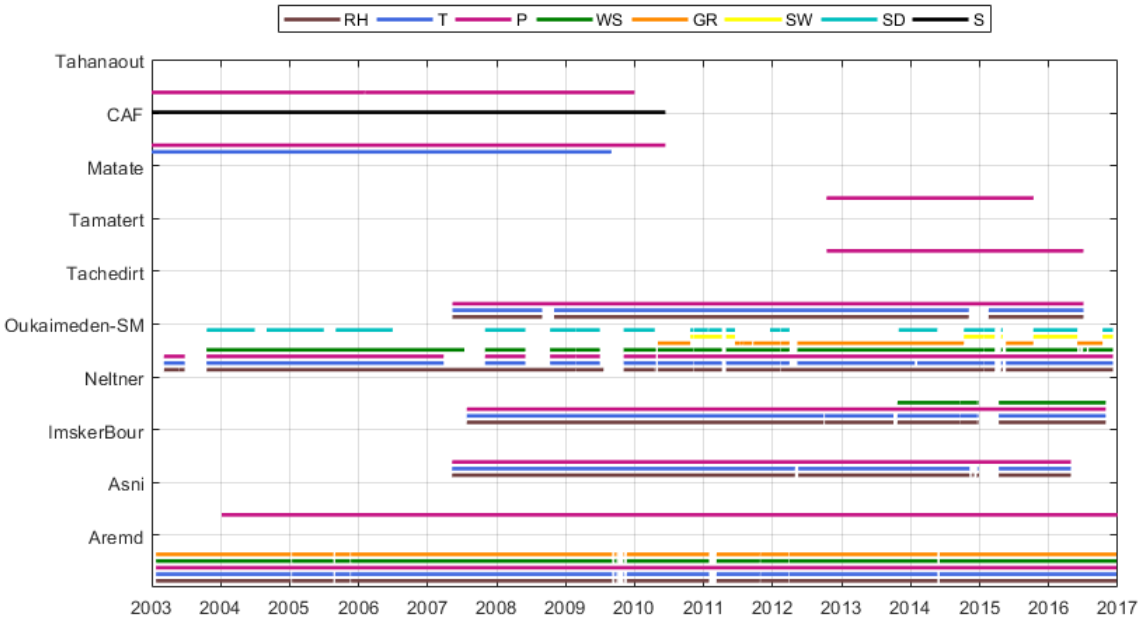

Figure 5: Available observations during the study period (2003-2016) for the different weather stations in the Rheraya catchment. RH: relative humidity; T: air temperature; P: total precipitation; WS: wind speed; GR: global radiation; SW: shortwave; SD: snow depth and S: snowfall

Table 2: Characteristic and geographic coordinates (WGS-84) of weather stations in the Rheraya catchment, with available observations: total precipitation (P), air temperature (T), relative humidity (RH), wind speed (WS), snowfall (S), shortwave (SW) and runoff (Q).

Stations	Latitude (°)	Longitude (°)	Elevation GPS (m)	Elevation DEM (m)	Available data
Aremd	31.12	-7.92	1940	1938	P, T, RH, WS,GR
Asni	31.25	-7.98	1170	1183	P
Imskerbour	31.20	-7.94	1404	1426	P, T, RH.
Neltner	31.07	-7.94	3207	3120	P, T, RH, WS
Oukaimeden-SM	31.18	-7.87	3230	3239	P, T, RH, WS, SW, GR
Tachedert	31.16	-7.94	2343	2321	T, RH
Tamatarte	31.14	-7.90	1924	1913	P
Matate	31.16	-7.85	1825	1800	P
CAF	31.21	-7.86	2612	2635	P, T, S
Tahanaout	31.29	-7.96	925	1069	P, Q

2.1.2. Weather stations

All meteorological series were collected from ten stations at various locations and different elevations within the Rheraya catchment. Previously some of these stations (Asni, Tamatert, and Matate) disposed only of classical rain gauges, non-autonomous (Figure 6A), where rain observations are recorded after each event by an observer present on site. While now they are equipped by autonomous tipping bucket for half-hourly cumulative values for rain (Figure 6B). It is worth mentioning that both Oukaimeden-SM and Aremd were the only two automatic weather stations that disposed of half-hourly measurements for most variables (T, P, and RH), and also the recorded solar radiations (SW, GR) in Rheraya over the studied period (2003-2016) (Figure 5, Table 2).

A- Classical rain gauge

B- Tipping bucket rain gauge

Figure 6: Different type of rain gauges at Rheraya weather stations (pictures from Cheggour 2008)

A description of the main stations used in this work is presented below, and Figure 7 shows the instruments available at some stations in Rheraya.

2.1.2.1. Oukaimeden SM

Oukaimeden-SM is a fully equipped automatic weather station (AWS) installed since 2003 (Figure 7E). The station is located at an altitude of 3200 m a.s.l., on the northern side of the High Atlas in the headwaters of the Rheraya sub-catchment, near to Oukaimdem ski resort and ~70 km south of Marrakech city. Recorded data include precipitation, incoming and outgoing shortwave radiation,

incoming and outgoing longwave radiation, air temperature, relative humidity and wind speed (Table 17). All historic set up and detailed meteorological instrumentation about Oukaimeden-SM AWS is given by Boudhar et al. (2016) (Table 16).

Despite the availability of all main meteorological variables in this station, it remains an unreliable and unconfident station due to an unheated tipping-bucket rain gauge (besides lack of either anti-freeze or anti-evaporation oil) which yields unreliable precipitation data in winter. Hence, it is worth noting in this study that, precipitation data of the Oukaimeden-SM station was excluded in the spatial distribution of precipitation taking into account the unreliable historic precipitation data.

2.1.2.2. Club Alpin Français

Despite its location outside, but near the catchment boundary, the Club Alpin Français (CAF) station is proven to be crucial in this study, especially to distribute precipitation at high elevations. The lower altitude of the CAF station (2612 m a.s.l.) has more reliable manual precipitation observations since rainfall and snowfall are independently and manually measured since 1988 (Figure 5, Table 2). It is located 600m lower than Oukaimeden-SM.

A- Tachdirt

B- Imskerbour

C-Aremd

D- Neltner

E- Oukaimeden-SM

Figure 7: Photos of different weather stations at Rheraya

2.2. Satellite data

2.2.1. Digital elevation model

A Digital Elevation Model (DEM) derived from Pleiades stereoscopic imagery at 4 m spatial resolution was used to represent the basin topography of this study. Pleiades is an optical satellite constellation of two twin satellites (Pléiades 1A and Pléiades 1B), launched on 6 December 2011 and 2 December 2012 respectively. The main satellite mission was to deliver a very high spatial resolution data equal to 50 cm after pre-processing, with a 20 km swath, and offering a daily revisit capability to any point on the globe. The image acquisition is characterized by two images in the same area with different angles which are then combined to drive the DEM. Three different stereo-pairs covering the Rheraya catchment were selected on three summer dates 04-08-2015, 17-08-2015, and 18-08-2015 to avoid the presence of snow. Further details about these images and DEM processing are provided in Baba et al. (2019).

2.2.2. MODIS daily snow cover product

2.2.2.1. MODIS description

MODIS snow cover data products have been widely used at local, regional and global scales by numerous studies worldwide (Hall et al. 2002, Klein and Barnett 2003, Tekeli et al. 2005, Parajka and Blöschl 2006, Liang et al. 2008, Zhang et al. 2010, Dietz et al. 2012, Gao et al. 2012, Dietz et al. 2013, Gascoin et al. 2015, Marchane et al. 2015). With its high time and free access, MODIS snow cover products are considered a benefit for hydrologists because the data have been improved for spatial resolution comparing to others such as NOAA and Advanced Very High-Resolution Radiometer (AVHRR) (1 km). Moreover, the MODIS products are (i) readily available for users without further classification (Hall et al. 2002, Tekeli et al. 2005, Hall and Riggs 2007), (ii) the snow/cloud discrimination capabilities, (iii) the geolocation accuracy and the frequent global coverage (daily coverage up to 500m).

Various studies have tested the accuracy of MODIS snow cover data, e.g Klein and Barnett (2003) reported an 88% agreement when comparing to measurements of the Upper Rio Grande Basin. Parajka and Blöschl (2006) compared snow cover data with in-situ information over the whole of Austria and reported an agreement of 95% on cloud-free pixels. A similar agreement has been reported by Hall and Riggs (2007) with an emphasis on the misclassification errors between cloud and snow pixels. However, Maurer et al. (2003) concluded less cloud-free misclassification (4%

and 5% fewer overall for the Columbia and Missouri basins, respectively) for MODIS than with National Operational Hydrologic Remote Sensing Center (NOHRSC) under cloud-free conditions.

2.2.2.2. MOD10A1 and MYD10A1

Snow cover maps used in this thesis were derived from the MODIS daily snow cover products MOD10A1 and MYD10A1 (MODIS Snow Cover Daily L3 Global 500 m SIN GRID V006), respectively generated from the Terra and Aqua MODIS satellites, and acquired from the National Snow and Ice Data Center (NSIDC) (Hall and Riggs 2016). The MODIS snow products from the Terra and Aqua satellites are available since February 2000 and February 2002, respectively. The satellites pass over the equator in the morning (Terra at 10:30 a.m. in a descending mode) and afternoon (Aqua at 1:30 p.m. in an ascending mode), capturing the earth's current state and provide two snow cover images for the same location per day. The MODIS uses 36 spectral bands to estimate 44 globally available data products with a spatial resolution of 250 m, 500 m, and 1 km. Moreover, it also provides a grid of snow cover information at 500 m spatial and daily temporal resolutions. The daily gridded snow cover product contains the NDSI snow cover, snow albedo, and QA observation selected from all the MOD10_L2 and MYD10_L2 swaths mapped into a grid cell. The snow cover is identified using the Normalized Difference Snow Index (NDSI) (Hall et al. 1995), which captures the high contrast between the characteristically high reflectance of snow in the visible (VIS) spectrum and its low reflectance in the shortwave near-infrared (SWIR) spectrum.

Starting in MODIS Collection 6 (C6), various changes have been made to increase data content and accuracy compared to older Collection 5 (C5) (Riggs and Hall 2015, Riggs et al. 2015). These changes include:

- The Fractional Snow Cover (FSC) has been replaced by the Normalized Difference Snow (NDSI) providing more flexible data to the user (Riggs et al. 2015).
- The binary Snow-Covered Area (SCA) map has been discontinued.
- Data screens designed to reduce snow detection errors of omission and commission have been revised and several new screens have been added for mapping snow cover extent (SCE) accurately on the global scale.
- Data screen results are provided in a new QA bit flag, including snow detection reversals and detections with increased uncertainty.

- Basic pixel-level QA uses new criteria to indicate the overall quality of the algorithm result.
- The snow cover algorithms and data sets are significantly revised in Version 6

However, the main significant change or revision in C6 was in Aqua products. Since dysfunction of band 6 on Aqua (about 75% of the detectors are non-functional), this band is therefore considered useless in the snow algorithm. A specific Aqua processing was made through an integrated Quantitative Image Restoration (QIR) algorithm (Gladkova et al. 2012) in the MYD10 to restore the missing Aqua MODIS band 6 data and obtain the same snow detection algorithm in both Terra and Aqua using band 6 data in C6, to scientifically usable data for snow detection (Riggs and Hall 2015, Riggs et al. 2015).

3. Methodology

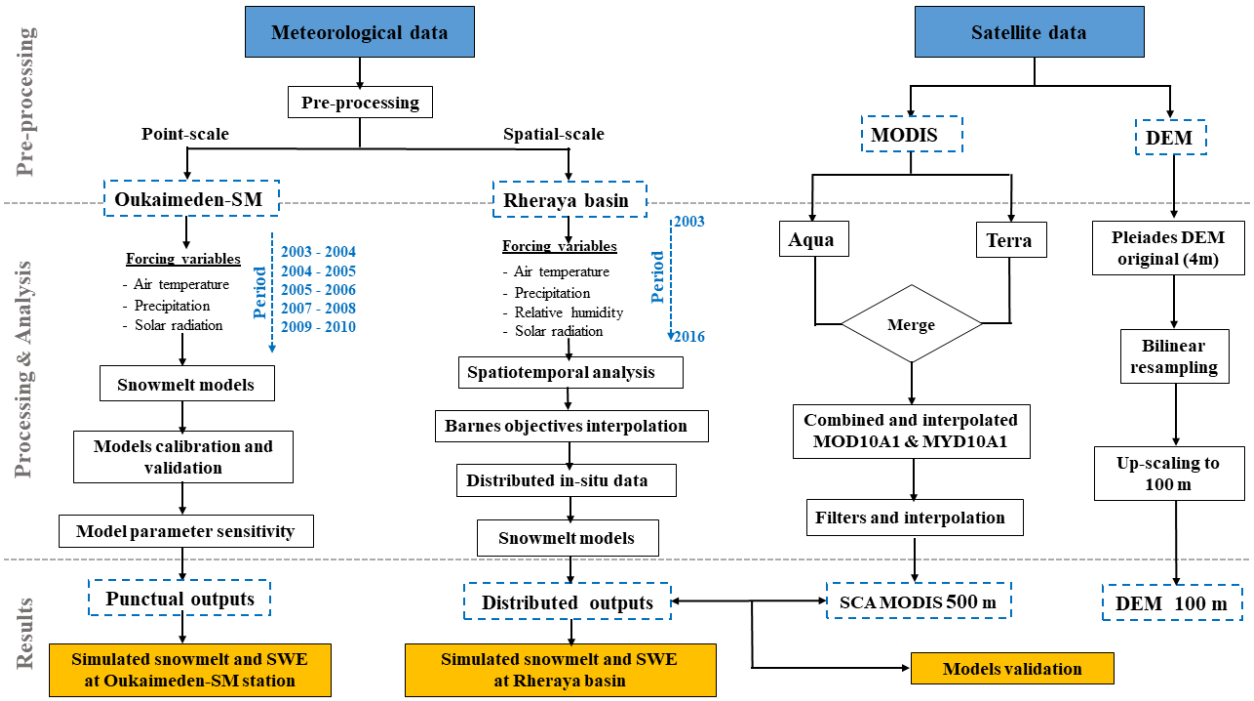

Figure 8: Flowchart of key aspects of the methodology

3.1. Meteorological data pre- and post-processing

3.1.1. Filters and pre-processing

Data pre-processing remains the most important and critical step in any study, which requires special interest and caution. It aims to facilitate the analysis process and to improve the quality of experimental data by appropriately cleaning, transforming, and scaling the entire dataset.

In this study, the preparation of our data was more complicated since we worked in a mountainous area where stations are sparse and measurements are often scarce or/and erroneous (i.e. systematic errors due to either presence of wind or snow, or random errors such as noisy data related to the instrumental measures). In this sense, a daily mean average was derived for all climatic variables available for different time ranges (half-hourly and hourly) at the stations. The original time series were adjusted to a uniform period from 2003 to 2016. Additional pre-processing was performed on the Oukaimeden-SM station, taking into account the large discontinues and erroneous observations. This, includes (i) filters to correct and/or remove any abnormal observation value, (ii) linear regression method to interpolate and fill missing data, and (iii) the merging of summer and winter data, delivered separately, into one series.

3.1.2. Spatiotemporal analysis

Once the data pre-processing step is completed, the data are suitable for analysis. Spatiotemporal variability analysis of climatic variables was performed to determine the relationship of these variables against elevation. Thus, identifying a lapse rate of each variable to spatially distribute data at unknown points when measurements are not available. The analysed variables would include air temperature, relative humidity, and precipitation.

3.1.2.1. Air temperature

Air temperature is the climatic variable most often available from in-situ measurements. In comparison with precipitation, air temperature measurements are much less biased and the interpolation methods are more robust. To investigate the variation of air temperature observations between stations, the inter-annual mean was calculated for all air temperature stations. Figure 9 shows an explicit effect of topography and seasonality between the different stations. For instance, in the Oukaimeden-SM station, the mean monthly air temperatures vary between -2 °C in February to 15 °C in July with a range of 17 °C (seasonality effect). A difference of 1174 m in elevation between the Imskerbour and Oukaimeden-SM stations results in a decrease of 7 °C in the monthly average values in February (topographic effect).

To quantify the magnitude of the lapse rate, a linear regression was conducted between the inter-annual mean of air temperature and elevation (Z) as displayed in Figure 10. Considering that Ta is a linear function of elevation, a high correlation was detected in this present study. The slope value of this linear regression is the temperature lapse rate (TLR) or as called “altitudinal gradient”,

presented in Figure 11 and Table 3. It ranges from -0.59 °C 100 m^{-1} in October to -0.49 °C 100 m^{-1} in June with an annual monthly average of -0.54 °C 100 m^{-1}. Besides, it should be noted here that lapse rates vary throughout the year, it is generally high in spring-summer and low in autumn-winter (Table 3). The mean value is close to the standard environmental temperature lapse rate of 0.65 °C 100 m^{-1}.

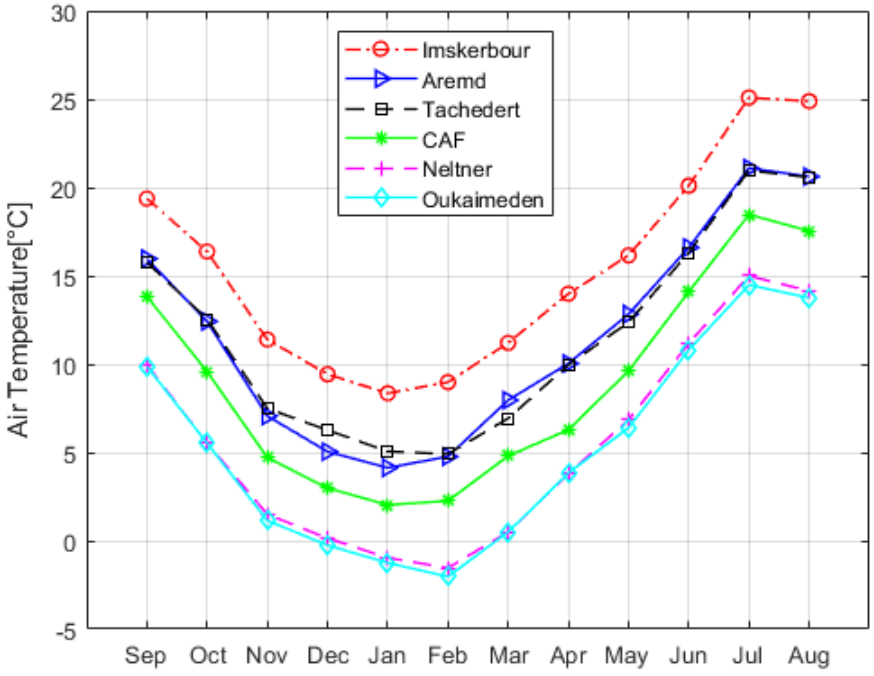

Figure 9: Variability of mean monthly air temperature per station: topography and seasonality effect.

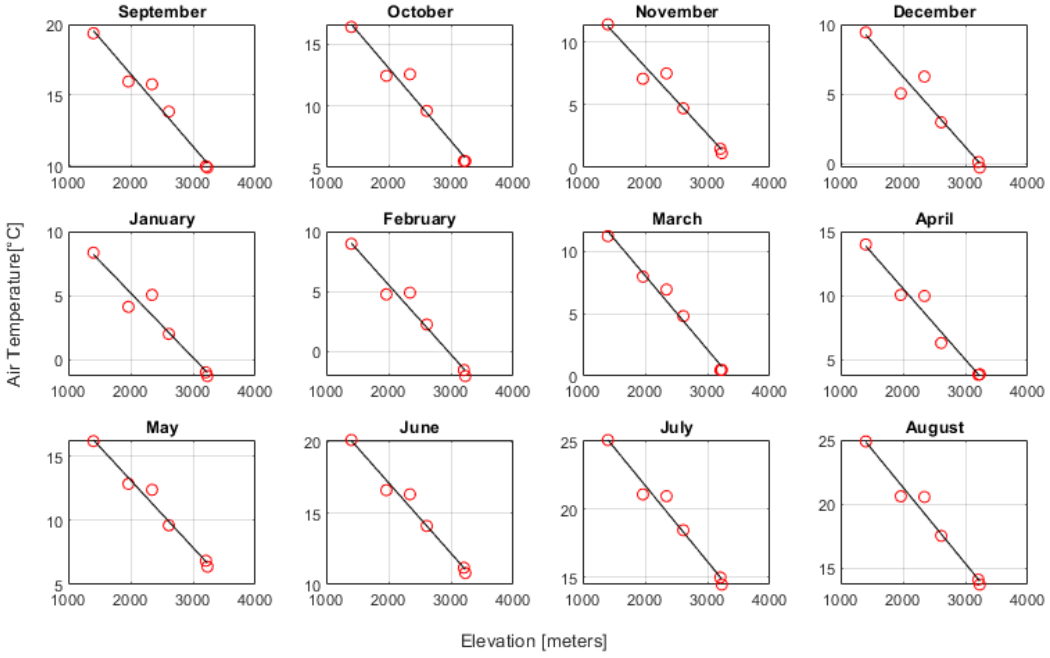

Figure 10: Elevation effect on mean monthly air temperature over Rheraya

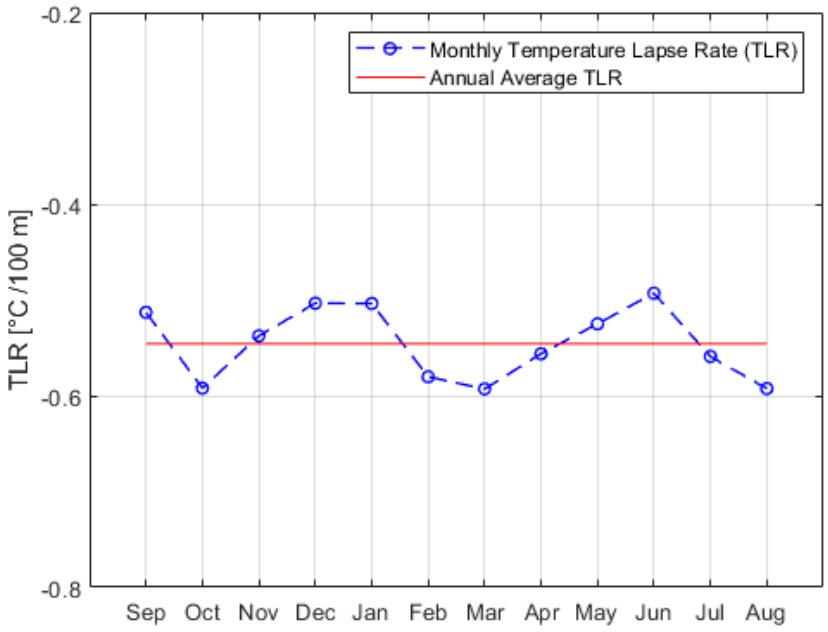

Figure 11: Mean monthly air temperature lapse rate (TLR) variability in Rheraya catchment

Table 3: Mean monthly air temperature lapse rate in Rheraya

	Sep	Oct	Nov	Dec	Jan	Feb	Mar	Apr	May	Jun	Jul	Aug
TLR (°C 100 m^{-1})	-0.51	-0.59	-0.54	-0.50	-0.50	-0.58	-0.59	-0.56	-0.52	-0.49	-0.56	-0.59
Correlation coef "r"	-0.99	-0.98	-0.98	-0.96	-0.97	-0.98	-0.99	-0.98	-0.99	-0.99	-0.99	-0.99

3.1.2.2. Relative humidity

In general, the relative humidity (RH) is a non-linear function of elevation, it is inversely proportional to air temperature. This is clearly represented in Figure 9 vs Figure 12, where air temperature decreases during the winter season from December to the end of February in contrast to the relative humidity that rises during the same season. Therefore, the dew point temperature (T_d) variable is commonly used, instead of RH, for such elevation adjustments. Thereby, a spatiotemporal variability of T_d is investigated below.

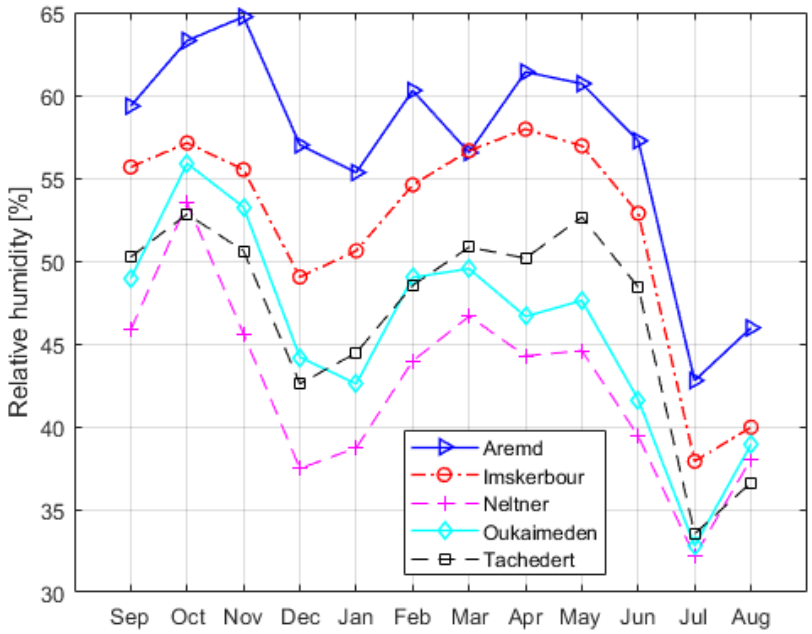

Figure 12: Variability of mean monthly relative humidity per station: topography and seasonality effect

The dew point temperature (T_d) is the temperature at which the air particle would become saturated, i.e. the temperature at which the water vapor of an air particle condenses into liquid water. Its computing requires a combination of simple conversion equations from relative humidity (Kunkel 1989) following this order:

- First, the station relative humidity RH (%) is converted to dew point temperature T_d (°C), using the air temperature T (°C). The saturation vapor pressure, (e_s) in Pa, at air temperature T (°C), is computed as :

$$e_s = a\, exp\left(\frac{bT}{c+T}\right) \quad (8)$$

  Where a = 611.21 Pa, b =17.502, and c = 240.97 °C (Buck 1981)

- Using equation (8) above, the RH equation is :

$$RH = 100\frac{e}{e_s} \quad (9)$$

  Where e is the vapor pressure in Pa

- Then, the dew point temperature (T_d)can be calculated as :

$$T_d = \frac{c\ln(e/a)}{b-\ln(e/a)} \quad (10)$$

  Where a = 611.21 Pa, b =17.502, and c = 240.97 °C (Buck 1981)

The temperature dew point lapse rate should behave as air temperature, taking into account that it is also linear with elevation, and hence all stations in mountains would have lower dew point temperatures than those in the foothills. Figure 13 shows the inter-annual mean variation of dew point temperatures for the different stations in the basin. A difference altitude of only 400 m between 'Neltner' and 'Tachdert' results in a decrease of 7 °C in January. The temperature dew point lapse rate (DPLR) was therefore determined and displayed in Figure 15, it varies between -0.73 in December and -0.58 °C 100 m^{-1}s in August with an annual mean of -0.68 °C 100 m^{-1} (Table 4).

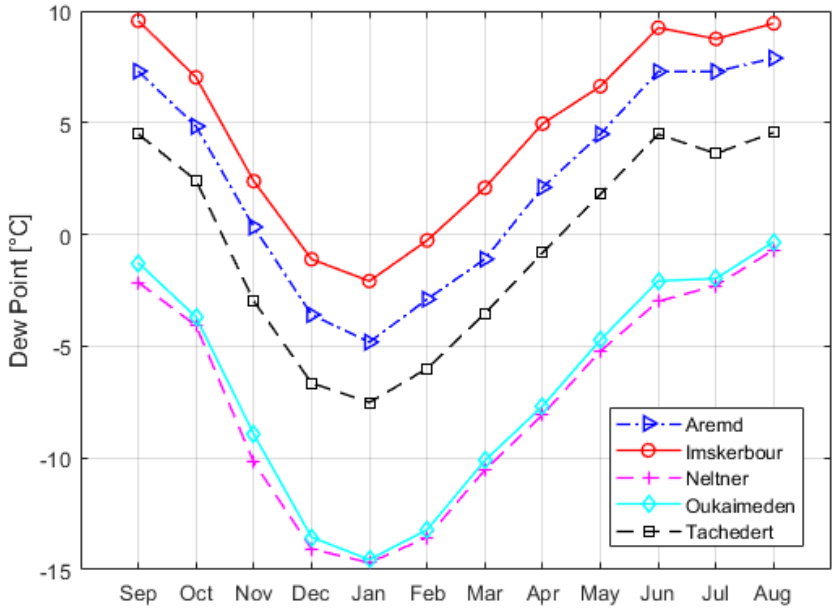

Figure 13: Variability of mean monthly dew point per station: topography and seasonality effect

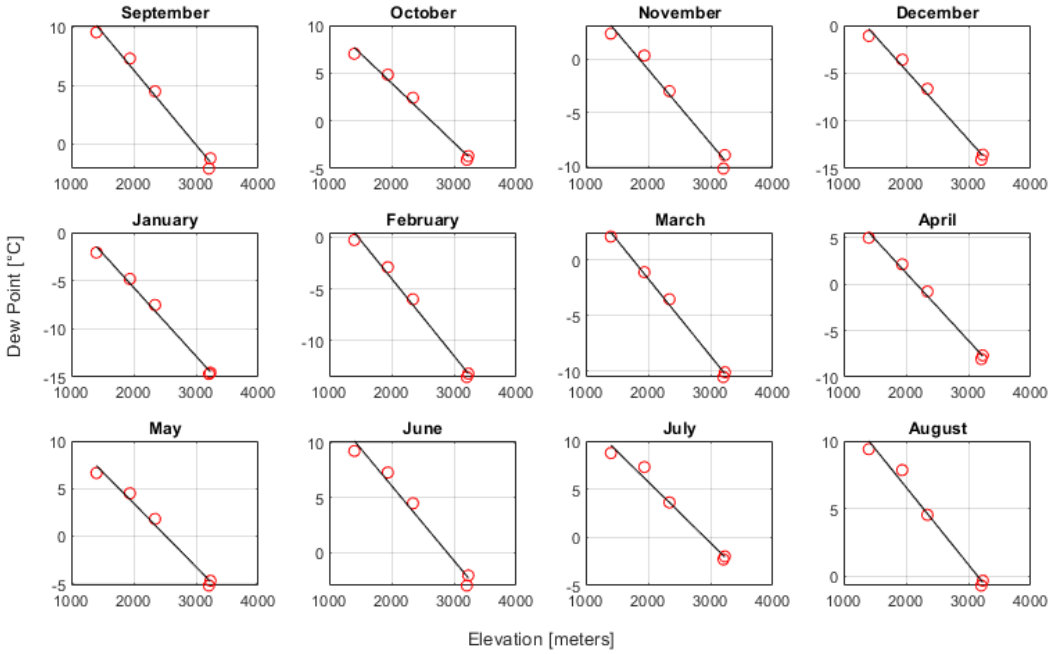

Figure 14: Effect of elevation on mean monthly dew point temperature in Rheraya

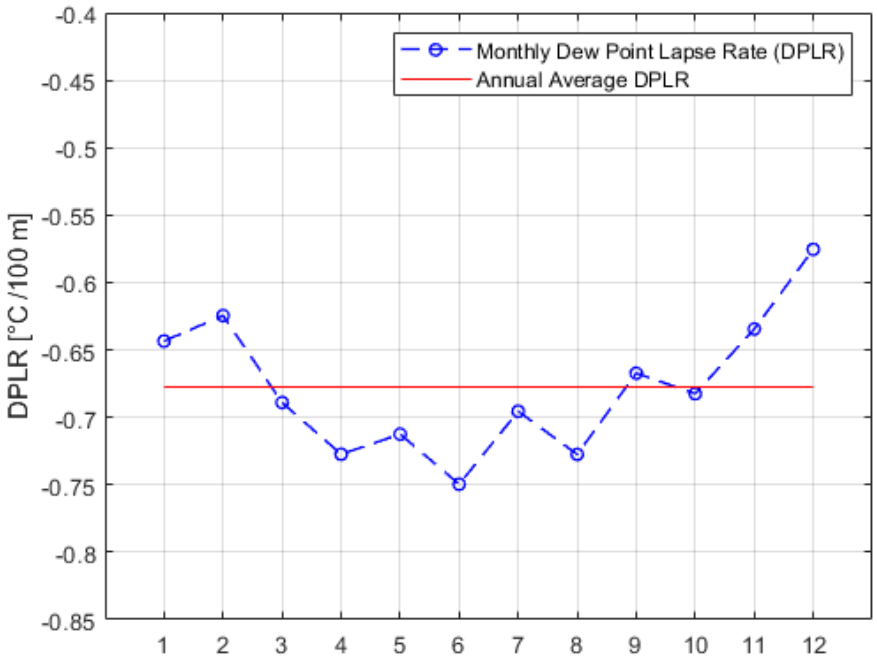

Figure 15: Mean monthly variability of dew point temperature lapse rate in Rheraya

Table 4: Mean monthly dew point temperature lapse rate in Rheraya

	Sep	Oct	Nov	Dec	Jan	Feb	Mar	Apr	May	Jun	Jul	Aug
DPLR (°C 100m^{-1})	-0.64	-0.62	-0.69	-0.73	-0.71	-0.75	-0.70	-0.73	-0.67	-0.68	-0.63	-0.58
Correlation coef "r"	-0.99	-0.99	-0.99	-0.99	-1.00	-0.99	-1.00	-1.00	-0.99	-0.99	-0.99	-0.99

3.1.2.3. Precipitation

Due to the spatiotemporal variability of precipitations, and the lack of ground data in mountainous regions, particularly in the high Atlas Mountains, a special emphasis on this climatic variable will be placed throughout this thesis.

a) Unreliable precipitations

Similar to all other meteorological variables, uncertainties associated with measuring precipitation arises from, (i) the lack of AWS in remote and high-elevation mountain areas, and (ii) gauge undercatch errors. In the high-elevation stations at Rheraya, the use of unheated tipping-bucket rain gauges increases the likelihood of unreliable precipitations mainly during snow events. Because of this, a selection of proper stations has been done, where both Oukaimeden-SM and

Neltner precipitation records were excluded from this analysis.

b) Precipitation lapse rate

To investigate the relationship between precipitation and elevation, various methods were tested to determine a suitable precipitation lapse rate (PLR), such as linear and polynomial regressions. In daily time scale, no significant linear function with elevation is established. However, on a monthly time scale, a linear lapse rate of 1.68 mm 100 m^{-1} was found based on the equation displayed in Figure 16.

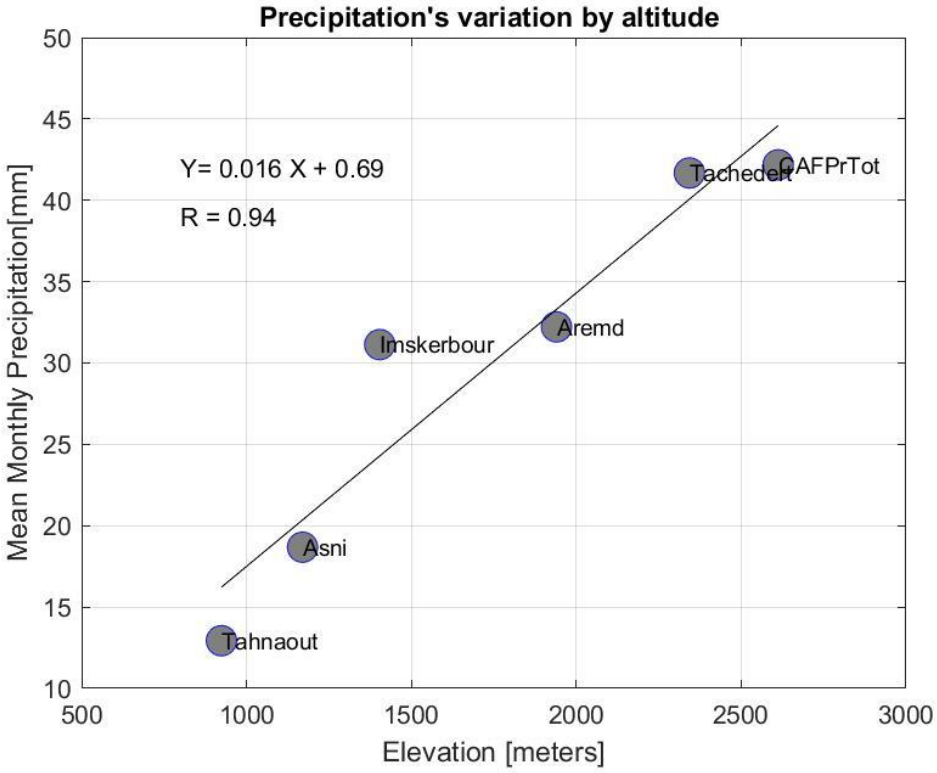

Figure 16: Monthly linear precipitation lapse rate (PLR) at Rheraya

c) Non-linear optimization of PLR

A non-linear precipitation lapse rate was investigated at the Rheraya catchment following Liston and Elder (2006). Taking into account the station availability displayed in Figure 5, two different periods are determined depending on station coverage: (a) whole period including all stations (Figure 17), (b) common period (2007-2010) excluding two stations (Figure 18). As shown in both cases, the PLR is extremely variable within the season and even months. Table 5 summarizes the PLR (km^{-1}) found in both cases with a mean of 0.21 km^{-1} in case (a) and 0.14 in case (b). Then, a

special PLR calibration is required in this thesis, further details are given in Chapter IV, 2.1 Distributed meteorological variables.

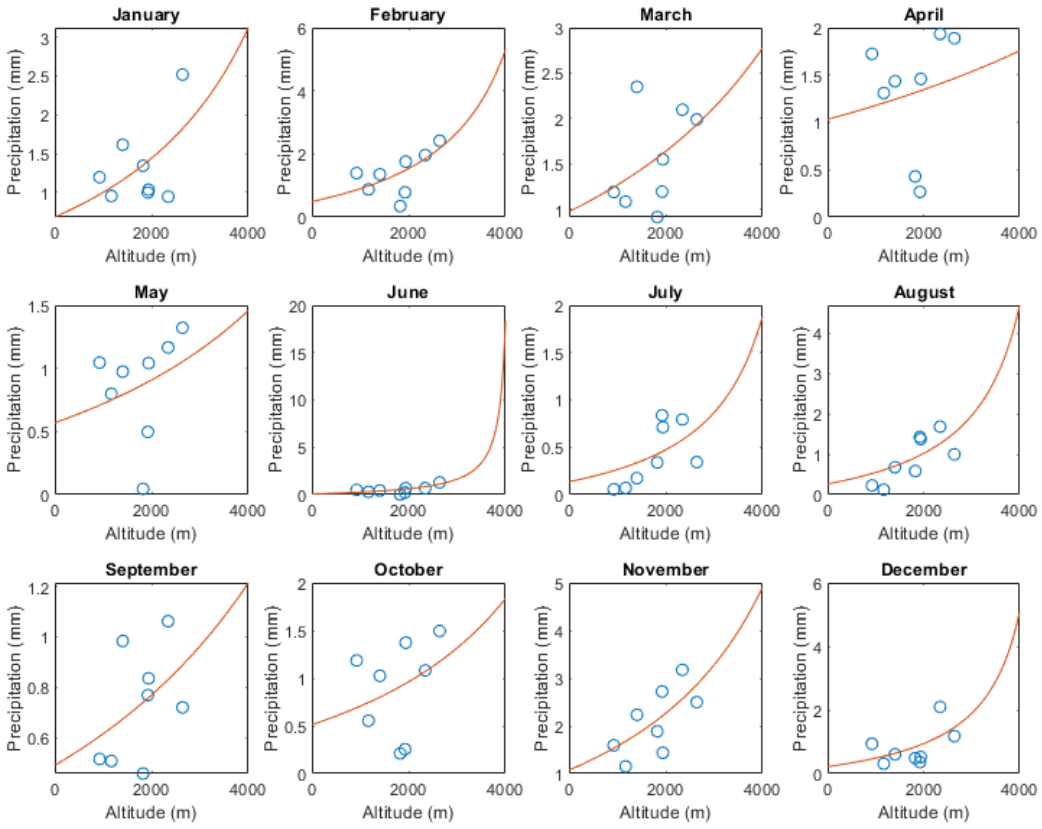

Figure 17: Precipitation lapse rate optimization over the whole period (2003-2016) at all stations

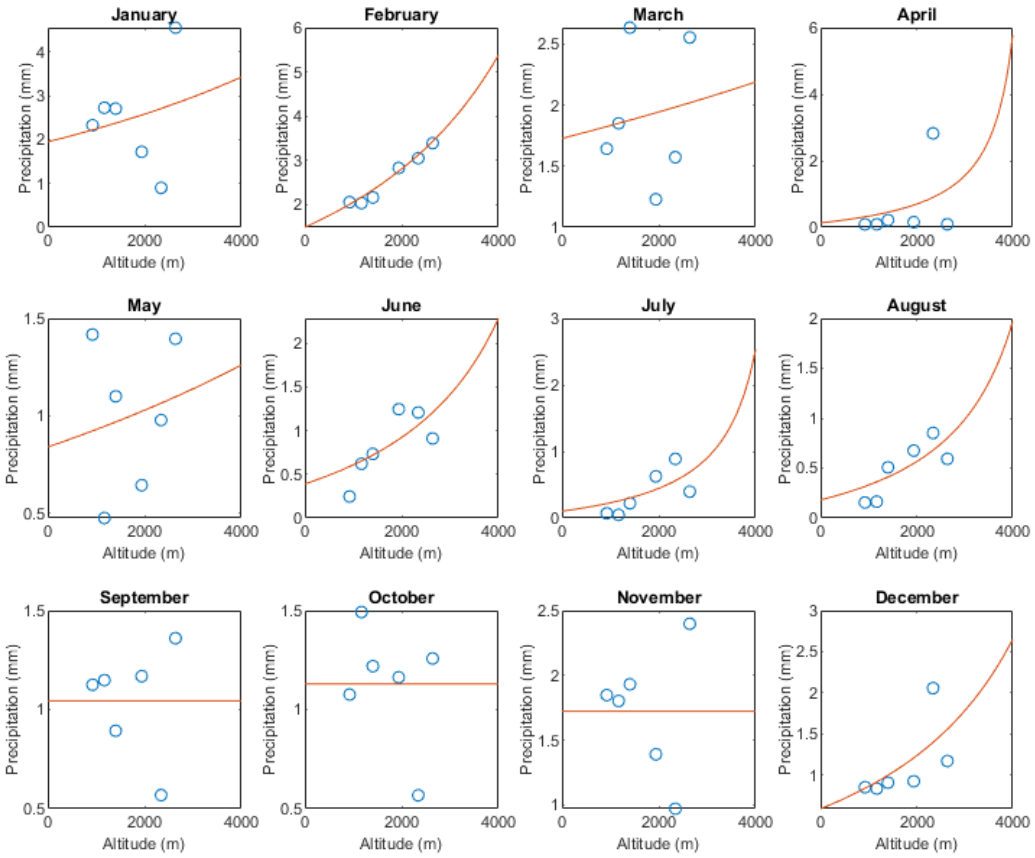

Figure 18: Precipitation lapse rate optimization over the common period (2007-2010)

Table 5: Errors statistics of non-linear PLR optimization at Rheraya

Month	Whole period 2003-2016 All stations			Common period 2007-2010 Excluding 'Matate' and 'Tamatarte'		
	PLR (km^{-1})	RMSE (mm)	R^2	PLR (km^{-1})	RMSE (mm)	R^2
January	0.18	0.44	0.33	0.07	1.10	0.19
February	0.27	0.51	0.44	0.15	0.10	0.97
March	0.13	0.45	0.28	0.03	0.51	0.18
April	0.07	0.59	0.14	0.36	0.94	0.28
May	0.12	0.37	0.18	0.05	0.35	0.19
June	0.42	0.26	0.55	0.21	0.24	0.60
July	0.29	0.25	0.40	0.33	0.23	0.54
August	0.31	0.40	0.53	0.27	0.17	0.65
September	0.11	0.19	0.29	0.00	0.25	0.17
October	0.15	0.44	0.20	0.00	0.28	0.17
November	0.18	0.49	0.51	0.00	0.45	0.17
December	0.33	0.47	0.38	0.18	0.34	0.49
Mean	*0.21*	*0.40*	*0.35*	*0.14*	*0.41*	*0.38*
Std	*0.11*			*0.13*		

3.1.2.4. Solar radiations

Regarding solar radiations at Oukaimeden-SM scale, a parameterizations for the global radiation and snow albedo were developed and calibrated in 2009-2010 as described in 'Chapter III, 2.2 Forcing variables and model calibration' section.

Figure 19 displayed the annual variation of potential solar radiation received on a horizontal surface for Oukaimeden-SM (local scale) latitude by Julian date (01 Jan= 1). The data were generated with equation (15) through "Shading Hock" model

In terms of spatial solar radiation, a distinct spatial distribution of potential solar radiation (I_{pot}) is carried out using the same model mentioned above and described in section'4.2.The potential clear sky radiation model'. Figure 20 shows an example of potential solar radiation maps produced by shading Hock model over Rheraya basin.

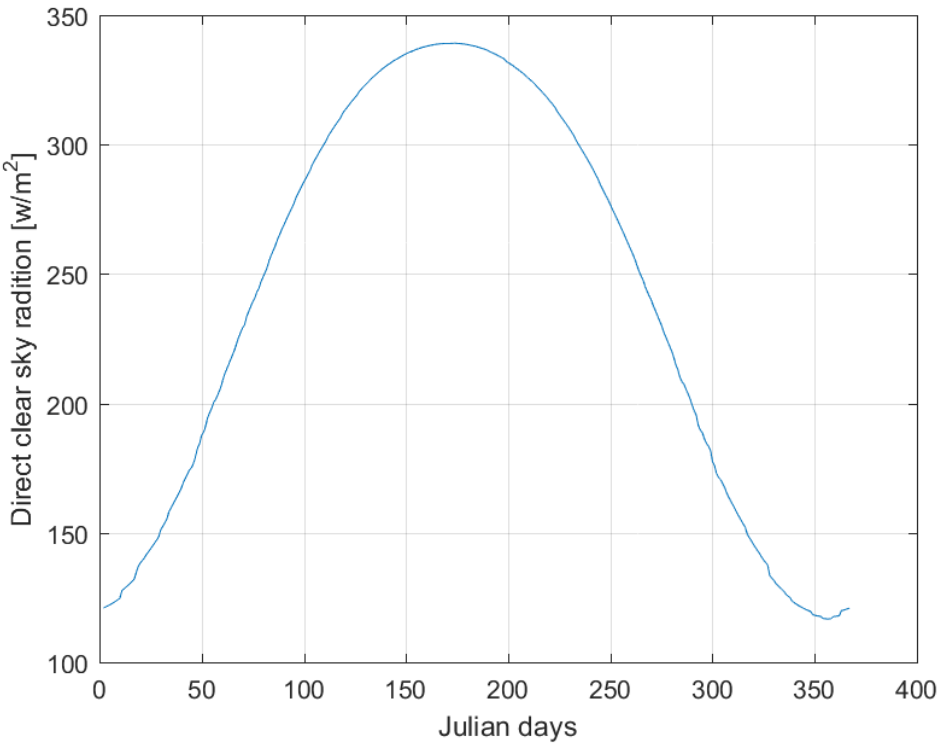

Figure 19: Annual variation of total daily potential clear sky solar radiation (I_{pot})

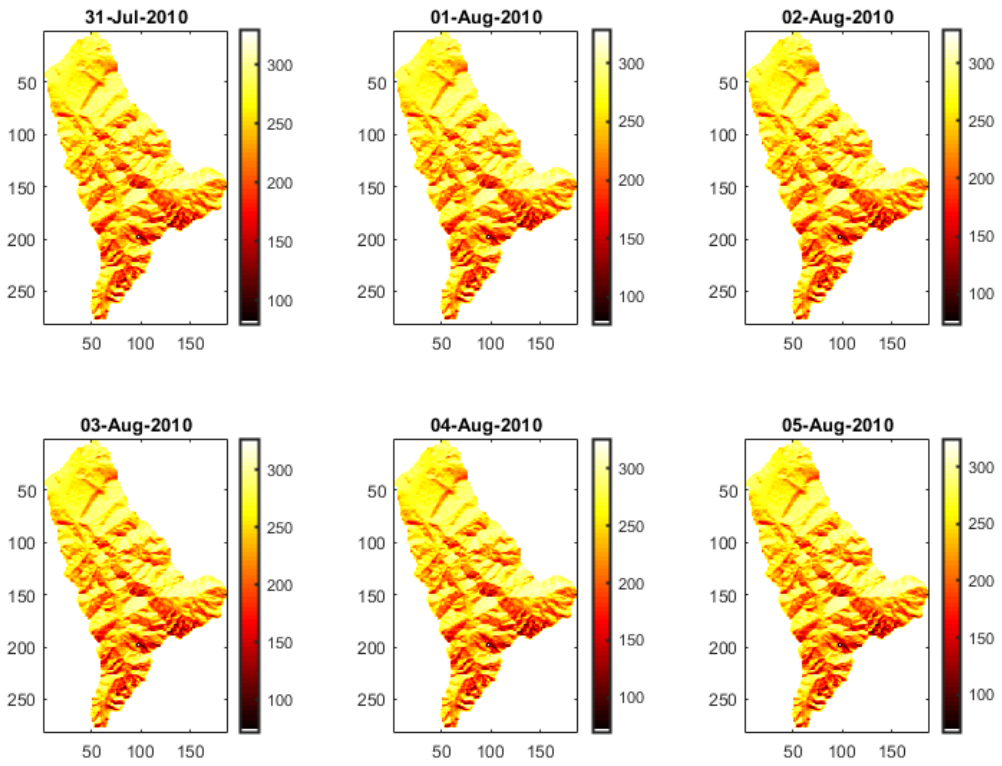

Figure 20: Distribution of potential solar radiation (I_{pot}) over Rheraya basin

3.2. Satellite data pre-and post-processing

3.2.1. Digital elevation model

The DEM was produced at very high spatial resolution after a sequential pre-processing including; alignment, stereoscopy, rasterization, mosaicing and blending, gap-filling of cloud covered area, ortho-image, filtering, and gap-filling of artifacts. Then the DEM was validated for the Rheraya catchment, showing a vertical absolute accuracy of 4.72 m. All these steps are well described by Baba et al. (2019). In this current study, the DEM was aggregated from original resolution 4 m to a coarser 100 m resolution using bilinear resampling method and was projected in World Geodetic System 1984 (WGS84) Universal Transverse Mercator (UTM) coordinate system (WGS_1984_UTM_zone 29N). This resolution was chosen as a good trade-off allowing for a reasonable model computation time while adequately representing the dominant topographic features in the Rheraya catchment.

3.2.2. MOD10A1 and MYD10A1

The datasets are produced in a Geographic projection and were re-projected to the World Geodetic System 1984 (WGS84) Universal Transverse Mercator (UTM) coordinate system using the data transformation options available at NSIDC. One MODIS tile was large enough to cover our study area, a total of 4734 MOD10A1 images and 4760 MYD10A1 images covering 13 years from September 2003 to August 2016, were used in this study (Taking account 5 days before and after each date of moving window).

Many previous studies (e.g. Hall and Riggs 2007, Liang et al. 2008) have demonstrated that MODIS daily snow cover products in clear-sky conditions are in good agreement with ground-based observations or other satellite-based snow cover products with snow agreement reaches 98.2%. However, cloud obscuration remains the main obstacle to using MODIS snow cover products (Parajka and Blöschl 2008, Wang et al. 2008, Xie et al. 2009, Zhou et al. 2013). Getting cloud-free or even reduced cloud percentage of less than 10 % of daily MODIS images remains a challenge. In this sense, various approaches have been proposed to reduce cloud obscuration through numerous approaches, such as altering the cloud mask, separating cloud-masked pixels, and applying spatiotemporal or multi-sensor combinations.

Various previous studies have shown that combining Terra and Aqua observations reduces cloud obscuration (Parajka and Blöschl 2008, Gafurov and Bárdossy 2009, Wang and Xie 2009, Xie et al. 2009, Gascoin et al. 2015), taking into account that the Terra and Aqua satellites have an approximate 3 hours average overpass time difference, during which cloud conditions can change significantly. For example, Gao et al. (2010) reported that combining Terra and Aqua improved cloud filtering, by reducing the influence of transient clouds in daily reflectance data by 11.7% compared to using MOD10A1 alone, and 7.7% compared to using MYD10A1 alone. In this study, the MOD10A1 and MYD10A1 were merged into a combined product called CMXD10A (fig) as follow: (i) on any given day if only one source (either Terra or Aqua) was available it was used for that day; (ii) for days when both products are available, priority was given to the Terra product (e.g. Xie et al. 2009) since the Aqua MODIS instrument provides less accurate snow maps due to dysfunction of band 6 on Aqua (Riggs and Hall 2004, Salomonson and Appel 2006, Gascoin et al. 2015, Zhang et al. 2019). This means that any pixel classified as either cloud, missing, or unclassified in MOD10A1 was filled with the corresponding pixel in MYD10A1 if that pixel had an NDSI value, else the original MOD10A1 pixel classification was conserved (Figure 31).

Subsequently, a spatiotemporal filter was applied to the merged CMXD10A product to fill in missing NDSI data, i.e. pixels classified as cloud, but also those classified as either missing, saturated or unclassified, collectively referred to as 'missing' therein. A spatial filter was first applied only if less than 60% of the mountainous areas (elevations above 1000 m) were missing (Marchane et al. 2015). This filter classifies missing pixels as snow-covered when their elevations are higher than the average elevation of the snowy pixel for the entire basin. Then, a temporal filter was applied to linearly interpolate the remaining missing pixels within a moving window extending 3 days prior and 2 days after the current date. NDSI values in the blended and interpolated CMXD10A product were converted to binary maps of snow cover area (SCA) based on an NDSI threshold of 0.4, following previous studies (Xiao et al. 2004, Marchane et al. 2015, Hall and Riggs 2016), i.e., for each pixel, SCA = 1 when NDSI ≥ 0.4, otherwise SCA = 0 (Figure 31). The blending and filtering procedure reduced the fraction of missing pixels to 0.84%, similar to previous results obtained in the same area by Marchane et al. (2015). The pixel classes in those snow cover images were reclassified into two categories: snow and cloud (Figure 31).

4. Models

4.1. Snowmelt models

Four models of increasing complexity were used to simulate snowmelt at the Oukaimeden-SM weather station site. Model formulation range from the simple, classical degree-day method to different 'enhanced' degree-day methods. Each model is outlined below.

4.1.1. Classical temperature index (TI) melt model

Temperature index models or so-called degree-day models are considered the most classical method for melt modeling due to the widespread availability of air temperature data and their computational simplicity. These models also perform generally well, being generally classified amongst the most efficient models used for melt modeling (Hock 2003). The model has a single coefficient or factor of proportionality, called the "degree-day factor" (DDF, in mm $°C^{-1}$ d^{-1}):

$$M = \begin{cases} \mathrm{DDF} \times T_\mathrm{a} & T_\mathrm{a} > T_\mathrm{T} \\ 0 & T_\mathrm{a} \leq T_\mathrm{T} \end{cases} \quad (11)$$

Where M is the melt rate (mm d^{-1}), T_a is daily mean air temperature (°C) and T_T is a threshold temperature beyond which snowmelt is supposed to occur, fixed at 0°C in this study.

4.1.2. Hock's temperature index melt model (HTI)

To enhance the classical model (TI), the potential incoming direct solar radiation (I_{pot}) for clear-sky conditions, was added as proposed by Hock (1999). In this structure, the melt factor (MF) varies seasonally according to I_{pot}:

$$M = \begin{cases} (\mathrm{MF} + \mathrm{RF} \times I_{pot}) T_a & T_a > T_T \\ 0 & T_a \leq T_T \end{cases} \quad (12)$$

where M is daily melt (mm d^{-1}), I_{pot} is the potential clear-sky incoming direct solar radiation (W m^{-2}), and MF and RF are two empirical coefficients, respectively the melt factor and radiation factor (expressed in mm d^{-1} °C^{-1} and m^2 mm W^{-1} d^{-1} °C^{-1}, respectively).

4.1.3. Enhanced temperature-index (ETI-A) melt model

This enhanced temperature-index melt model includes global radiation (incoming shortwave radiation), which is an important energy source for melt (Hock 2005). This model separates between melting induced by solar radiation and that induced by temperature-dependent energy fluxes (Pellicciotti et al. 2005):

$$M = \begin{cases} \mathrm{TF} \times T_a + \mathrm{SRF_{in}} \times I & T_a > T_T \\ 0 & T_a \leq T_T \end{cases} \quad (13)$$

Where I is incoming shortwave radiation (W m^{-2}), TF is the temperature factor (mm d^{-1} °C^{-1}) and SRF_{in} is the radiation factor (m^2 mm W^{-1} d^{-1}). The index 'in' stands for incoming shortwave radiation, to differentiate from the ETI-B model, described next.

4.1.4. Enhanced temperature-index (ETI-B) melt model

The ETI-B model structure is similar to ETI-A, but considers the net shortwave radiation instead of only the incoming shortwave radiation. This model, proposed by Pellicciotti et al. (2005), is considered the most physical-based of all the aforementioned melt models, as it includes the variability in snow albedo:

$$M = \begin{cases} \mathrm{TF} \times T_\mathrm{a} + \mathrm{SRF_{net}} (1 - \alpha) I & T_\mathrm{a} > T_\mathrm{T} \\ 0 & T_\mathrm{a} \leq T_\mathrm{T} \end{cases} \quad (14)$$

Where α is albedo and I the incoming shortwave radiation (W m^{-2}), and TF and $\mathrm{SRF_{net}}$ are two empirical coefficients, respectively the temperature factor and net shortwave radiation factor (expressed in mm d^{-1} °C^{-1} and m^2 mm W^{-1} d^{-1}).

4.2. The potential clear sky radiation model

4.2.1. Purpose and formulation

The potential clear-sky direct solar radiation (I_pot) is calculated as a function of solar geometry, topography, and a constant vertical atmospheric transmissivity (Hock and Noetzli 1997, Hock 1999) (equation (15)). Its theory involves computations to adjust energy received from the Sun for the time of day, time of year, slope, aspect, and latitude for the watershed or site of interest, taking into account the atmospheric transmissivity (Hock and Tijm-Reijmer 2012).

$$I_\mathrm{pot} = I_0 \, (R_m/R)^2 \;\; \psi a^{(P/P_0 \cos Z)} \;\; \cos\theta \quad (15)$$

Where I_0 is the solar constant (1368 W m^{-2}), R is the distance Earth-Sun, the subscript m refers to the mean, ψa is the vertical clear-sky atmospheric transmissivity (-), or as called the 'bulk' coefficient of transmissivity, generally varies between 0.6 and 0.9 (Oke 1987) (the optimal ψa value using in this study is given at '2.2.1Clear-sky transmissivity' section). P is the atmospheric pressure in Pa and P_0 is standard atmospheric pressure (101 325 Pa), Z is the solar zenith angle, and θ is the incidence angle of the Sun on the surface. The ratio P/P_0 accounts for the effect of altitude (lower air pressure yields higher solar radiation) and the introduction of cos Z in the exponent expresses the variation of the path length with Sun altitude (Hock 1999, Hock and Tijm-Reijmer 2012). Detailed information about

4.2.2. Program « Shading.c ».

In terms of the program, the 'shading Hock' model is designed to predict the spatial distribution of topographic shading and potential solar radiation for selected time intervals. The formulation of calculated potential radiation is described above (equation (15)). Hock and Tijm-Reijmer (2012) have made their whole mass balance model -including 'shading.c'- available as open-source, to facilitate the development of new modules and improve their model. In general, this model can

apply to any location including high latitudes, and for any spatial resolution. Table 6 summarized all mainly particularities of this model.

Table 6: Principal particularities of 'Shading radiation' model of HOCK

Functions	Structure	Limitations
▪ The potential solar radiation can be computed without any meteorological input data. ▪ The DEM is a sufficient raster element required to calculate the topographic shading effects, besides slope and aspect. ▪ The radiation effect refers to clear sky conditions to avoid the need for additional meteorological data.	▪ The model is written in C; allowing ease of application. ▪ All input parameters specific are read from a controlling input file (name list file: 'input.dat') which needs to be adjusted before each location by the user. ▪ No changes in the source code are required when applying the model to another area.	▪ The area should not be too large (<5° in longitude and latitude because solar geometry calculations refer to the geographic coordinates of only one point inside the area.

5. Spatial distribution methods

There is a large variety of spatial interpolation methods used in different studies to estimate unknown meteorological values at specific locations from a specific known point data (e.g. Dingman et al. 1988, Phillips et al. 1992, Daly et al. 1994, Bacchi and Kottegoda 1995). These methods vary from simple to extremely complex. Vicente-Serrano et al. (2003) report that many factors control the method performance such as; the area, spatial scale, and the climatic variable desired .i.e. annual mean temperature is easier than minimum temperatures (Ninyerola et al. 2000, Daly et al. 2002). Moreover, topographic, geographic, and atmospheric factors, determine the spatial distribution of the climatic variable. In the snowmelt and runoff modeling, temperature and precipitation are considered the two most important inputs (Zhang et al. 2013), hence, the spatial distribution of temperature and precipitation when observations are limited is commonly recommended.

5.1.1. Lapse Rate

Considered the most used method to estimate climatic variables at different elevation zones (Dunn and Colohan 1999, Singh 2001), by distributing them from a reference station to the mean hypsometric elevation of each zone. For instance, when air temperature stations at different altitudes are not available or not reliable in high mountain catchments, temperature lapse rate predetermined from historical observations is usually used to interpolate or/and extrapolate temperature from existing stations. Then a linear lapse rate can be computed as shown in equation (16). However, lapse rates can be highly variable across space and time (Richard and Gratton 2001, Rolland 2003, Gupta et al. 2007).

$$T_x = T_{stn} - TLR\ (Z_x - Z_{stn}) \quad (16)$$

Where T_{stn} (°C) is the observed station air temperature at the station elevation, Z_{stn} (m); T_x (°C) is the air temperature at a given elevation, Z_x (m); and TLR (°C m^{-1}) is the temperature lapse rate.

5.1.2. Inverse Distance Weighting (IDW)

One of the most commonly used techniques for interpolation between stations based on the assumption that the interpolating surface is influenced mainly by nearby stations, and less by the more distant stations (Amri et al. 2011). The method concept is based on a weighting of the point data by the inverse of their distance to the estimated point. In other words, it is based on the assumption that the climatic value at an unknown point $Z(x)$ is a distance weighted average of the climatic values at known points $Z(x_1)$, $Z(x_2)$…, $Z(x_n)$, included in a radius around $Z(x)$. The distance (d_i) between $Z(x_i)$ and $Z(x)$ is the weighting factor because, generally, climatic values are more alike between the nearest points than between distant points (Figure 21). This supposes that predictions are obtained from the nearest sampling points, i.e the method has the effect of giving more weight to nearby data points than those farther away (Vicente-Serrano et al. 2003, Hultstrand 2006).

$$Z(x) = \frac{\sum_{j=1}^{n} Z(x_i)\ d_{ij}^{-r}}{\sum_{i=1}^{n} d_{ij}^{-r}} \quad (17)$$

Where $Z(x)$ is the predicted value; $Z(x_i)$ is the climatic value of a neighboring weather station; d_{ij} is the distance between $Z(x)$ and $Z(x_i)$; and r is the exponent of the distance.

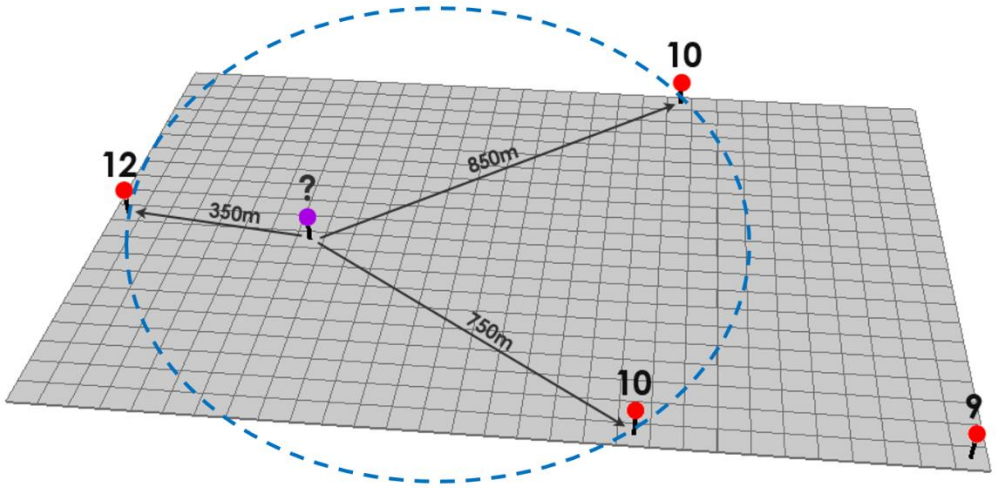

Figure 21: Inverse distance weighting (IDW) method concept

5.1.3. Barnes Objectives scheme

The Barnes scheme is used for interpolating data from irregularly spaced observations to a regular grid using a two-pass scheme (Barnes 1964). It uses a Gaussian distance weighting function to interpolate observations to the regular grid, in which the weight that a station contributes to the grid point decreases with increasing distance from the point. Since the grid point values are weighted averages of the surrounding stations, the gridded values are always less than the maximum and greater than the minimum values surrounding the point, resulting in smoothed station data (Figure 22). The interpolation weights, w, are given by:

$$w = exp\left[-\frac{r^2}{f(d_n)}\right] \quad (18)$$

Where r is the distance between the observation and grid point, and $f(d_n)$ defines a filter parameter whose value ultimately defines how smooth the interpolated field will be. The data spacing and distribution objectively determine the filter parameter value (Liston and Elder 2006). Furthermore, it should be noted that a combination of two interpolation methods is possible, which is the case in this study, we combine lapse rate with Barnes objective methods. More details are given in Chapter IV.

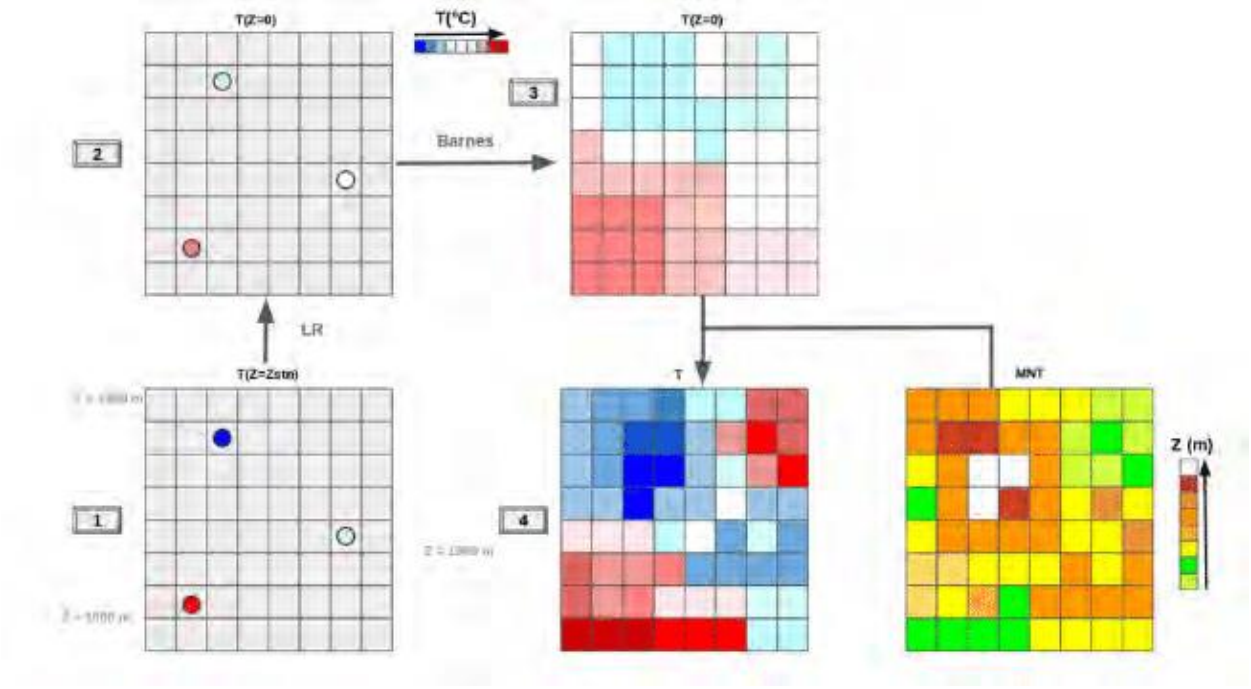

Figure 22: Description of Barnes interpolation method (from MicroMet guide)

6. Evaluation metrics

To assess model performances and calibrated parameters, different evaluation metrics are used throughout this study. One of the classical approaches is to calculate the residuals between observed and simulated through certain objective functions. The choice of the objective function is crucial and has important effects on model results and parameterization. Table 7 summarize all the performance criteria used. One of the well-known and convenient objective functions (Performance criteria) is the Nash-Sutcliffe Efficiency (NSE) (Nash and Sutcliffe 1970) which is generally recognized as a good criterion between other metrics such as the coefficient of determination (R^2) or Root Mean Squared Error (RMSE) which is commonly used in the literature.

Table 7: Criteria equations

Criterion	Definition	Optimal value	Worst value
Nash–Sutcliffe Efficiency (NSE)	$NSE = 1 - \frac{\sum_{i=1}^{n}(Obs_i - sim_i)^2}{\sum_{i=1}^{n}(Obs - \overline{Obs})^2}$	1	$-\infty$
Root Mean Squared Error ($RMSE$)	$RMSE = \sqrt{\frac{\sum_{i=1}^{n}(sim_i - Obs_i)^2}{N}}$	0	∞
Bias	$B = \frac{\sum_{i=1}^{n}(sim_i - obs_i)}{N}$	0	∞
Coefficient R^2	$R^2 = \frac{\sum_{i=1}^{n}((sim_i - \overline{sim})(obs_i - \overline{obs}))^2}{\sum_{i=1}^{n}(sim_i - \overline{sim})^2 \sum_{i=1}^{n}(obs_i - \overline{obs})^2}$	1	-1

CHAPTER III.
PERFORMANCE OF TEMPERATURE AND RADIATION INDEX MODELS FOR POINT-SCALE SNOW WATER EQUIVALENT (SWE) SIMULATIONS IN THE OUKAIMEDEN-SM STATION

The findings of this chapter were the subject of a published paper in the hydrological science journal (HSJ) in 2018:

Bouamri, H., Boudhar, A., Gascoin, S., and Kinnard, C. (2018). Performance of temperature and radiation index models for point-scale snow water equivalent (SWE) simulations in the Moroccan High Atlas Mountains. *Hydrological Sciences Journal, 63(12), 1844-1862. doi:10.1080/02626667.2018.1520391*

1. Introduction

In this chapter, four models of increasing complexity were tested and compared to simulate snowmelt and snow water equivalent at the station scale in the Moroccan High Atlas Mountains. The classical temperature-index (TI) and the three enhanced temperature index (ETI) models (described all in '4.1 Snowmelt models' section) that respectively include the potential clear-sky direct radiation (HTI), the incoming solar radiation (ETI-A), and net solar radiation (ETI-B), were subjected to annual and multi-annual calibration and cross-validated over the period 2003-2010.

The calibration is a key issue in the context of limited data availability, especially in Mountain. Therefore, when used within hydrological models, parameters of empirical melt models are often calibrated at the same time as the hydrological parameters, which can give rise to equifinality problems and hamper the transferability of model parameters (Beven 1993, Beven 2006). There are, however, indications that the parameters of simple temperature-index models can depend

strongly on the climatic conditions of the calibration period, calling into question their transferability over time (Gabbi et al. 2014, He et al. 2014). This is in fact to be expected from simple melt models with few parameters, which do not fully account for inter-annual variations in energy flux partitioning between the atmosphere and the snow surface. The problem of climate dependency of model parameters is likely to be more acute when the period of data available for calibration is short, which can require recalibration of the models for individual sub-periods (Huss et al. 2009). The formulation of 'enhanced' melt models partly seeks to address this shortcoming, by considering additional processes while maintaining a simple model structure and a low data requirement. The increased physical realism of enhanced models may help to alleviate the climate dependency of the calibrated parameters, however at the cost of increased model complexity, i.e. the number of parameters to be calibrated.

The application of empirical melt models in semi-arid regions is further complicated by snow sublimation. Several studies have shown that sublimation can reduce considerably the energy available for melt in such regions (e.g. Hock 2003, Froyland 2013, Gascoin et al. 2013, MacDonell et al. 2013, Herrero and Polo 2016), which can complicate the melt-temperature relationship and the calibration of simple empirical melt models. The semi-arid climate conditions of the Atlas Mountains favour snow sublimation, which can represent a non-negligible fraction of annual snow ablation. Based on energy balance calculations in earlier studies, the sublimation ratio (total sublimation/total ablation) was found to be as high as 44% on the south slopes of the Atlas (Schulz and de Jong 2004) while on the north slopes this ratio was found to be lower, varying between 7 and 20% depending on the year (Boudhar et al. 2016). This large difference in sublimation ratios is consistent with the fact that the northern, windward side of the Atlas intercepts moist air masses from the Atlantic Ocean, while the leeward side is relatively more depleted in moisture and more arid (Knippertz et al. 2003, Schulz and de Jong 2004).

There have been few studies that have explicitly explored the issues of coefficient transferability over time and their dependency on climate conditions. These issues are important in order to guide model calibration practices in a context of limited data availability, which often plagues remote mountain sites such as the Atlas. Therefore, the aim of the present study is twofold:

1. Evaluate the performance of four simplified approaches, ranging from simple temperature-index method to enhanced temperature-index methods to simulate snowmelt and snow water equivalent (SWE) at the Oukaimeden-SM station over the period 2003-2010.

2. Assess the models transferability over time and the climate dependency of the model parameters, using different calibration/validation strategies.

2. Methodology

The meteorological data used in this study were recorded by the automatic weather station 'Oukaimeden-SM', which is already described above in 'Chapter II, 2.1 Meteorological data section'. The studied period is 2003-2010, exactly over the five hydrological years: 2003-2004; 2004-2005; 2005-2006; 2007-2008; 2009-2010.

The 2006-2007 and 2008-2009 years were excluded from the analysis due to unreliable snow data, leaving a total of five hydrological years for analysis.

As continuous SWE measurements are not available at this station, the SWE records previously estimated by Boudhar (2009) were used in this study. Boudhar (2009) converted the snow depth records to SWE using the snow density parameterization of Verseghy (1991); as follow:

$$\rho_s(t + \Delta t) = (\rho_s(t) - \rho_{\max}) \times \exp\{\tau_f \, \Delta t/\tau\} + \rho_{\max} \quad (19)$$

Where ρ_s is the snow density, $\rho_{\max}$ is the maximum snow density, set to 300 kg m^{-3}, Δt = 1 d, and τ_f/τ is the characteristic time (0.24/4800 s^{-1}). The fresh snow density (ρ_{new}, in kg m^{-3}) was calculated by Pomeroy et al. (1998):

$$\rho_{\text{new}} = 67.92 + 51.25 \times \exp\{T_a/2.59\} \quad (20)$$

Where T_a is the air temperature in °C. A mean snowpack density, $\bar{\rho_s}$, was calculated at each time step as the average of the old (ρ_s) and new snow (ρ_{new}) densities weighted by their respective depths. A 0.5 kg m^{-3} °C^{-1} h^{-1} density increase was also applied during melting conditions ($T_a > 0$) to include the effect of meltwater refreezing on snowpack density. If the resulting density value rises above $\rho_{\max}$, equation (19) is not applied and the density is limited to a maximum of 450 kg m^{-3}, based on observations. The density can still decrease afterward following a new fresh snowfall. Snow depths (mm) were converted to SWE (mm) at each half-hour time step using:

$$\text{SWE} = \bar{\rho_s}/\rho_w \times \text{snow depth} \quad (21)$$

Where ρ_w is the density of water (1000 kg m^{-3}). The parameterization was previously calibrated using *in situ* snow density measurements at the Oukaimeden-SM AWS site and found to give fair results with $R^2 = 0.72$ and RMSE = 40 mm (Boudhar 2009). Daily estimated SWE averages were further used in this work and are referred to as "estimated SWE" in the remainder of the text.

2.1. Filtering of wind erosion events

Since the models were forced with measured snow accumulation, any snow deposited by wind was already accounted for. However, as the simple snowmelt routines do not account for snow erosion, any such events would introduce errors in the models and exaggerate the simulated melt rates. While the estimated SWE records at the Oukaimeden-AWS site did not appear to be particularly affected by snow transport during the years studied, even small erosion events during certain years could strongly bias the calibration of the melt models. As our objective is to compare model performance and obtain representative melt parameters, a filtering step was introduced to identify potential wind erosion events and exclude them from the calibration of the melt equations.

Parameterizations for blowing snow probability such as the one proposed by Li and Pomeroy (1997) were developed from, and for, hourly data and is thus not directly applicable to daily data. The filtering step used instead identifies anomalous rises in ablation rate followed by an equally rapid decline over a one or two-day period. The change in ablation rate over time was calculated as the second differential of the estimated SWE record. A threshold of 15 mm d^{-1}, called the wind factor (WF), was used to discriminate 'anomalous' rises in ablation rates from normal conditions. This means that if the ablation rate rose and fell by more than 15 mm d^{-1} over a one or two-day period the ablation event was deemed highly probably to have been caused by wind erosion. In addition, because blowing snow probability decreases sharply over melting snow, only events with negative air temperatures were retained. This also decreases the chance that the filtered ablation events were caused by a rain event. The wind factor, WF, must be specified based on visual interpretation of the d^2SWE/dt^2 plots, as shown in Figure 23 (A). Days that vary below (–WF) and above WF within one or two days are flagged as probable wind erosion events. The detected events correspond well with those that were visually identified on the SWE record (Figure 23 (B)). Sixteen events (days) were detected, which represents 2% of snow days over the 5-year period. Using a non-parametric Mann-Whitney U (rank-sum) test we found that the wind speed was significantly higher, the snow age significantly younger, and the air temperature significantly

lower for the 16 erosion events compared to the remaining snow days, while no significant difference was found for relative humidity ($p < 0.05$). This increases our confidence that these ablation events resulted from wind erosion. Melt was not simulated during these events and the estimated SWE was used during the calibration of the melt equations.

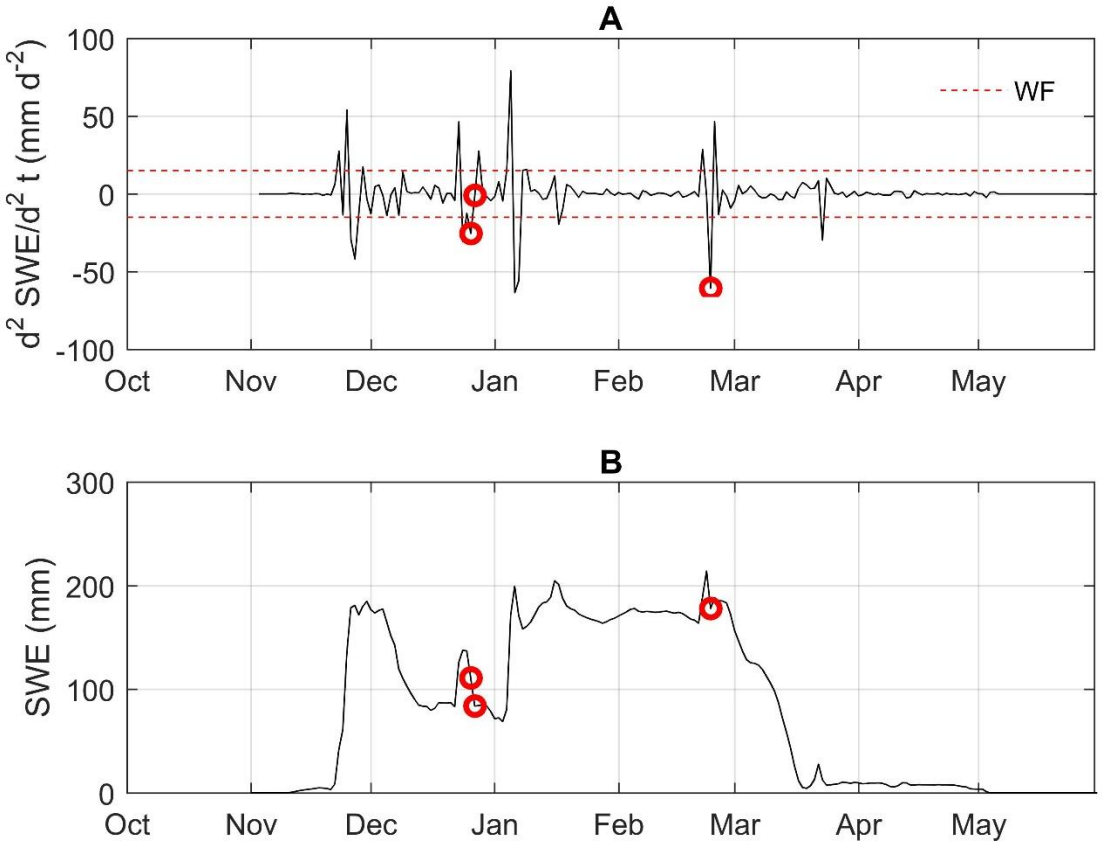

Figure 23: Filtering of wind erosion events from the daily SWE measured in 2007/08. (a) Anomalous increases in ablation rate are identified as those days that successively cross the lower wind factor (–WF) and upper (+WF) threshold within a 1- or 2-day period (circles), which was determined from the second derivation of SWE (d^2SWE/dt^2). (b) Detected erosion events superimposed on the SWE record.

It is worth noting that using the observed accumulation and filtering out wind erosion events will yield the best SWE simulations possible by the melt models. Our goal here is to obtain the best melt model parameters, whose calibration is the least affected by precipitation data quality and/or any snow erosion. Applying these parameters within distributed or lumped hydrological models will thus ensure that melt is correctly simulated, understanding that errors in precipitation data and/or wind redistribution would further affect the spatial simulation of snow cover and result in

reduced model performance compared to the point-scale applications described in this chapter.

2.2. Forcing variables and model calibration

As previously mentioned, some meteorological variables were not available or limited at the Oukaimeden-SM AWS and were thus parameterized. These parameterizations are detailed below.

2.2.1. Clear-sky transmissivity

The vertical clear-sky transmissivity ('ψa' in equation (15), section '4.2 The potential clear sky radiation model') was calibrated by minimizing the root mean square error (RMSE) between I_{pot} and the global radiation measured on clear days, during the year 2009-2010 with reliable measurements. 'Clear' days were classified as those having a mean daily radiation value larger than 80% of the radiation at the top of the atmosphere (TOA). A constant direct (diffuse) fraction of solar radiation of 85% (15%) was assumed for the selected clear days (e.g. Hock and Holmgren 2005). An optimal ψa value of 0.75 was found (RMSE = 14.9 W m^{-2}, NSE = 0.92).

2.2.2. Global radiation

The temperature index models based on incoming and net solar radiation ('I' in equations (13) and (14)) require reliable measurements of global radiation, which in our case were only available for the 2009/2010 season. Hence parameterizations for global radiation and albedo (see next section) were sought in order to apply the ETI-A and B models to the full period. Global radiation was parameterized using the calculated potential clear-sky direct solar radiation and an *R* ratio:

$$R = G / I_{\mathrm{pot}} \qquad (22)$$

Where *R* is the ratio between the global radiation (G) and the potential clear-sky direct solar radiation (I_{pot}), and accounts for the effects of clouds and diffuse radiation (Hock 1999, Hock and Holmgren 2005). If measured global radiation exceeds the calculated direct radiation ($R > 1$), the difference indicates the amount of diffuse radiation. Conversely, measured global radiation less than calculated ($R < 1$) is caused by cloud cover. Atmospheric conditions, especially cloud cover, surrounding topography and the sun position are the major parameters influencing the *R* ratio. As variations in *R* are predominantly due to clouds the *R* ratio is akin to, but different from, the 'cloud factor' used in other studies (e.g. Pellicciotti et al. 2011). In our case, since the clear-sky transmissivity is assumed constant, the *R* ratio also reflects variations in air humidity and aerosol

concentration, which can yield slightly positive *R* values.

Since reliable global radiation measurements were only available for one year, and in order to use modeling approaches as simple as possible, methods relying on commonly observed data (i.e. temperature, humidity, and precipitation) were used to parameterize unmeasured variables such as the *R* ratio and albedo. A parameterization of the *R* ratio was sought based on its relationship with two potential predictor variables: (i) the daily temperature range, which has been previously found to be a good indicator of cloud cover, and (ii) relative air humidity, which could reflect the attenuation by both water vapor and clouds (e.g. Dai et al. 1999, Pellicciotti et al. 2005). Several linear and non-linear regression equations were tested with ΔT and RH as sole predictors, and with both variables as potential predictors.

2.2.3. Albedo

Snow albedo is an important factor governing the amount of solar energy absorbed by the surface. Since albedo measurements were only available for 2009/2010 at the study site, the albedo parameterization developed by Brock et al. (2000) was used to simulate albedo for the whole study period. The parameterization assumes that snow albedo (α_s) decays as a function of time and air temperature, as follow:

$$\alpha_s = p_1 - p_2(\log_{10}(\mathrm{PDD})) \quad (23)$$

Where PDD (mm °C^{-1} d^{-1}) is the positive degree-day sum since the last snowfall. The parameter p_1 represents a typical maximum albedo value for fresh snow, which in this work was fixed to 0.8 based on observations. The parameter p_2 was calibrated on daily albedo observations, by varying its value within a range between zero and one. Prior to calibration, raw hourly albedo observations were filtered to remove values with solar elevation angles less than 20º, or with reflected radiation less than 20 W m^{-2}, this step removed all night time values as well as early/late day values, when low sun angles can cause a large error in radiation measurements (Abermann et al. 2014). As snow deposition on the upward-looking sensor can sometimes cause unrealistically high albedo values. Values larger than 0.9 were set at 0.9. The resulting daytime albedo data were averaged to daily values.

2.3. Model calibration and validation

All melt model parameters were subjected to calibration. A systematic calibration procedure was used, which consisted of varying each parameter value within ranges determined from previous studies (Hock 2003, Pellicciotti et al. 2005, Gabbi et al. 2014). The parameter ranges were then extended if necessary, i.e. if the optimum value found was on the range boundary. The parameter ranges and increments used for the calibration step are listed in Table 8.

The SWE simulations were made at a daily time step during the snow season, from September to May, and compared with the measured SWE. Simulations were evaluated using the Nash–Sutcliffe efficiency measure (NSE). The optimum parameter values were chosen as those maximizing the NSE criterion during the calibration period, and the model performance was assessed during the independent validation period.

Two different approaches were adopted for model calibration and validation: annual and multi-annual calibration. The first approach, annual calibration, consisted of successively calibrating the models on every single year and validating on the remaining years. This is a variant of the split sample (SS) calibration/validation procedure (Klemeš 1986), which consists of dividing the period into two independent sub-periods for calibration and validation. This approach was used to examine the performance of each model when calibrated on a single year of measurements, and to detect possible model overfitting (e.g. Wagener et al. 2003) and its impact on model performance, as well as possible climate dependency of yearly-calibrated coefficients. In the second approach, multi-annual calibration, models were successively calibrated on all four-year sub-periods and validated on the left-out year. This ‘leave-one-year-out’ cross-validation procedure allows the incorporation of natural climate variability in the calibration, and thus should reduce the dependence of parameters on climate conditions of the calibration period (Klemeš 1986, Coron et al. 2012).

Table 8: Parameter ranges and value increments (Δ) used for the calibration of the four empirical models

Model	Parameter	Description	Unit	Range	Δ
TI	DDF	Degree-day factor	mm d^{-1} °C^{-1}	0.00–6.00	0.1
HTI	MF	Melt factor	mm d^{-1} °C^{-1}	0.00–6.00	0.1
	RF	Potential radiation factor	m^2 mm W^{-1} d^{-1} °C^{-1}	0.00–0.05	0.0025
ETI-A	TF	Temperature factor	mm d^{-1} °C^{-1}	0.00–6.00	0.1
	SRF_{in}	Global radiation factor	m^2 mm W^{-1} d^{-1}	0.00–0.12	0.005
ETI-B	TF	Temperature factor	mm d^{-1} °C^{-1}	0.00–6.00	0.1
	SRF_{net}	Net shortwave radiation factor	m^2 mm W^{-1} d^{-1}	0.00–0.16	0.005

2.4. Parameter sensitivity

Sensitivity analysis is often used to calibrate model parameters and assess how parameter uncertainty affects model performance, i.e. how model performance changes when moving away from optimal parameter set (e.g. Paton et al. 2013). The sensitivity of the model performance, as measured by the NSE criterion obtained during multiyear calibration, to parameter variations within their calibration range, was examined graphically for the four melt models studied.

3. Results

3.1. Calibration variables

3.1.1. Global radiation

A positive relationship was found at Oukaimeden-SM between the *R* ratio and ΔT, and a negative relationship between *R* and RH, however with a significant amount of scatter (Figure 24). Based on the coefficient of determination (R^2) and variance ratio (*F*) tests, a second-order polynomial regression with relative humidity as a sole predictor was found to be the best parsimonious predictive model of the *R* ratio (R^2 = 0.52, RMSE = 0.19) (Figure 24 (b)):

$$R = -0.000054\mathrm{RH}^2 - 0.0024\mathrm{RH} + 1.3 \quad (24)$$

Previous studies (Dai et al. 1999) have reported significant relationships between ΔT and cloud cover. On the Arolla and Gorner glaciers, in the Swiss Alps, Pellicciotti et al. (2011) found significant relationships between ΔT and computed daily cloud transmittance factors, with ΔT explaining 33–48% of the cloud transmissivity, depending on the year and location. They also found significant but weaker relationships between RH and cloud transmissivity (R^2 = 13–41%).

They used the ΔT relationship to parameterize the effect of cloud attenuation on the incoming shortwave radiation. In our case, including the diurnal temperature range did not improve the model and this term was thus neglected. Hence while only half the variance of R is explained by equation (24), this results is in line with, and even superior to, previous findings and, consequently, can add significant predictive power to the ETI models, as found, for example, by Pellicciotti et al. (2005).

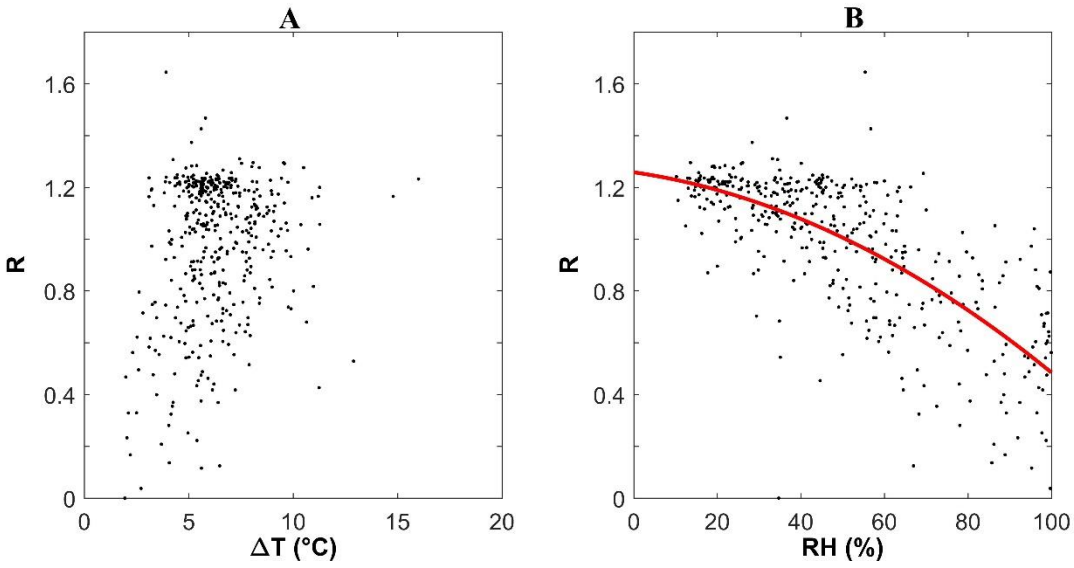

Figure 24: Scatter plot of the R ratio against (a) daily temperature range (ΔT) and (b) relative humidity (RH) with second-order polynomial fit (see equation (24))

3.1.2. Albedo

Globally, the agreement between modeled and measured albedo is fair during the snow season, except during peaks events, where the simulated albedo does not reach some peaks due to the fixed value of p_1 at 0.8 (Figure 25). A calibrated value of 0.21 was found for the p_2 coefficient, with RMSE of 0.098 and NSE of 0.80.

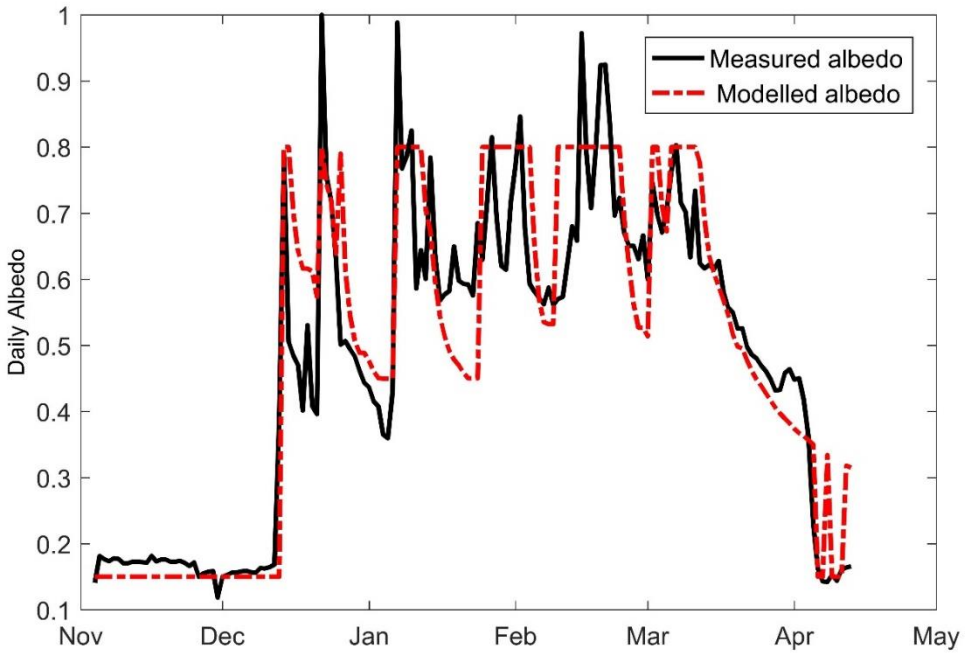

Figure 25: Measured and modeled daily mean albedo at Oukaimeden-SM station in 2009/2010.

3.2. Model calibration and validation

3.2.1. Annual calibration

All models performed equally well during annual calibration (NSE > 0.93) (Figure 26(a)). However, validation statistics show that the model performances outside the calibration period, and hence the parameter transferability, is very unequal among years and models, with the mean validation NSE across years varying from 0.56 to 0.74 (Figure 26(b)). The two models that include radiation (ETI-A) and albedo (ETI-B) show an overall better performance in validation mode (mean NSE of 0.68 and 0.74, respectively) than the TI and ETI models (mean NSE of 0.56). Hence, when calibrated on a single year both ETI models show better time transferability than the TI and HTI models, and the ETI-B model stands out as the best model. The generally poor transferability of yearly models can be further observed in Figure 27: the spread of SWE simulated by models calibrated yearly on other years is sometimes considerable (grey envelope), although it is reduced for the ETI models compared to both TI and HTI models. All models present the worst prediction performance, and hence worst transferability, when calibrated in 2005/2006 and 2009/2010, especially for the TI and HTI models (Figure 26(b)). These two years were the two wettest in terms of mean relative humidity and peak SWE and also ranked first and third, respectively, in terms of

total precipitation measured at the lower CAF station (Table 10, Figure 27). Closer inspection of the simulated SWE record in 2005/06 shows that no melting was simulated in early February while the observed SWE decreased; the cause of this error is unclear but could arise from an unfiltered erosion event, or from errors propagated from the conversion of snow depth to SWE. The positive bias introduced in the simulated SWE in winter was compensated by a higher-than-observed melt rate in the spring (Figure 27). The opposite situation arose in 2009/2010: melt rates appear exaggerated in winter and are compensated by slower-than-observed melt rates in the spring. In both instances, these biases in annual calibration resulted in poor model transferability. Interestingly both ETI models, while also showing a degraded performance, still performed significantly better than the TI and ETI models during those two years, which suggests that these humid years were also probably more cloudy and that models including a global radiation term are better suited to represent the varying energy inputs associated with changing cloud cover between years.

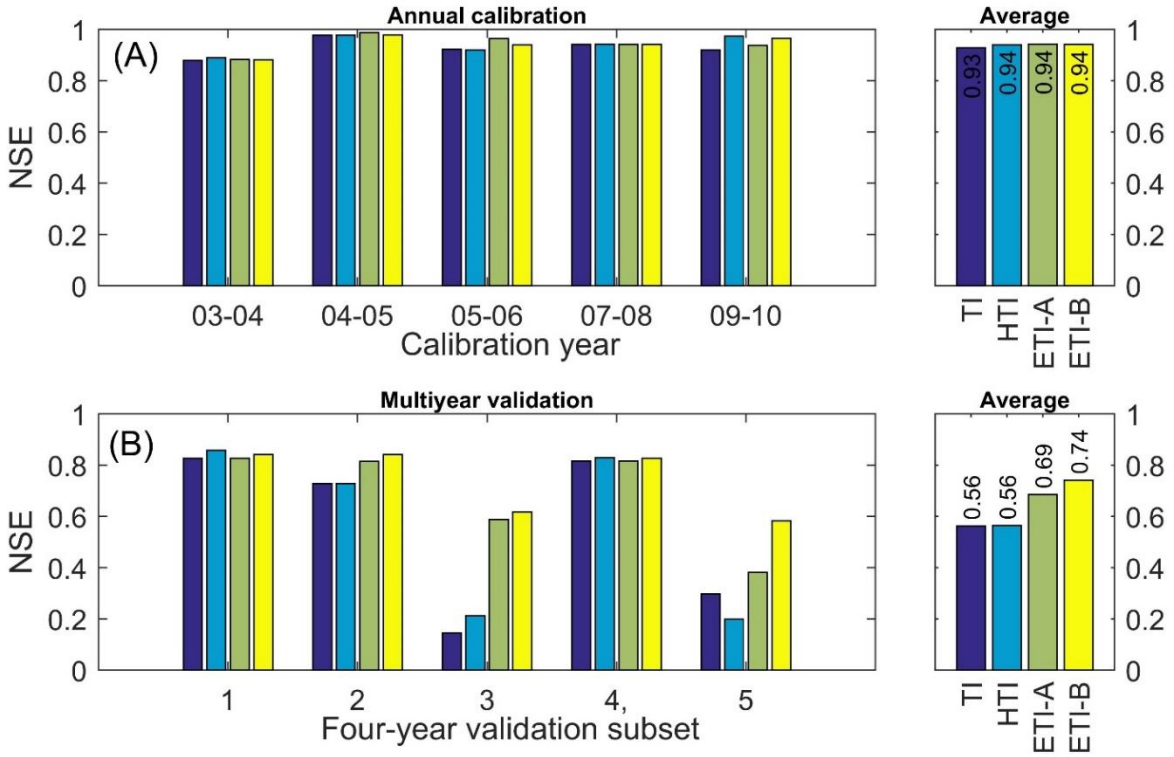

Figure 26: Comparison of the performance of the four melt models using annual calibration. (a) Nash-Sutcliffe Efficiency (NSE) coefficient for annual calibration (left) and mean NSE across years (right); (b) 4-year-out validation NSE corresponding to each calibration year in (a) (left) and mean validation NSE across years (right).

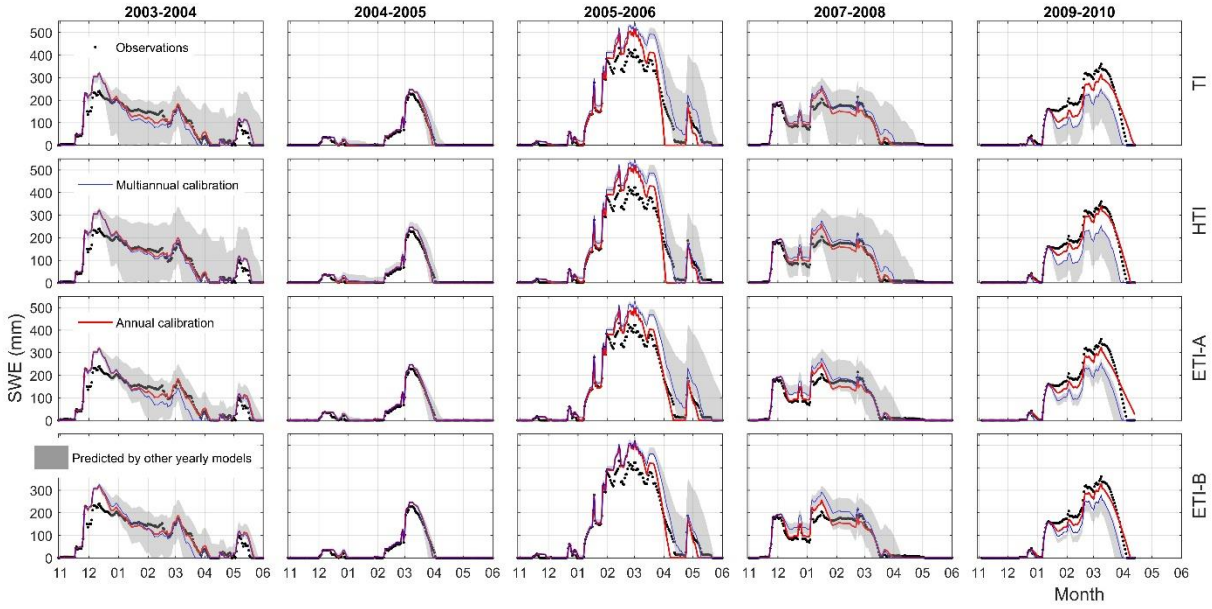

Figure 27: Simulated vs observed SWE using the four melt models for the 2003–2010 period. Each row corresponds to one model and each column to a hydrological year. Black dots: observations; red line: annual calibration (Method 1); blue line: multi-annual calibration (Method 2), shaded area: the range of SWE simulated by models calibrated yearly on other years.

Table 9: Error statistics for the four models from the annual calibration method: RMSE (mm) and NSE

Models	Validated years	Calibrated years: 2003/2004		2004/2005		2005/2006		2007/2008		2009/2010	
		RMSE	NSE	RMSE	NSE	RMSE	NSE	RMSE	NSE	RMSE	NSE
TI	2003/2004	24.1	0.92	75.0	0.23	90.4	-0.12	62.1	0.47	42.2	0.76
	2004/2005	28.4	0.92	15.7	0.97	24.4	0.94	17.2	0.97	35.7	0.87
	2005/2006	110.8	0.68	65.1	0.89	55.7	0.92	72.5	0.87	133.6	0.54
	2007/2008	58.3	0.52	32.1	0.86	90.2	-0.15	20.4	0.94	78.3	0.14
	2009/2010	38.8	0.93	84.9	0.65	144.9	-0.03	68.9	0.77	34.7	0.94
HTI	2003/2004	13.7	0.97	75.0	0.23	90.4	-0.12	55.7	0.58	70.9	0.31
	2004/2005	23.7	0.94	15.7	0.97	24.4	0.94	16.5	0.97	47.9	0.76
	2005/2006	78.4	0.84	65.1	0.89	55.7	0.92	68.3	0.88	107.8	0.70
	2007/2008	60.0	0.49	32.1	0.86	90.2	-0.15	19.1	0.95	112.0	-0.76
	2009/2010	45.6	0.90	84.9	0.65	144.9	-0.03	74.6	0.73	20.0	0.98
ETI-A	2003/2004	15.6	0.97	45.5	0.72	74.5	0.24	59.8	0.51	15.6	0.97
	2004/2005	25.6	0.93	13.2	0.98	28.2	0.92	15.1	0.98	25.6	0.93
	2005/2006	137.1	0.52	78.8	0.84	38.6	0.96	69.6	0.88	137.1	0.52
	2007/2008	66.4	0.38	30.5	0.87	50.0	0.65	19.7	0.95	66.4	0.38
	2009/2010	32.9	0.95	54.2	0.86	105.9	0.45	67.2	0.78	32.9	0.95
ETI-B	2003/2004	15.4	0.97	38.5	0.80	76.8	0.19	60.4	0.50	15.6	0.97
	2004/2005	22.9	0.95	13.3	0.98	27.4	0.92	15.8	0.97	21.8	0.95
	2005/2006	136.1	0.52	86.2	0.81	47.4	0.94	70.8	0.87	138.3	0.51
	2007/2008	68.1	0.35	38.4	0.79	50.5	0.64	19.8	0.94	68.5	0.34
	2009/2010	30.8	0.95	47.8	0.89	105.5	0.45	67.5	0.78	30.3	0.95

3.2.2. Multi-annual calibration

Calibrating the models on 4-year periods forces the models to better represent inter-annual climate variability, which results in a poorer model fit than yearly-calibrated models (mean calibration NSE across years = 0.84–0.88 versus 0.93–0.94, Figure 26(a) and Figure 28(a)). However, the independent validation, as performed with the leave-one-year-out cross-validation, shows that models are more transferable, as seen by the larger mean NSE across years (0.79–0.82) (Figure 28 (b)) and reduced variability in model performance compared to annual calibration (Figure 26(b)). Models calibrated on multi-annual periods (blue lines in Figure 27) yield reasonable SWE simulations for independent years, compared to the spread in transferred yearly-calibrated models (blue lines vs grey envelopes in Figure 27).

Each model was recalibrated on the full five-year period and annual melt rates computed (Table 11). Annual melt rates are on average higher for the HTI and ETI-A models than for the ETI-B

and TI models, but the ETI-B shows less variations between years than the other models, suggesting that including variations in snow albedo helps to better constrain inter-annual variations in melt rates. The sublimation ratio, using the prescribed sublimation rates (see Table 10), averaged 5.3 ± 1.6% over the 5-year period. Due to the oversimplified representation of sublimation in the models, the inter-annual variability is most likely underestimated.

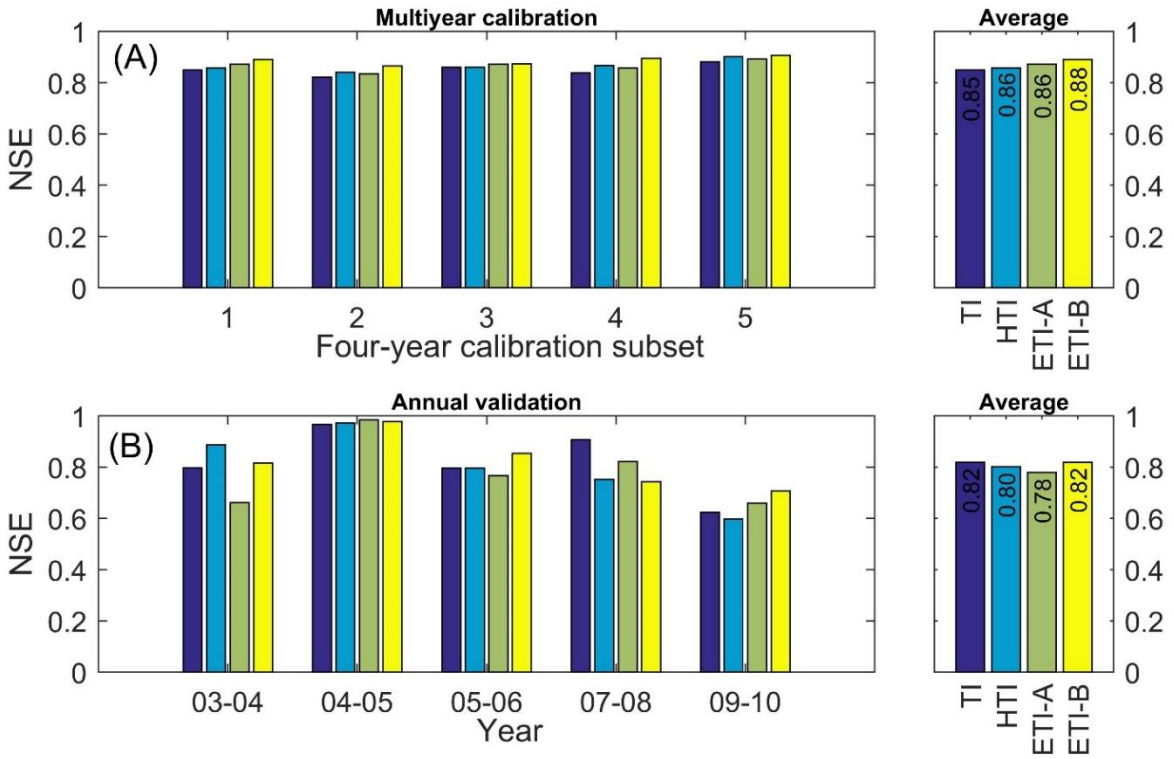

Figure 28: Comparison of the performance of the four melt models using multi-annual calibration. (a) Nash-Sutcliffe Efficiency (NSE) coefficient for each 4-year calibration sub-period (left) and mean calibration NSE by the model (right); and (b) validation NSE on the year left-out from the calibration subset in (b) (left) and mean leave-one-year-out validation NSE by the model (right).

Table 10: Mean climate conditions and sublimation rates calculated for days with snow on the ground. RH: relative humidity; TP: total precipitation.

Year	RH	Air temp.	TP[a]	Peak SWE	Wind speed	Sublimation[b]
	(%)	(°C)	(mm)	(mm)	(m s^{-1})	(mm d^{-1})
2003/04	42.9	1.18	466	240	2.54	0.26
2004/05	52.3	-1.92	168	229	2.72	0.18
2005/06	55.1	0.61	503	430	2.91	0.29
2007/08	44.5	0.74	291	214	2.84	0.21
2009/10	52.6	0.93	312	360	2.67	0.17

[a] at CAF station. [b] from Boudhar et al. (2016)

3.3. Parameter sensitivity and variability

Model parameter sensitivity was analysed in terms of model error as measured by the NSE criterion obtained from multi-annual calibration on the whole 5-year dataset (Figure 29). For two-parameter (enhanced) models, NSE contour plots allow assessing the effect of varying each model parameter on the calibration performance of the SWE simulations. The optimal parameter sets obtained from annual calibration were also overlain on NSE contour plots to investigate their variability with respect to the multi-annual calibration optimum. The three enhanced models are seen to be equally sensitive to both temperature and radiation. However, while an optimum was found for all models using multi-annual calibration, equifinality is also apparent for the two-parameter models, with different combinations of temperature and radiation-related parameters resulting in a high NSE criterion. The optimum is clearest for the ETI-B model (Figure 29(d)).

Optimal parameters obtained from annual calibration (Method 1) show considerable inter-annual variability, with the respective contribution of the radiation and temperature terms changing between years for a given model (Figure 29). Several of the optimal annual parameter sets are found along the high NSE diagonal band found from multi-annual calibration, which suggests that at least some of the inter-annual variability in annual coefficients could be due to equifinality. However, deviations also occur, especially for the additive ETI models, which also suggests that the respective contribution of temperature and radiation to snowmelt may change between years in response to climatic conditions, as found for example by Gabbi et al. (2014).

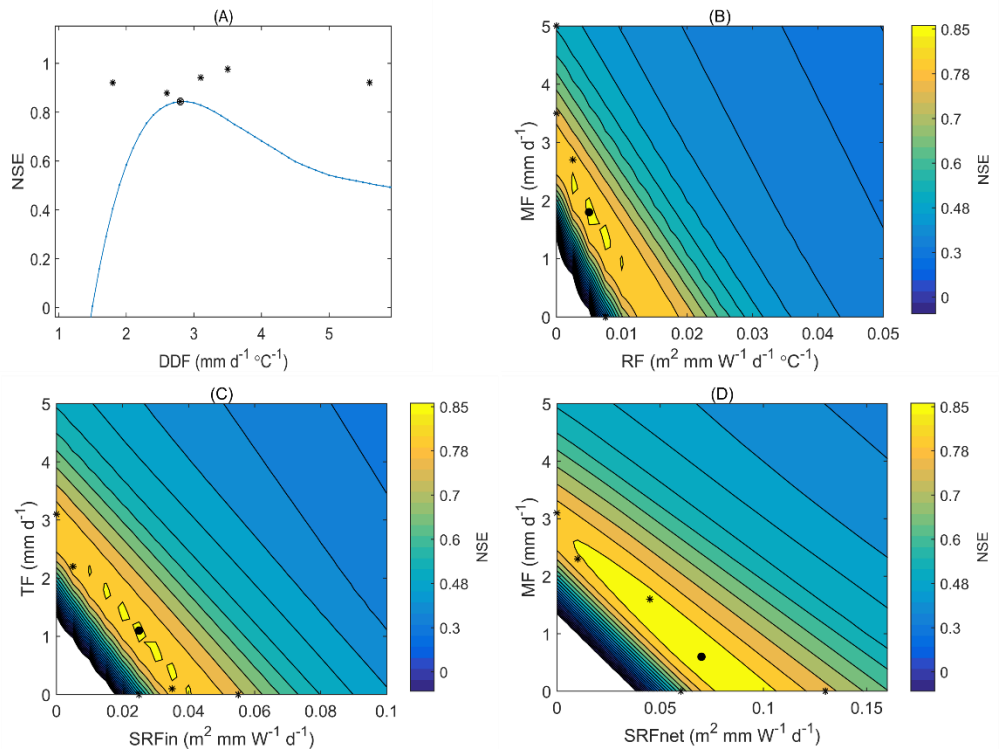

Figure 29: Sensitivity of model performance to parameter variations (see Table 1). The model performance is assessed with the NSE criterion using calibration over the full 5-year period. (a) TI model; (b) HTI model; (c) ETI-A model; (d) ETI-B model. Optimal parameter values from multi-annual calibration are indicated by a black dot; yearly-calibrated parameters are overlaid onto the contour plot and indicated by asterisks (*).

The inter-annual variability of model parameters values resulting from the annual calibration (Method 1) is further investigated in Figure 30. The temperature factor of both the TI and HTI models exhibit a similar tendency over the five studied seasons, increasing until 2005/2006 and decreasing afterward. The pattern is different for the ETI models. Both models show a maximum TF value (3 mm d^{-1} $°C^{-1}$) in 2007/2008. The TF factor is nil in 2004/2005 for ETI-A and in 2005/2006 for both models. The radiation factor (SRF_{in}, SRF_{net}) varies inversely with the temperature factor. Whether these annual variations in model parameters are related to climate conditions prevailing in a given year, or are simply caused by overfitting the models in each single year and/or parameter compensation (i.e. equifinality) is investigated in the next section.

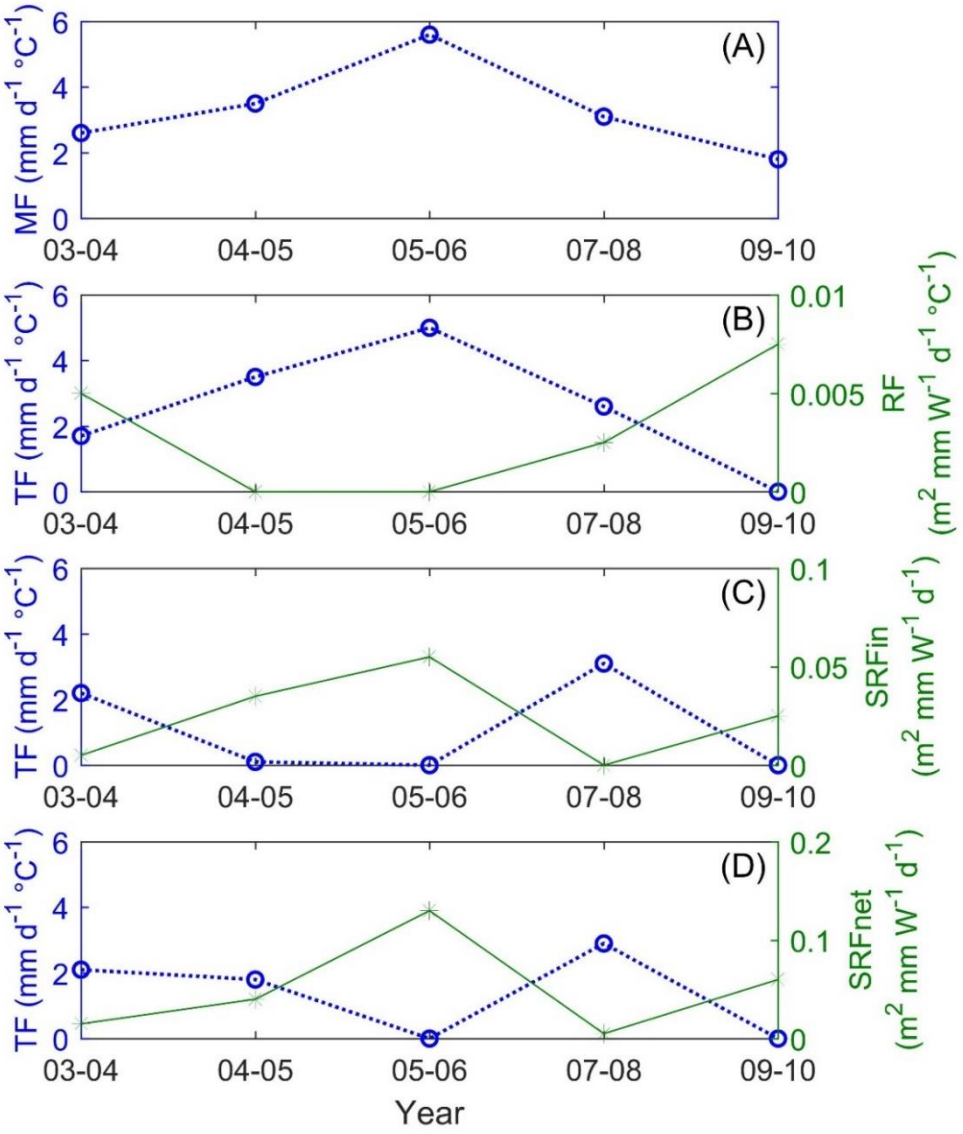

Figure 30: Yearly-calibrated model parameters for the (a) TI, (b) HTI, (c) ETI-A and (d) ETI-B models for five hydrological years.

3.4. Relationship between annual parameters and climate

The dependence of model parameters on climatic conditions was investigated using simple bivariate correlation analysis between the yearly-calibrated model parameters and annual averages of measured meteorological variables (air temperature, relative humidity, total precipitation, wind speed) as well as with the mean daily sublimation rate used in the model formulation (Table 10). The averages were calculated for days with snow on the ground only. The scope of this analysis is

evidently limited by the small number of observations (5 years), but is nonetheless instructive to reveal possible climate control on annual parameters variations. The TF and SRF_{in} factors in the ETI-A model show statistically significant ($p < 0.05$) negative and positive correlation with relative humidity, respectively. The same pattern is found for the ETI-B model, albeit with weaker correlations ($p < 0.10$). For the three enhanced models, the temperature and radiation factors are inversely correlated, reflecting the pattern seen in Figure 30. This parameter compensation is strongest for the HTI and weakest for the ETI-B model.

Table 11: Mean daily melt rates for each year, calculated using the five-year calibrated models. The constant daily sublimation rates listed in Table 10 were used to calculate the sublimation ratios. SD: standard deviation

Year	Melt				All models
	TI ($mm\ d^{-1}$)	**HTI** ($mm\ d^{-1}$)	**ETI-A** ($mm\ d^{-1}$)	**ETI-B** ($mm\ d^{-1}$)	**Mean sublimation ratio ± SD (%)**
2003/04	5.6	6.1	6.1	5.0	4.9 ± 0.4
2004/05	2.8	2.7	3.4	3.4	6.2 ± 0.7
2005/06	4.9	5.3	5.3	5.3	5.6 ± 0.2
2007/08	3.3	3.3	3.7	3.5	7 ± 0.3
2009/10	5.6	5.7	5.8	5.2	2.7 ± 0.1
Mean ± SD	*4.4 ± 1.3*	*4.6 ± 1.5*	*4.8 ± 1.2*	*4.5 ± 1*	*5.3 ± 1.6*

4. Discussion and conclusion

4.1. Model performance and transferability

Taken together our results show that when calibrating models on a restricted dataset such as a single year of measurement, a situation not uncommon at remote sites, enhanced additive models such as ETI are more transferable than simpler models such as TI and HTI, which are predominantly temperature-based models (Figure 26). At a point scale, the sole effect of including a potential radiation term in the HTI is to progressively augment the TF factor as solar radiation increases toward its summer maximum. But, explicit consideration of the atmospheric transmissivity (via the *R* ratio in both ETI models), and snow albedo in the ETI-B, appears to better capture the intra-season variability in melt rate arising from changes in the contribution of shortwave radiation versus temperature-dependent longwave and sensible heat fluxes to the snow surface energy balance. The fact that the additive ETI models are better transferred from one year to another is somewhat surprising given the significant variability of the yearly calibrated

parameters. The explanation may reside in the fact that several combinations of the temperature and radiation factors give similarly acceptable model performance (Figure 29), i.e. equifinal solutions (Beven 2006), and hence a given combination of parameters fitted to one particular year has a good chance to give acceptable predictions when applied to a different year. Conversely, the simpler temperature-dependent TI and HTI models are less able to represent changes in energy fluxes induced by varying cloud cover and albedo, and will thus exacerbate model overfitting when calibrated on short intervals, making them less transferable between years.

However, when calibration is performed on a longer period which incorporates at least some inter-annual climatic variability, all models perform equally well, and no model clearly stands out as optimal (Figure 28). It is noteworthy, however, that the simplest model TI has the second highest performance (NSE = 0.81) behind the ETI-B model (NSE = 0.82). These results are in agreement with those of Pellicciotti et al. (2005), who suggested that ETI models are more transferable over time, whereas e.g. Réveillet et al. (2017) concluded instead that TI models are the most efficient models overall for predicting snow and ice melt on glaciers, when calibrated on a long period (>10 years). Our results tend to corroborate these findings, i.e. that simple TI models, when calibrated on a period long enough to capture inter-annual climate variability, offer good performance at the station scale, comparable and even superior to some enhanced models.

4.2. Parameter variability and climate dependency

Our results showed pronounced inter-annual variability in yearly-calibrated model parameters. Lang and Braun (1990) and Hock (2003) report that under otherwise similar conditions, degree-day factors are expected to increase in response to increased solar radiation input and decreased albedo, and that higher shares of sensible heat flux in the heat balance are generally associated with low degree-day factors and *vice versa*. No such simple relation emerged between the temperature factor of the TI model and climate conditions at the Oukaimeden site. For the ETI-A model, and the ETI-B model to a lesser extent, a positive and negative correlation emerged between relative humidity and the radiation and temperature factor, respectively. Inter-parameter correlations show that radiation and temperature factors in enhanced models compensate each other; this effect is most pronounced for the HTI model, which is rather expected since both factors are used as the multiplier of the temperature (see Equation (12)), different from the two ETI models.

Strong parameter compensation (equifinality) was observed for all the enhanced models (Figure 29, Table 12). The same compensation between temperature and radiation-based parameters was previously reported and discussed by Gabbi et al. (2014) and Réveillet et al. (2017). However, Gabbi et al. (2014) attributed inter-annual variations in parameters to climate conditions, finding for the ETI-B model that the temperature factor was higher and the radiation factor lower in years with reduced solar radiation. They interpreted this relationship to result from a decreased influence of solar radiation, and respective increased influence of incoming longwave and sensible heat fluxes on melt during more humid and cloudy years, in line with previous findings by Carenzo et al. (2009). No such relationship emerged in our analyses; moreover, more humid conditions, which are associated with reduced solar radiation via the R ratio parameterization (see Equation (24)), were found to promote a larger radiation factor and smaller temperature factor in the ETI models, which is opposite to the aforementioned results found by Gabbi et al. (2014). Interestingly, the correlation between relative humidity and both TF and SRF is reduced in the ETI-B model when the albedo is considered (Table 12).

In light of these results, we suggest that much of the inter-annual variability in the yearly-calibrated coefficients are due to model overfitting errors in a given year. Including a solar radiation term (incoming or net) seems to reduce this phenomenon and allows the calibrated models to better transferred to other years. This improved transferability is in part inherited from the equifinality of the temperature and radiation factors, whereas several pairs of parameters give similarly acceptable predictions. However, it also implies that parameters are not well defined, and hence that year-to-year climate variations and/or measurement errors can cause significant differences in the contribution of the melt and radiation factors to snowmelt. This phenomenon may be explained by the partial collinearity of air temperature and incoming solar radiation, an aspect that has been overlooked in the literature when discussing the calibration of empirical melt models. In statistics, collinearity is a phenomenon in which one predictor variable in a multiple regression model can be linearly predicted from the others with a substantial degree of accuracy. It does not reduce the predictive power or reliability of the model as a whole, at least within the sample data, but will increase the uncertainty of model parameters. In such situation, the standard error for the regression coefficient of a given predictor increases by a factor equal to $\sqrt{\text{VIF}}$, where VIF is the variance inflation factor of the predictor, equal to $1/(1-R^2)$, and R^2 is the coefficient of determination of the regression of the predictor against all other predictors (e.g. Draper and Smith 1998). Variables

with VIF > 5 are typically flagged as collinear. The presence of collinear variables in a linear model makes the model more prone to overfitting, i.e. the model coefficients can vary significantly between different calibration samples. However, such model can still yield a good predictive performance outside the calibration interval, especially if the collinearity between the predictors is maintained. Statistical theory does not strictly apply in this case as the model parameters were not derived using the least square method. Nonetheless, the linear structure of the additive ETI models and the systematic calibration procedure that minimizes prediction errors is much akin to the multiple regression framework. Over the whole study period, air temperature was found to be positively and significantly ($p < 0.01$) correlated with the potential ($r = 0.44$), global ($r = 0.65$) and net shortwave ($r = 0.74$) radiation, considering only the days with snow on the ground. This gives VIF factors of 1.73 and 2.21 for the ETI-A and ETI-B models, respectively. This is of course to be expected, as apart from the heat flux from advected air masses the air temperature depends on the longwave radiation emitted from the surface and upward convection of sensible and latent heat, all of which depend, albeit in a complex manner, on the surface shortwave radiation balance. Hence air temperature and solar radiation 'share' a significant fraction of the snowmelt predictive power and as such are partly redundant predictors. The VIF factors only point to moderate, but still significant collinearity of these two variables in the linear ETI models. This may confuse the identifiability of parameters and increase their uncertainty when calibrated on short intervals. This collinearity explains the parameter compensation and equifinality observed in this study (Figure 30, Table 12) and probably that observed in previous ones (Gabbi et al. 2014). The fact that both ETI models were found to be better transferred to other years when calibrated yearly can be explained on the one hand by the true, non-redundant predictive contribution of the solar radiation term, and on the other by the fact that the collinearity between air temperature and solar radiation is maintained in other years.

Table 12: Pearson correlation coefficients between climatic variables and annual model parameters.

Climatic variables & Parameters	**TI**	**HTI**		**ETI-A**		**ETI-B**	
	DDF	**TF**	**RF**	**TF**	**SRF_{in}**	**TF**	**SRF_{net}**
Air temperature (°C)	–0.19	–0.38	0.61	0.41	-0.37	–0.03	–0.06
Relative humidity (%)	0.47	0.31	–0.31	–0.93**	0.93**	–0.87*	0.88*
Total precipitation (mm)[a]	0.74	0.68	–0.64	-0.11	0.47	–0.18	0.52
Wind speed (m s^{-1})	0.39	0.20	0.10	0.08	0.15	–0.25	0.39
Sublimation (mm d^{-1})	0.65	0.64	–0.44	0.40	0.04	0.24	0.16
Inter-parameter correlation	n.a.	–0.95**		–0.87*		–0.86*	

[a] at CAF station. $^{**}p < 0.05$ $^{*}p < 0.10$

CHAPTER IV.
ADDED VALUE OF SOLAR RADIATION IN SNOWMELT MODELS OVER THE RHERAYA SUB-BASIN

The results of this chapter were subjected to a submitted paper in the Frontiers in Earth Science journal.

Bouamri. H**,** Kinnard, C, Boudhar, A., Gascoin, S., L. Hanich, and A. Chehbouni. (2020). MODIS does not capture the spatial heterogeneity of snow cover induced by solar radiation. *Frontiers in Earth Science DOI: 10.3389/feart.2021.640250*.

1. Introduction

Representing the spatial variability of snow cover within distributed snowmelt models for hydrological applications remains challenging, especially in mountainous areas where the snow distribution depends on complex relationships between meteorological conditions and the surrounding landscape, primarily topography (Anderton et al. 2004, Molotch et al. 2005, DeBeer and Pomeroy 2009, Grünewald et al. 2010, Clark et al. 2011). In this sense, various studies have shown that elevation, slope, and aspect play a crucial role in determining the spatial variability of snow processes (Lehning et al. 2006, Letsinger and Olyphant 2007, López-Moreno and Stähli 2008). Interactions between topography and solar radiation strongly modulates the shortwave radiation balance and produce considerable shading effects, especially in high relief landscapes (e.g. Olyphant 1984). While simple TI models only consider the elevation dependence of temperature to model the heterogeneity of snowmelt rates, adding solar radiation allows to explicitly include the effect of topography on melt and as such to better represent the snow cover heterogeneity (e.g. Cazorzi and Dalla Fontana 1996, Zaramella et al. 2019). Indeed, previous studies have shown that including solar radiation improved the performance of spatially-distributed melt models for predictions of glacier mass balance (Gabbi et al. 2014), snow cover area (Cazorzi and Dalla Fontana 1996, Follum et al. 2015) and streamflow from snow-fed basins (Brubaker et al. 1996, Follum et al. 2019). Given the larger computational cost entailed to calculate

spatially distributed radiation fields, it is important to assess their relevance for estimating snowmelt with conceptual models aimed for operational hydrological applications.

Including solar radiation in distributed snowmelt models raises the question about the appropriate scale (resolution) to run models and the suitability of available data to validate them (Baba et al. 2019). While distributed empirical models can be run at high spatial resolutions (<1 km) over large catchments (> 1000 km^2), few observations are usually available to validate spatial simulations explicitly. Snow depth maps from repeat lidar surveys (Painter et al. 2016) and satellite photogrammetry (Marti et al. 2016) are becoming increasingly available, but they remain rare, so that snow cover area (SCA) maps often represent the sole source of spatially-distributed snow information to validate distributed snow models. Snow cover maps derived from the Moderate-Resolution Imaging Spectroradiometer (MODIS) sensor on board the Terra and Aqua satellites, available since 2000 and 2002 respectively, have been at the forefront of distributed snow model calibration and validation efforts (Parajka and Blöschl 2008, Finger et al. 2011, Franz and Karsten 2013, Gascoin et al. 2013, Duethmann et al. 2014, He et al. 2014). However, its spatial resolution (~500 km) may often be larger than the resolution of key processes, such as topographic radiation loading and snow drifting.

The following chapter examines the added value of including different treatments of solar radiation within empirical snowmelt models with a focus on:

1. Benchmark the performance of enhanced temperature index (ETI) models including different parametrizations of solar radiation, relative to the reference temperature index model (TI) to simulate snowmelt, SWE and SCA within the Rheraya basin over the 2003-2016 period.

2. Investigate scale issues arising when using MODIS snow cover area maps for model validation.

This study can be used to complete our previous results at the local scale in Oukaimeden-SM station, and helps our understanding of the spatial variability of snow cover in the Moroccan High Atlas Range.

2. Methodology

The half-hourly meteorological observations retrieved from the different weather stations in the Rheraya catchment were averaged to daily interval for the entire study period, from 2003 to 2016; all the pre- and post-processing steps followed are detailed in 'Chapter II, 3.1 Meteorological data pre- and post-processing' section.

2.1. Distributed meteorological variables

Relative humidity (RH) observations were converted to dew point temperature (DP) following Liston and Elder (2006) (Equations (8),(9) and (10)), since RH is considered a non-linear function of elevation. Then the mean monthly lapse rates for air temperature (Ta) and dew point temperature (DP) were determined by linear regression of these variables against elevation. The both lapse rates used are described in '3.1.2 Spatiotemporal analysis' section.

To distribute Ta and DP observations, station observations were first adjusted to a common elevation using the calculated lapse rate for each variable, and then spatially interpolated to the entire basin using the Barnes objective analysis scheme, following Liston and Elder (2006) (method description in '5.1.3 Barnes Objectives scheme' section). It is worth noting that the Barnes method was chosen in this study after a comparative analysis over Rheraya basin of both interpolation methods, the nearest neighbor and Inverse Distance Weighting. The results showed that Barnes method results in smoother gridded fields and reduced errors compared to other mentioned methods. The interpolated values (Ta and DP) are then lapsed back to their original grid elevation using the same lapse rate, and the DP reconverted to RH.

Precipitation was spatially distributed by combining spatial interpolation with a non-linear lapse rate, following Liston and Elder (2006). First, precipitation observations are interpolated to the model grid using the Barnes objective analysis scheme. A reference topographic surface is constructed by interpolating the station true elevations (as measured by GPS) using the same method. The modeled precipitation rate P_x (mm d^{-1}), at a grid point x with elevation Z_x is computed as:

$$P_x = P_0 \times \frac{[1 + \mathcal{X}\ (Z_x - Z_0)]}{[1 - \mathcal{X}\ (Z_x - Z_0)]} \tag{25}$$

Where P_0 is the interpolated station precipitation, Z_0 is the interpolated station elevation, and $\mathcal{X}$ (mm km^{-1}) is the precipitation lapse rate, or 'correction factor' (Liston and Elder 2006). This enhancement factor $\mathcal{X}$ is referred to as the 'precipitation lapse rate' (PLR) hereafter. An interpolated topographic reference surface (Z_x) is used rather than a fixed reference because the precipitation adjustment function (equation (25)) is a nonlinear function of elevation (Liston and Elder 2006).

Due to the large spatial and temporal heterogeneity of observed precipitation in Rheraya, a specific calibration of PLR was sought. A range of 0.21- 0.35 km^{-1} was used based on the lapse rate value fitted to station observations (described in sub-section '4.1.2 Spatiotemporal analysis (c), Chapter II') and the highest typical winter value set by Liston and Elder (2006) and also found by Baba et al. (2019) in the Rheraya basin. The calibration-validation procedure was performed on the simulated snow accumulation, derived from positives SWE changes at the Oukaimeden-SM AWS and compared with *in-situ* SWE observations available at the same station. PLR was calibrated over a lumped 3-years period (2003 until 2006) and validated separately on the remaining two years (2007-2008, 2009-2010).

The extrapolation of precipitation using equation (25) can result in unrealistically large accumulation rates at high elevations where there are few stations to constrain precipitation. Several studies have shown that while precipitation typically increases with elevation in mountain basins due to orographic uplifting of air masses, this increase can cease and precipitation even decreases passed a certain elevation (Alpert 1986, Roe and Baker 2006, Eeckman et al. 2017, Collados-Lara et al. 2018). This is caused by the progressive depletion of moisture available for condensation within the rising air mass. As such, it is crucial in hydrological modeling to limit the vertical extrapolation of precipitation to avoid artificial snow build up at high elevations. In this sense, Liston and Elder (2006) limited the difference between the actual (Z_x) and interpolated (Z_0) station elevation ($\Delta Z = Z_x - Z_0$) to a default maximum value (ΔZ_{max}) of 1800 m. In this study, this parameter was subjected to a calibration/validation procedure against the MODIS SCA maps for all melt models. ΔZ_{max} was calibrated on odd years within a 300-1800 m range and validated on even years for each model in order to reduce the climate dependency of the calibration period (Arsenault et al. 2018). The validation was done using the optimal parameter for each model as well as with the mean of the optimal parameters of each model (mean ΔZ_{max}).

Regarding the potential clear-sky direct solar radiation, it was calculated as a function of solar geometry, topography, and a constant vertical atmospheric transmissivity following Hock (1999), and includes topographic shading (Equation (15)). Global radiation is calculated using a cloud factor parameterization based on relative humidity (Equation (22) and (24)) and the net radiation uses an albedo parameterisation based on accumulated positive degree days (Equation (23)) (further details are given in Chapter III).

2.2. Rain/snow partition

Determination of the precipitation phase has a large influence in hydrological modeling, especially in mountain areas (Yasutomi et al. 2011, Marks et al. 2013). Various approaches based on air temperature variable have been used, such as a single air temperature threshold (e.g. Fassnacht et al. 2013) or a varying snowfall fraction between two air temperature thresholds (e.g. Marks et al. 2013, Feiccabrino et al. 2015). This linear transition technique was used for the rain-snow partition in this work. The snowfall fraction is linearly interpolated between a temperature threshold for rain T_{rain} (°C), and a temperature threshold for snow T_{snow} (°C) (Tarboton and Luce 1996, McCabe and Wolock 1999, Moore et al. 2012). The daily snowfall (SF) and rainfall (RF) are computed as:

$$SF = P_x\,(T_{rain} - T_x)/(T_{rain} - T_{snow}) \quad (26)$$

$$RF = P_x - SF \quad (27)$$

Where P_x is total precipitation and T_x is the air temperature at gridpoint x. If the daily air temperature is above the T_{rain} threshold then $RF = P_x$ and $SF = 0$, while if $T_x < T_{snow}$ then $RF = 0$ and $SF = P_x$. The two fixed temperature threshold, T_{rain} and T_{snow}, were calibrated on odd years and validated on even years using manual observations of snowfall and rainfall available at the CAF station. A range of -3 to 3°C was selected for calibration based on observed temperatures during recorded precipitations at the CAF station.

2.3. Model validation

The daily snow cover area (SCA) from the merged CMXD10A product (previously described in section '4.3. Processing and combined MOD10A1 and MYD10A1', Chapter II) was used to assess the ability of each model to simulate the spatiotemporal variability of snow cover in the Rheraya basin over the 2013-2016 period. A conversion of the simulated SWE to SCA was required in

order to compare the simulated SCA with MODIS SCA. This conversion was performed using a constant threshold (SWE_0), i.e. for each grid, SCA = 1 when SWE ≥ SWE_0 and SCA = 0 otherwise. The conversion was done at the model resolution (100 m). The use of this fixed threshold avoids more complex snow depletion curves that require more parameters unknown in our area (Magand et al. 2014, Pimentel et al. 2017). Therefore, SWE_0 was subjected to the same calibration/validation procedure as for ΔZ_{max}, using a range of values from 1 to 20 mm following previous studies (Gascoin et al. 2015, Baba et al. 2019)

Confusion matrices were used to assess the classification accuracy of the simulated SCA maps relative to MODIS SCA. Confusion matrices are two-dimensional contingency tables that display the discrete joint distribution of simulated and observed data frequencies (Zappa 2008). Model skill scores were derived from the confusion matrix (Table 13). The Heidke Skill Score (HSS) (Heidke 1926) which is equivalent to the Kappa coefficient proposed by Cohen (1960), measure the classification accuracy relative to that expected by chance and has been extensively used for imbalanced datasets, including snow remote-sensing studies (e.g. Zappa 2008, Notarnicola et al. 2013, Baba et al. 2019). The HSS was thus the preferred global metrics used for model assessment. Still, because no global metric is able to completely depict the types of classification errors committed by a model, four metrics based on marginal ratios of the confusion matrix were also used to investigate model errors, as done in several previous studies (e.g. Parajka and Blöschl 2012, Rittger et al. 2013, Zhou et al. 2013, Zhang et al. 2019). The true positive rate (TPR) measures the proportion of MODIS snow-covered pixels correctly identified as such by the model. Oppositely, the true negative rate (TNR) measures the proportion of MODIS snow-free pixels correctly simulated by the model. The false-negative rate (FNR) measures the proportion of MODIS snow-covered pixels incorrectly identified as snow-free by the model. Complementarily, the false-positive rate (FPR) or 'False Alarm Rate' (FAR) as called by Zappa (2008) is the proportion of MODIS snow-free pixels incorrectly identified as snow-covered by the model. Further descriptions of these metrics are given in (Figure 31).

Table 13: Description of confusion matrix between simulated and MODIS SCA, and the evaluation metrics used for model assessment. TP: true positive, TN: true negative, FP: false positive, FN: false negative.

	SCA MODIS	
SCA_{sim}	**Snow**	**Snow free**
Snow	TP	FP
Snow free	FN	TN
Metrics	**Definitions**	
TPR	$TP/(TP+FN)$	
TNR	$TN/(TN+FP)$	
FNR	$FN/(FN+TP)$	
FPR	$FP/(FP+TN)$	
HSS	$\frac{2\times(TP\times TN-FP\times FN)}{(TP+FP)\times(FP+TN)+(TP+FN)\times(FN+TN)}$	

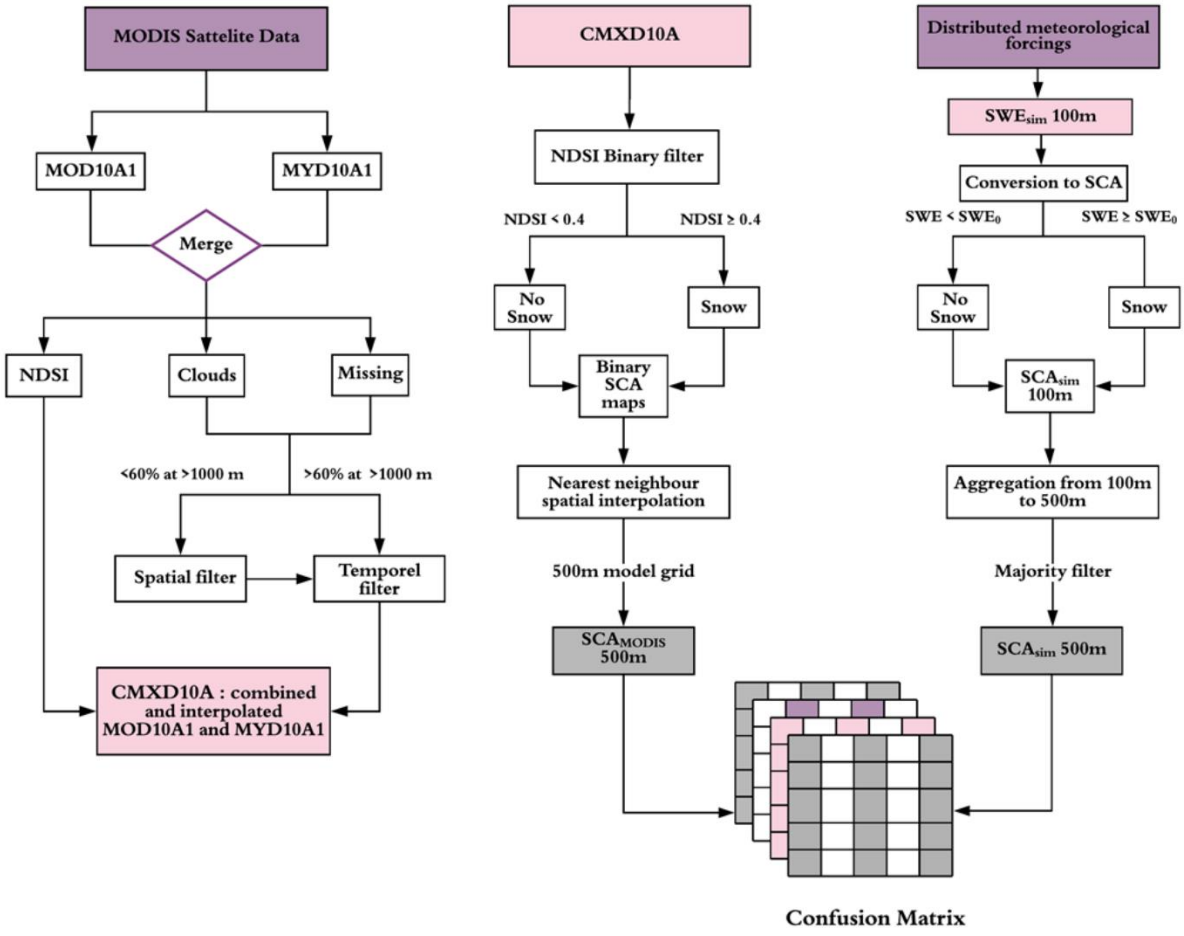

Figure 31: Flowchart describing the steps for processing MODIS data and comparing MODIS and simulated snow cover area (SCA). Purple color: data source, pink: sub-results, and gray: main results.

3. Results

3.1. Point scale model calibration and validation

3.1.1. Rain/snow partition

The optimal values of T_{snow} and T_{rain} thresholds (Equations (26), (27)) found from calibration were -2.5 °C and 2.5 °C respectively. Overall, the agreement between simulated and measured precipitation is fair with a moderate performance for rainfall (NSE = 0.54; r = 0.75), and higher performance for snowfall (NSE= 0.77, r= 0.88) (Figure 32a). The frequency analysis of precipitation events at the CAF station shows that snowfall-only events occurred at air temperatures up to +5°C, while rainfall-only events can occur at temperature down to -5°C, with

mixed events occurring within this -5°C to +5°C range (Figure 32b). The -2.5°C to +2.5°C calibrated range thus stands out as the best compromise to predict most accurately absolute rain and snowfall quantities within this sensitive -5°C to +5°C interval. The better performance for snowfall is encouraging for the ensuing SWE modeling.

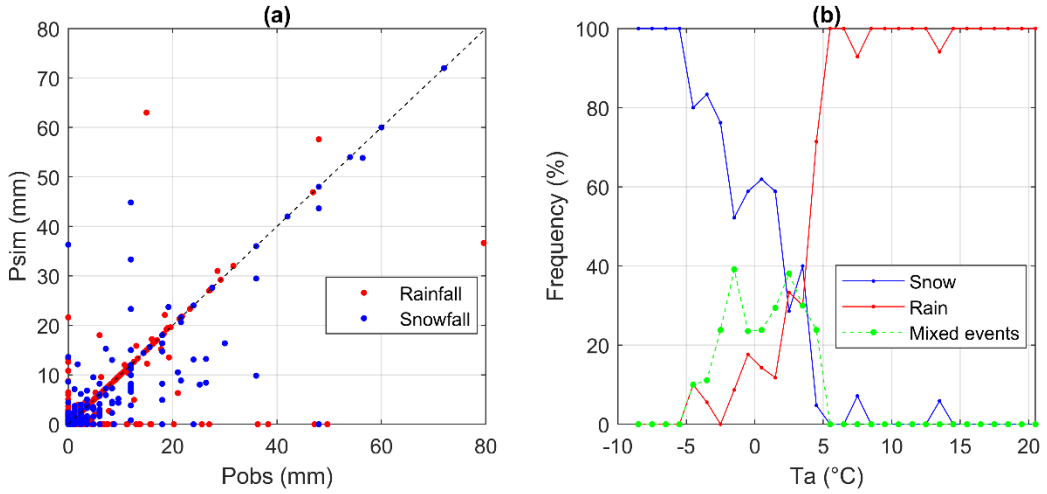

Figure 32: Partition of precipitation into snowfall and rainfall. (a) Simulated vs. observed precipitation after calibration of the fixed rain-snow partition temperature thresholds. (b) Observed frequencies of snow, rain, and mixed precipitation events per one-degree temperature bin at CAF weather station over the 2003-2016 period.

3.1.2. Calibration of PLR

The optimal value for the precipitation lapse rate (PLR) found from calibration against SWE measurements at the Oukaimeden-SM station was 0.35 km^{-1}. The performance among models is relatively similar during the lumped three-year calibration period (2003-2006) (Figure 33). The TI and HTI models show slightly better performances (NSE =0.85) than the models including radiation (ETIA, NSE = 0.78) and albedo (ETIB, NSE = 0.83). All models present the worst prediction performances during the calibration year 2003-2004, during which all models exaggerated ablation from mid-December to mid-February, especially for the ETIB model, while this model performed better than others in late spring (Figure 33a). Independent validation shows different results. In 2006-2007 the models performed unequally, particularly during the ablation period, with models that include radiation (ETIA) and albedo (ETIB) showing an overall better performance (NSE values of 0.60 and 0.78, respectively) than TI (NSE = -0.10) and HTI (NSE = 0.19) (Figure 33). In 2009-2010 all models underestimated accumulation, with slight differences in ablation, and the TI model performed slightly better than other models (NSE = 0.58).

Overall, these results show that the simpler TI and HTI models performed slightly better in calibration than additive ETI models, but they transfer less well to independent validation years. This agrees with previous findings by Bouamri et al. (2018) who showed that enhanced ETI models transfer better to other years when calibrated over a short time period. However, Bouamri et al. (2018) used the observed accumulation rate to calibrate and validate the different melt models, in order to remove the influence of precipitation uncertainties on the calibration of the melt model coefficients (Table 14). The comparatively worst performance observed at the Oukaimeden-SM station in this study can thus be attributed to uncertainties in precipitation observations, rain-snow partition, and the spatial interpolation of precipitation, and highlights the notorious difficulties in distributing precipitations observations in mountainous basins (Gottardi et al. 2012).

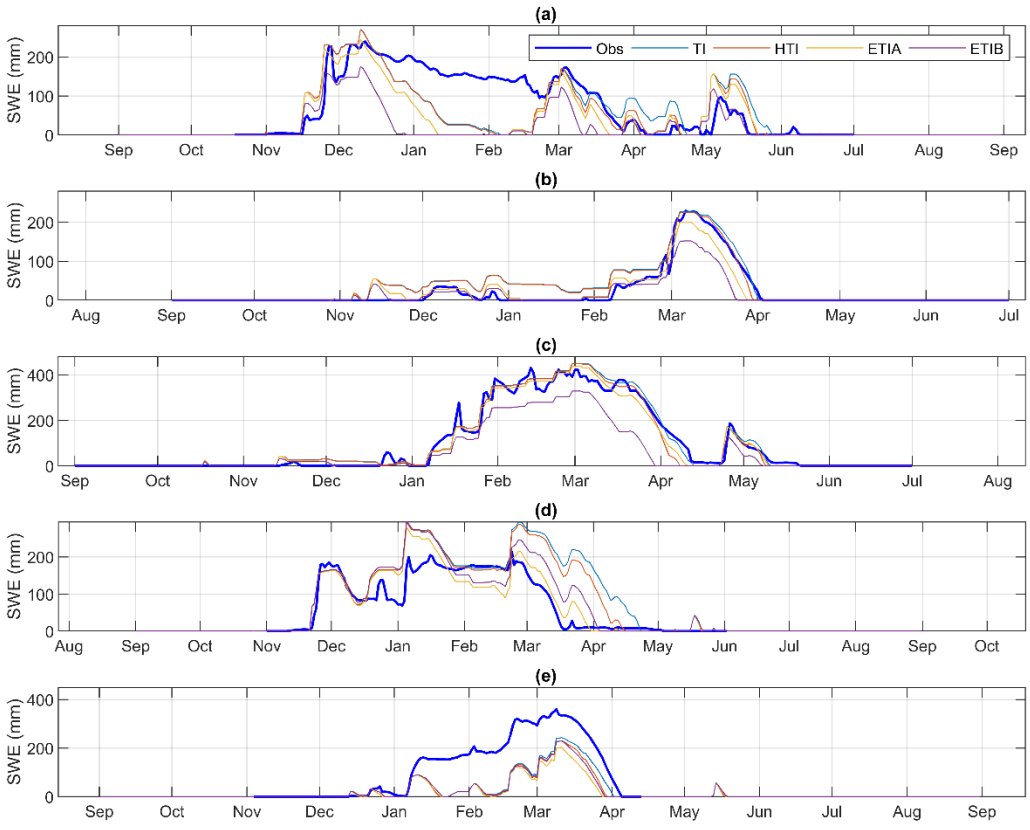

Figure 33: Calibration and validation of precipitation lapse rate (PLR) on observed SWE at AWS Oukaimeden-SM. (a-c) calibrated years, respectively 2003-2004, 2004-2005, 2005-2006; (d-e) validated years, respectively, 2007-2008 and 2009-2010.

Table 14: Summary of model parameters values previously calibrated by Bouamri et al. (2018) and prescribed in this study.

Prescribed parameter	Description	Optimal value	Unit	Calibrated parameter	Description	Optimum value	Unit
DDF	Degree-day factor	2.7	mm d^{-1} °C^{-1}	TLP	Temperature lapse rate	-0.56	°C 100 m^{-1}
MF	Melt factor	1.8	mm d^{-1} °C^{-1}	DPLR	Dew point lapse rate	-0.68	°C 100 m^{-1}
RF	Potential radiation factor	0.005	m^2 mm W^{-1} d^{-1} °C^{-1}	PLR	Precipitation lapse rate	0.35	km^{-1}
TF	Temperature factor	1.1	mm d^{-1} °C^{-1}	SWE_0	SWE-SCA threshold	4	mm
SRF_{in}	Global radiation factor	0.025	m^2 mm W^{-1} d^{-1}	ΔZ_{max}	Maximum elevation difference	1000	m
TF	Temperature factor	0.6	mm d^{-1} °C^{-1}	T_{snow}	Temperature threshold for snow	-2.5	°C
SRF_{net}	Net shortwave radiation factor	0.07	m^2 mm W^{-1} d^{-1}	T_{rain}	Temperature threshold for rain	2.5	°C
p_1	Fresh snow albedo	0.8	-				
p_2	Albedo decay parameter	0.21	-				
Subli	Constant sublimation rate	0.244	mm d^{-1}				

3.2. Catchment-wide snow cover area

3.2.1. Parameter sensitivity and variability

The sensitivity of SCA model performance to the maximum elevation difference (ΔZ_{max}) and SWE-SCA conversion threshold (SWE_0) was assessed using the mean daily HSS metric computed over the calibration period, i.e. the odd years of the 2003-2016 period (Figure 34). Generally, the model performance increases with model complexity, i.e. the HSS is lowest for TI and highest for ETIB. All four models are more sensitive to ΔZ_{max} than the SWE_0 parameter. The mean optimal SWE_0varies between 3 mm for TI to 6 mm for ETIB, with little variations in HSS score within this range as well as within each model. A mean optimal SWE_0 value of 4 mm was thus used for validation on even years and for further inter-model comparisons. This value is small compared to the 40 mm threshold used by Baba et al. (2019) and Gascoin et al. (2015) but SWE_0 is resolution dependent, increasing with pixel resolution. The optimal ΔZ_{max} shows more variability between

models, increasing with model complexity, i.e. lowest for TI and highest for ETIB. This is in fact to be expected from this parameter, which should also partly correct errors in ablation. A mean $\Delta Z_{max}$of 1000m, which is within the zone of maximum performance for each model (Figure 34), was used for validation across models and for further inter-model comparisons.

Table 15 summarizes the calibration and validation metrics using the optimal parameter sets of each model and the mean optimal parameters. Generally, HSS increases slightly with model complexity, where the enhanced ETI (A&B) performs slightly better than the simpler TI and HTI models. Choosing the multi-model average parameter set over the model-specific optimal parameters affects little the performance in validation (Table 15a, b). In fact, some increases in performance are even noted, which suggests that the model-specific values may be slightly overfitted and less transferable compared to the multi-model average parameters. The slight overall differences in performance between models suggest that, on average, all models have similar abilities to classify snow vs. snow-free MODIS pixels, as assessed by the HSS metric. The small differences could be partly attributed to the fact that performance metrics are averaged over the whole calibration period. Hence, inter-annual and seasonal differences in model performance are investigated next.

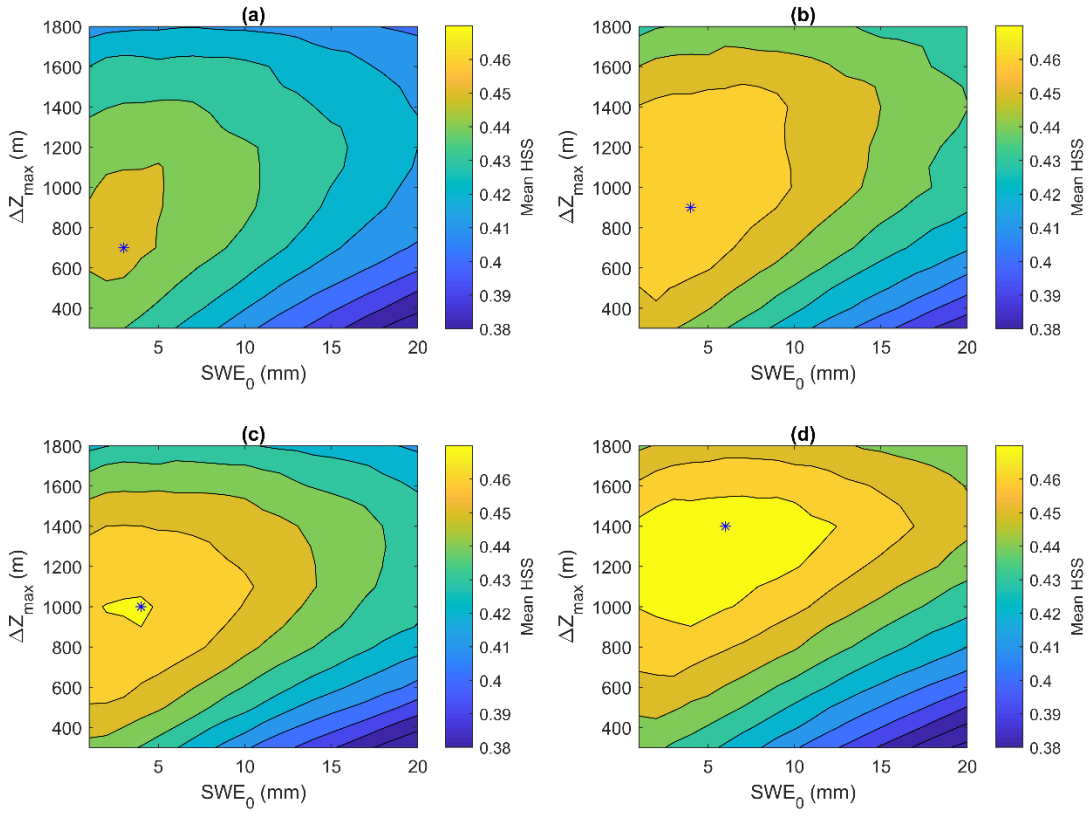

Figure 34: Sensitivity of model SCA simulation performance to ΔZ_{max} and SWE_0 parameters. The model performance is assessed with the mean HSS index over the calibrated period. Optimal parameter values are indicated by asterisks (*). (a) TI; (b) HTI; (c) ETIA; (d) ETIB.

Table 15: HSS index and optimal SWE_0 and ΔZ_{max} parameters obtained in calibration-validation

CALIBRATION				
Models	TI	HTI	ETIA	ETIB
HSS	0.45	0.47	0.47	0.48
VALIDATION				
	A- Optimal parameters sets of each model [SWE_0 (mm), ΔZ_{max}(m)]			
	TI [3, 700]	HTI [4, 900]	ETIA [4, 1000]	ETIB [6, 1400]
HSS	0.46	0.47	0.47	0.47
	B- Mean optimal parameter [$SWE_0 = 4$ mm, ΔZ_{max} = 1000 m]			
HSS	0.45	0.47	0.47	0.48

3.2.2. Basin-wide SWE and SCA

Time series of daily simulated basin-wide SWE and fractional snow cover (fSCA) show significant intra and inter-annual variability over the period (2003-2016) (Figure 35). The fSCA simulated by the four models are in good agreement overall with MODIS observations, both in terms of timing and magnitude. In some years, however, the simulated snow covers lasts longer than observed in MODIS (2004, 2007, 2008, 2009, and 2012). These years had above average basin-wide simulated SWE (Figure 35a), so that overestimated accumulation in the upper basin during these wetter years could be the cause for the longer-lasting simulated SCA. In contrast, in years with scarce snowfall and thinner simulated snowpack (e.g. 2011, 2013, 2014, and 2016), the agreement between simulated and observed fSCA is better.

All four models show slight differences in their basin-wide fSCA and SWE predictions. Error metrics for the whole period (2003-2016) show that increasing model complexity slightly improves the correlation (r) and predictive skill (NSE) for basin-wide fSCA (Figure 35c). Both the root mean squared error (RMSE) and mean absolute error (MAE) also decrease with model complexity, but a larger bias for the ETIB model slightly increases its overall error relative to the ETIA model (Figure 35d). Hence, overall, the best performance is primarily observed for both enhanced radiative models ETIA and ETIB followed by the HTI and the classical TI models. Still, given the slight differences between models and the increased computational cost associated with enhanced radiative models, it is tempting to conclude at this point that the simplest temperature-based TI model offers a satisfactory performance to simulate SWE for hydrological applications in the High Atlas range. The causes for inter-model differences in model performance and in simulated SWE and melt are explored in the next sections.

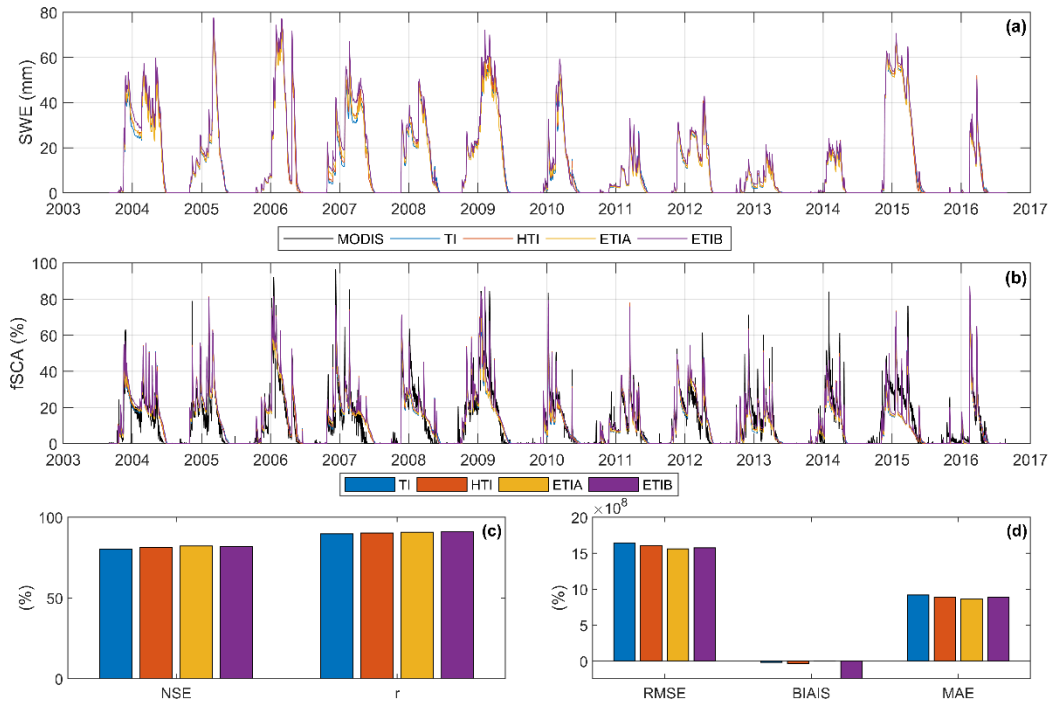

Figure 35: Time series of (a) simulated mean snow water equivalent (SWE), and (b) simulated mean SCA (fractional snow cover area: fSCA) of all models vs MODIS and (c) errors statistics over the entire period 2003-2016 in the Rheraya catchment.

3.2.3. Seasonality

The seasonality of the simulated SWE and fSCA was investigated to better understand seasonal inter-model differences (Figure 36). Models with a radiation term (HTI, ETIA, and ETIB) were contrasted to the classical TI model to highlight the effect of the different radiation terms to the simulated snow cover and model performance relative to MODIS (Figure 36d-f). The mean basin SWE seasonal cycle calculated over snow-covered areas only shows similar variations among models, particularly during the accumulation season (October-March) (Figure 36a). The mean simulated peak occurs in April and varies from 172 mm to 195 mm between models. Increasing differences between the ETI models and TI from March to May indicates increasing ablation rates simulated by these models relative to TI, while the HTI model differs significantly from TI only from May onward (Figure 36d). Maximum differences are reached at peak SWE in April for ETIA (-24 mm) and ETIB (-14 mm) and in June for HTI (-21 mm) (Figure 36d). When considering mean SWE over the whole basin surface, differences between the enhanced models and TI are more positive during winter and occur at different times. ETIB stands out with the largest mean peak

SWE of 37 mm in March, following by HTI and the other models. In contrast to the classical TI, all radiative models simulate higher mean basin SWE in accumulation, while ETIA and HTI simulate lower SWE in late spring compared to TI.

The different seasonal behaviors in the mean basin SWE ('SWE_{basin}') and mean SWE over snow-covered areas ('SWE_{SCA}') can be explained by differences in simulated SCA, since SWE_{basin} = fSCA / 100 × SWE_{SCA}. All models, except ETIB, underestimated MODIS fSCA during accumulation, whereas all models overestimated MODIS fSCA during the ablation period, by 4.2% for ETIB and TI, and by 3.4% for HTI and ETIA (Figure 36c, f). This confirms the tendency identified in Figure 35 for wet years to have a longer-lasting snow cover simulated by all models, relative to MODIS. Inter-model differences show that all enhanced models simulate a larger snow cover than TI during the accumulation period, with ETIB being the most different and also most in line with MODIS, followed by HTI and ETIA. This explains the positive differences in SWE_{basin} between these models and TI during the accumulation period (Figure 36b, e).

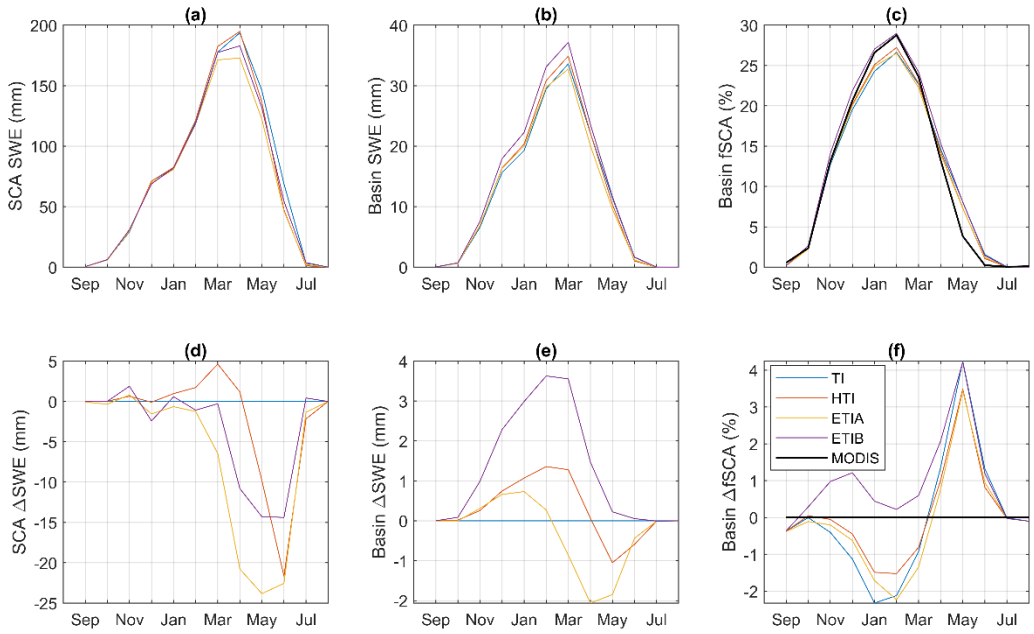

Figure 36: Seasonal cycle of mean simulated snow water equivalent (SWE) (a) over snow-covered area only; (b) over the whole basin; (c) mean simulated fSCA vs MODIS; (d-e) difference between radiative models and reference TI model for a-b panels; (f) difference between modeled and MODIS fSCA.

Seasonal variations in SCA model performance, as measured by the HSS index, were investigated over the calibration, validation, and entire period (Figure 37a-c). Globally, the HSS metric is highest (~0.6-0.75) during winter and spring (December-April) but decreases sharply during the shoulder season (Oct.-Nov. and May-June). This shows that the model performance is generally good during most of the snow season, but that classification errors increase when the snow cover is restricted in the basin. All radiative models performed better than TI especially in the accumulation period, with ETIB performing best, with a maximum increase in HSS of 0.05 in calibration and 0.03 for both the validation and entire period. The models become gradually more similar in late spring (May-June).

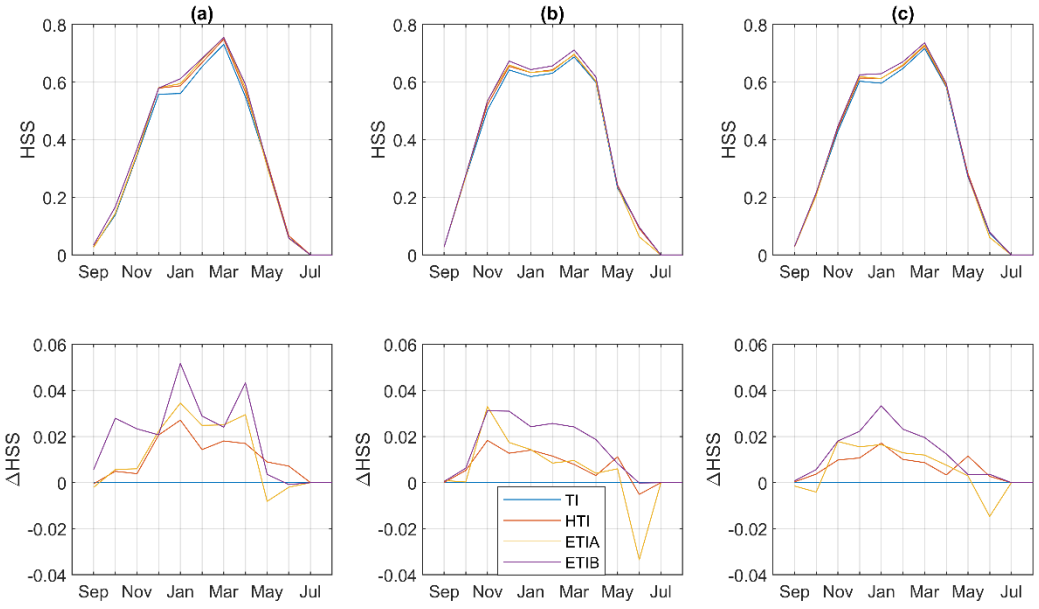

Figure 37: Seasonal cycle of HSS index over (a) calibration; (b) validation; (c) entire period. Lower row: corresponding differences between enhanced radiative models and classical temperature index (TI) model.

3.2.4. Spatial performance

Model performance in predicting spatial variations in SCA was investigated by plotting the HSS metric against elevation bins (Figure 38). Overall, the HSS index increases with elevation for all models (Figure 38b). The mean fractional snow cover area (fSCA) also increases with elevation, in line with MODIS fSCA, but all models start overestimating fSCA above 3500 m (Figure 38a). The lowest HSS values are thus associated with the marginal and transient snow conditions found at the lowest elevations of the basin. Since these elevation areas represent a large share of the basin

hypsometry (Figure 38a), the increased classification errors in these areas have a large influence on the basin-wide and time-averaged performance metrics displayed in Figure 29 and Table 15

All enhanced models perform generally better than TI, although the gains in performance remain overall small (c-e). Elevation trends also differ between the radiative models. ETIB performs best, but the improvement is most pronounced at lower elevations (Z<3000m), which represent a large portion of the total basin but where there is less snow present throughout the year (Figure 38a). At high elevations (Z>3000m) where mean SCA is above 30%, the gain in performance becomes more marginal for ETIB, while it is somewhat more pronounced for HTI and ETIA. While the bulk of the elevation bands show increased performance relative to TI, a small portion of grid points, in some cases up to ~20% (left side of boxes in Figure 38 boxplots), suffered increased errors relative to TI.

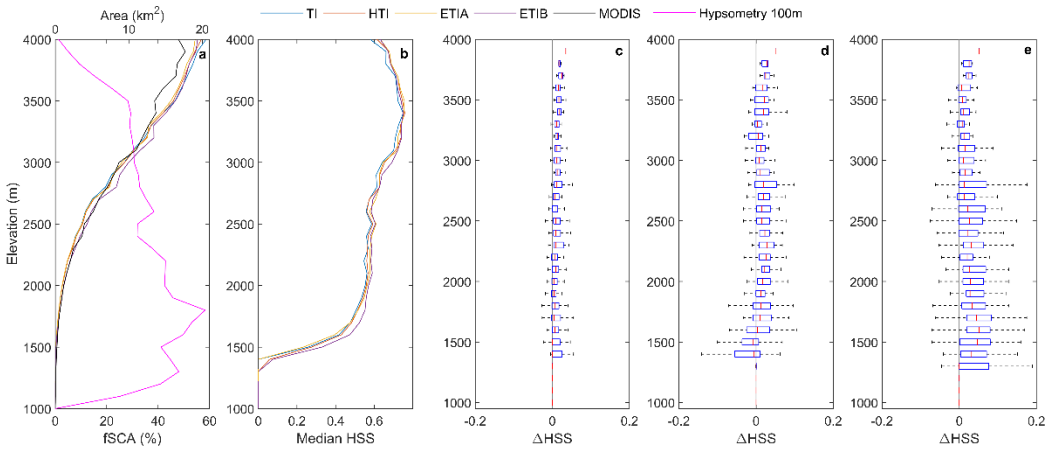

Figure 38: (a) Distribution of mean SCA per elevation range, and hypsometric curve at 100 m. (b) Median of HSS index of all models per elevation, (c, d, and e) HSS differences between radiative and classical model per elevation range over Rheraya basin.

Further insights into the performance behavior between models can be obtained by looking at classification success (TPR, TNR) and error (FPR, FNR) rates by altitude (Figure 39**)**. Overall, TPR increases with elevation, reaching a maximum value of ~0.9 around 3600 m. (Figure 39, row 1**)**. The enhanced models better classify snow presence than TI in the more transient snow zones (~1500-3200m), with ETIB clearly performing best. The improvement for HTI is small but rather consistent with altitude, whereas ETIA shows more variations with even losses in performance in the highest and lowest altitudes relative to TI. Opposite to TPR, the true negative rate (TNR) decreases with altitude. Both ETI models show the largest deviations with TI, but decreased

accuracy is seen at medium elevations, especially for ETIB (Figure 39, row 2). The elevation profile of the FPR error rate shows that all models tend to over predict snow presence towards higher altitudes (Figure 39, rows 3). Conversely, models rarely overpredict snow-free conditions at high elevations, but do so at the lower altitudes (Figure 39, rows 4). Enhanced models can be seen to reduce both the FPR and FNR errors on average, but large scatter occurs within elevation bands. The clearer improvement relative to TI is the decreased FNR error for ETIB (Figure 39 d, rows 4).

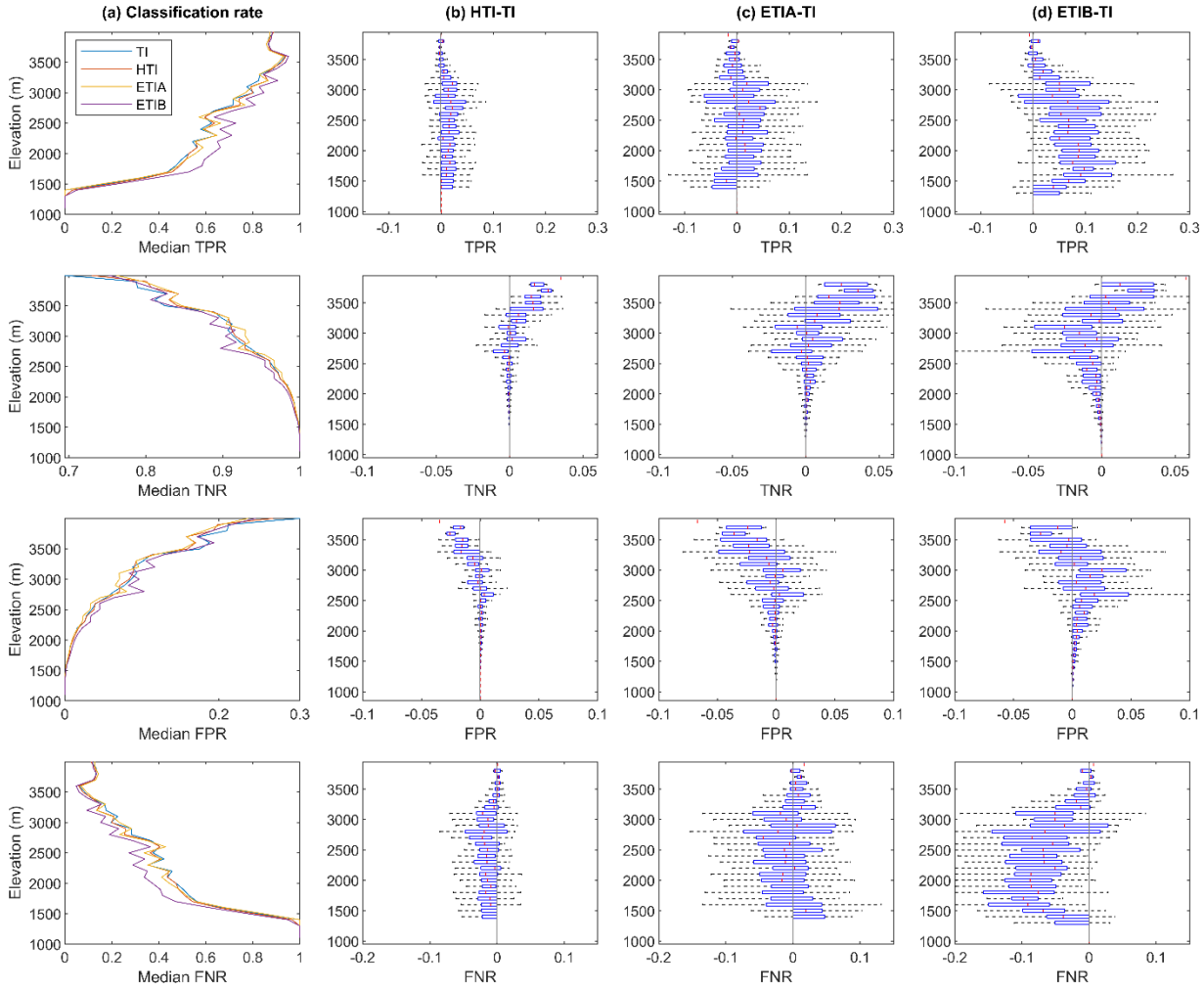

Figure 39: SCA classification errors per elevation range in the Rheraya watershed; 1st row: true positive rate (TPR); 2nd row: true negative rate (TNR); 3rd row: false positive rate (FPR); 4th row: false negative rate. (a) Median error rate; (b, c, and d) differences between radiative and classical TI model.

3.2.5. Snow cover duration (SCD)

The simulated snow cover duration (SCD) was also compared to the observed SCD from MODIS (Figure 40) during calibration (odd years) and validation (even years). The radiative models that include global radiation (ETIA) and albedo (ETIB), slightly outperform (r = 0.96, RMSE = 17 days) the HTI and TI models (r = 0.95, RMSE = 18-19 days) in validation. Overall ETIB performed best, with the lowest RMSE in calibration and in validation (equal to ETIA) and lower bias in validation. However, differences between models do no stand out clearly for SCD, despite significant spatial differences in SCA predictions and errors between models (Figure 38, Figure 39).

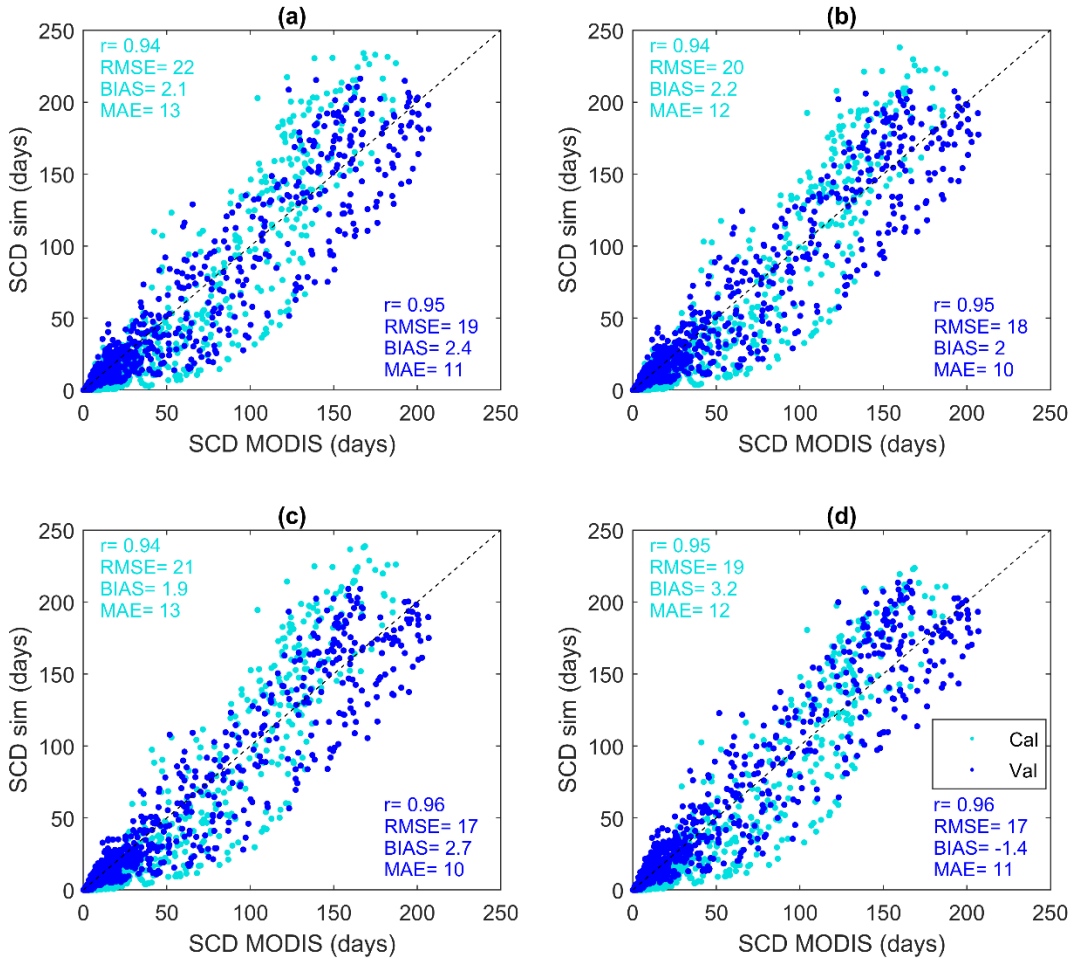

Figure 40: Annual average simulated snow cover duration (SCD) vs MODIS SCD during calibration (light blue) and validation (dark blue), with statistic errors for all model (a) TI; (b) HTI; (c) ETIA; (d) ETIB.

4. Discussion and conclusion

4.1. Difference in model performance

The enhanced radiative models, especially ETIB, showed increased performance relative to the simplest TI model for predicting basin wide SCA over time (Figure 35). In particular, the peak SCA in February was notably better simulated by the ETIB model compared to the other models (Figure 36c). However, overall differences in model performance were small. More contrasts between models were found in their ability to simulate the spatial heterogeneity of the snow cover. While all radiative models improved SCA predictions, the ETIB model showed the most improvement, with the largest gains in performance at mid to low elevations (Figure 38). The increasing FPR and decreasing FNR with elevations suggest that there may be a persistent elevation bias in the simulated SCA (Figure 39), which is partly alleviated by radiative models, in particular ETIB. This suggests that increasing global radiation with altitude (due to higher atmospheric transmissivity) and the consideration of snow albedo result in steeper ablation elevation profiles relative to temperature-only melt calculations with the TI model. However, the remaining elevation trends in the error rates point to lingering problems with the distribution of precipitation in the basin.

The distribution of precipitation in mountainous areas is challenging (Gottardi et al. 2012, Grünewald et al. 2014, Nepal et al. 2014), especially in a data-scarce region such as the High Atlas Range. The exclusion of two high elevation stations with unreliable unheated tipping bucket gauges left us to rely heavily on the CAF station to extrapolate precipitations to higher elevations. While reliable, this station is located near the basin boundary and its elevation (2612 m) is low compared to the considerable amount of snow-covered terrain higher up (Figure 38a). Furthermore, the precipitation lapse rate calculated using the available stations up to 2612 m was found to be poorly defined due to the large spatial and temporal heterogeneity of observed precipitation, which prompted the decision to use a single and constant non-linear lapse rate calibrated on positive SWE changes at the Oukaimeden station (3230 m). The use of a calibrated maximum difference elevation (ΔZ_{max}) to limit the vertical extrapolation of precipitation may have limited the errors associated with this approach, but better spatially-distributed precipitation fields would be needed in the future to improve snow simulations for hydrological model applications. Outputs from numerical weather models are increasingly used for this purpose, but

are still problematic for precipitation (Bellaire et al. 2011, Réveillet et al. 2020). Scaling precipitation inputs by measured snow distributions is another promising approach but requires costly airborne surveys to acquire reliable snow depth maps (Vögeli et al. 2016). Progresses in mapping snow depth from high-resolution stereoscopic satellite images could however open new avenues on this front (Marti et al. 2016). Assimilation of snow cover maps within snow models can also help reducing precipitations biases, but increases computation costs (Margulis et al. 2016, Baba et al. 2018).

Our results show that most of the snow cover variability is driven by elevation and that this trend was adequately captured by all four models (Figure 38). Hence the simple TI model could be sufficient for melt simulations at the basin scale, due to the strong dependence of temperature and related melt rates on elevation, as found elsewhere (e.g. Vincent 2002, Hock 2003, Réveillet et al. 2017). The enhanced radiative models improved the snow cover simulations, but given their significant extra computational cost, our results suggest that the simpler TI is adequate for operational snow simulations in the high Atlas Range. This contrasts previous studies that showed that including solar radiation improves the performance of spatially-distributed melt models for predictions of glacier mass balance (Gabbi et al. 2014), snow cover area (Follum et al. 2015), and streamflow from snow-fed basins (Brubaker et al. 1996, Follum et al. 2019). On the other hand, the use of a fully distributed (grid-based) model improved the simulations of SCA relative to semi-distributed temperature index models previously applied in this basin (Boudhar et al. 2009).

Despite the overall good performance for the simple TI model, enhanced models still explained more variability in SCA per elevation band, but with notable discrepancies among models (Figure 38). To better understand these discrepancies, the simulated SWE and melt rates were compared by elevation band (Figure 41). The HTI model shows the smallest difference relative to TI, in line with its more similar performance in SCA simulations. This can be attributed to the fact that HTI only considers the potential clear-sky radiation and thus ignores temporal variations in atmospheric transmissivity and albedo. Both ETI models show significant differences in simulated SWE (c, d) and melt rates (Figure 41g, h) relative to TI. The best performing ETIB model simulates smaller melt rates and larger SWE at middle elevations (2000-3500 m), and higher melt rates and smaller SWE at the highest elevations (>3500 m). Interestingly, median differences in SWE and melt rates per elevation band are rather small, which again shows that the preponderant influence of elevation on the simulated SWE is well captured by the simple TI model. However, significant deviations

occur, up to ca. ±20 mm for SWE and ca. ±1 mm d^{-1} for melt rates (Figure 41c-d, g-h). Even more interesting is the fact that these significant differences in melt rates and SWE do not result in larger inter-model differences in SCA simulations. On the one hand, this shows the general limitation of using satellite SCA to validate and compare model performance for SWE simulations. On the other hand, it also points to possible adverse effect of using coarse resolution products such as MODIS for validation of higher-resolution models. This topic is discussed in detail next.

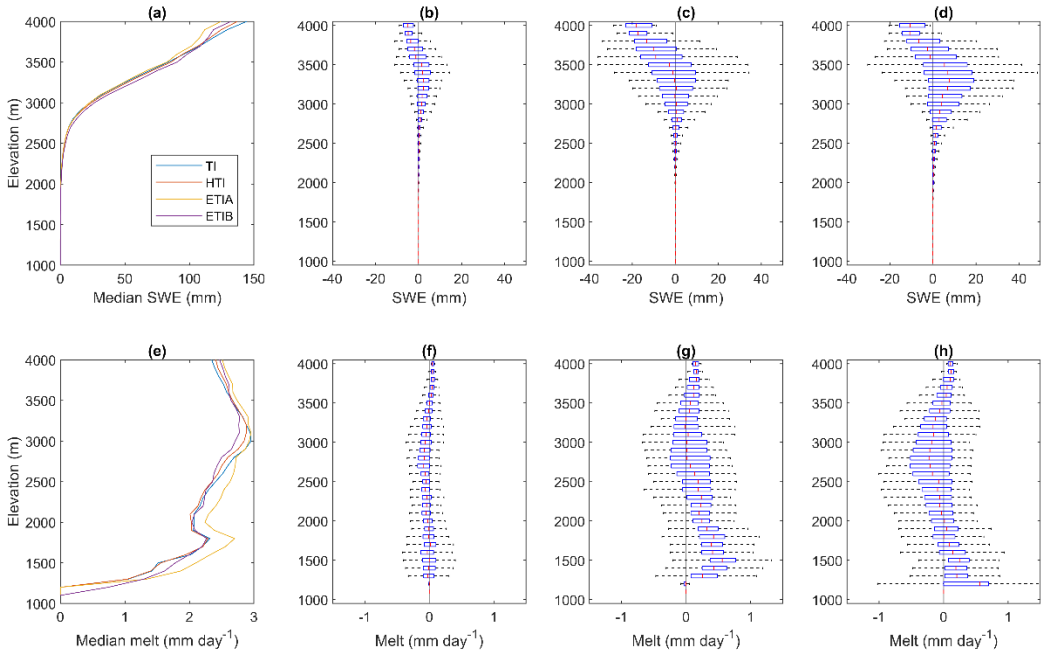

Figure 41: SWE and melt per elevation band in the Rheraya catchment. (a) Median SWE for all models; (b-d) SWE differences between radiative and classical TI model; (e) median melt rate for all models; (f-h) melt differences between radiative and TI model

4.2. Effect of spatial resolution on SCA validation

In order to compare the simulated SCA with MODIS, the modeled SCA was aggregated from 100 m to the 500 m resolution of MODIS (Figure 31). This has the potential to suppress significant spatial variability in the finer (100 m) scale simulated SCA. To explore this, the snow cover duration (SCD, equal to mean SCA × 365 days) modeled at the original 100 m resolution was compared to that aggregated at 500 m resolution (Figure 42). While the overall elevation trends remain unchanged, the aggregation of SCA from 100 m to 500 m results in significant changes in SCA at some elevations, especially for the ETI models (Figure 42c-d vs. g-h). The simulated median SCD elevation profiles at 500 m resolution are not as smooth as the original ones at 100

m (Figure 42a vs. e). This is explained by the considerable smoothing of SCA variability related to slope and aspect variations at scales finer than 500 m, as seen by the considerable noise in the median northern exposure index profile for the 500 m aggregated vs. original 100 m DEM (Figure 42a vs. e). This loss, upon aggregation, of topographic-induced SCA variability simulated by the radiative models can partly explain why the SCD simulated at 500 m by the different models give overall similar results compared to MODIS (Figure 40, Figure 42i-l).

The smoothing effect of model aggregation is particularly evident when plotting modeled quantities (SWE, melt rates, and SCD) by aspect (Figure 43). At the original 100 m model resolution, all radiative models expectedly simulate smaller melt rates and larger SWE on northern slopes, and vice-versa on southern slopes (Figure 43a, b), which results in longer-lasting snow on northern slopes compared to TI (Figure 43c). This is in line with previous studies (e.g. López-Moreno and Stähli 2008, Comola et al. 2015, Baba et al. 2019) which found that south-facing slopes receive more solar radiation and generally melts faster than on north-facing slopes. Aggregation of simulated SCA to 500 m results in significant disruption of this pattern (Figure 43d), which can be attributed to changes in the distribution of slopes and aspects following aggregation (Figure 43e). These results corroborate previous conclusions made by Baba et al. (2019) concerning the influence of DEM resolution on the simulation of snow cover. Using the physically-based model SnowModel (Liston and Elder 2006), they found a significant degradation of model performance when aggregating the model DEM to resolutions of 500 m and beyond, which disrupted the representation of slopes in the basin and affected solar radiation variability.

Our results can be put in the context of the findings by Comola et al. (2015), who showed that the effects of solar radiation patterns on the hydrologic response of snow-covered basins are scale dependent, i.e., significant at small scales with predominant aspects and weak at larger scales where aspects become uncorrelated and orientation differences average out. These authors further found that a calibrated TI model on scales larger than the aspect correlation scale are well transferable. Their conclusions find support in our results:

(i) The inclusion of radiation patterns in the large Rheraya catchment has a small influence overall on basin-wide simulated average SWE and SCA compared to the reference TI model.

(ii) The influence of solar radiation on simulated SWE and melt rates is greatly suppressed when aggregating model outputs to MODIS resolution of 500 m, which smooths out radiation effects and brings the radiative models closer to simulations made with a simple temperature-based (TI) model.

Hence, our results support the notion that in large basins (i.e. larger than the correlation length of the terrain), topographic-induced variations in solar radiation tend to average out so that mean simulated melt rates, SWE and SCA do not differ greatly from using temperature alone to predict snowmelt. A more uniform distribution of slope aspects in a basin, such as observed here for Rheraya (cf. Figure 43), will reinforce this phenomenon. In the context of operational flow forecasting in the High Atlas Range, simple temperature index models could thus provide sufficiently accurate snowmelt estimates.

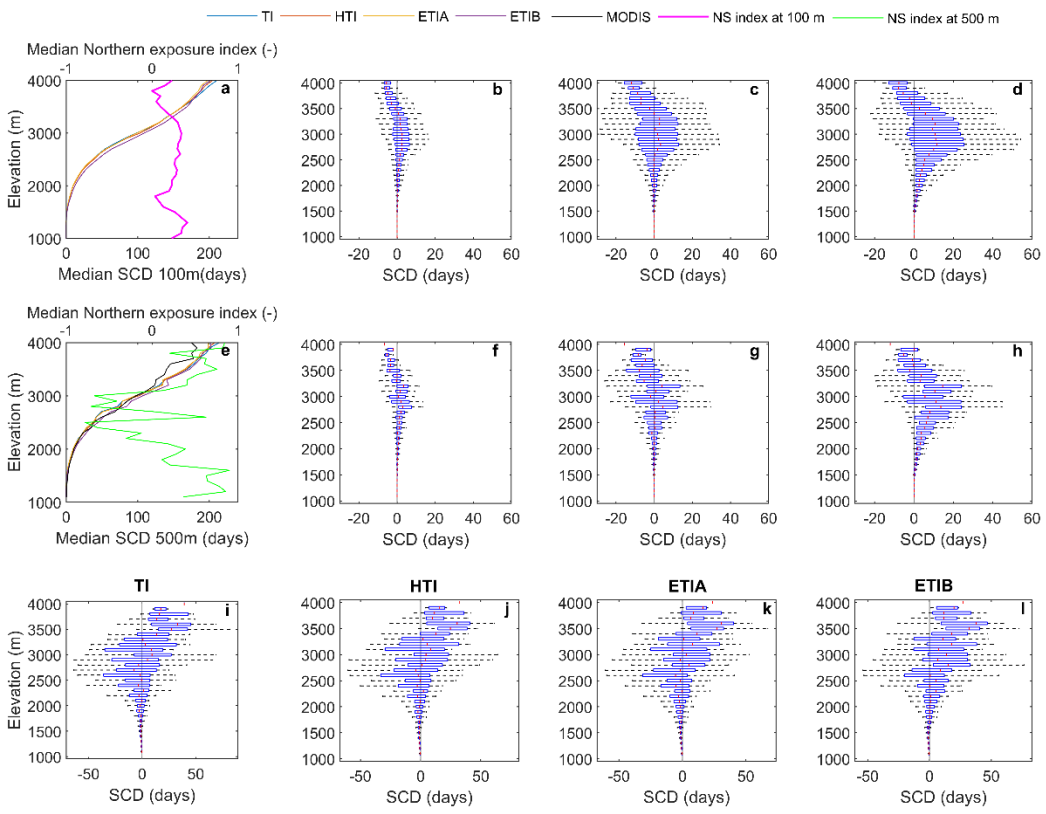

Figure 42: Snow cover duration (SCD) per elevation band in the Rheraya catchment. (a) Median SCD and DEM median northern exposure index at 100 m resolution; (b, c, and d) SCD differences between radiative and classical model at 100 m. (e-h): same as (a-b) but SCD is aggregated from 100 m to 500 m and the northern exposure index ('NS index') is calculated on a DEM aggregated from 100 m to 500 m. (i-l) Differences between each model 500 m SCA and MODIS.

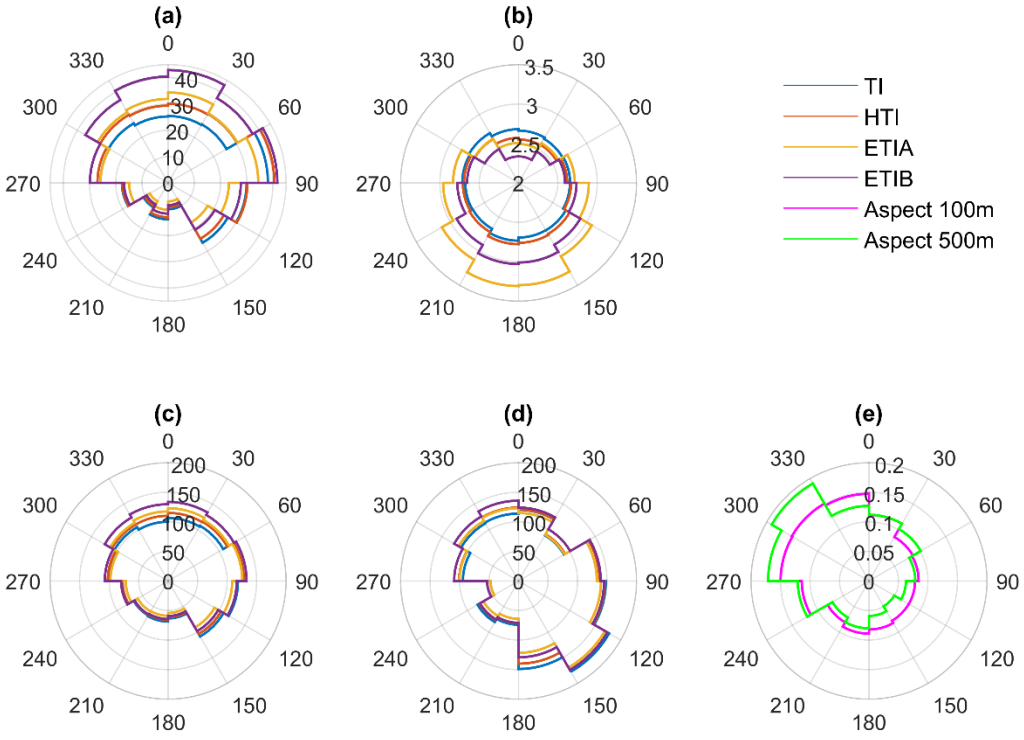

Figure 43: Mean SWE, melt rate, and snow cover duration (SCD) by aspect. (a) Mean SWE (mm); (b) melt rate (mm d^{-1}); (c) SCD (days) at 100 m resolution; (d) SCD (days) at 500 m resolution and (e) DEM aspect at 100 and 500 m resolution.

CONCLUSIONS AND PERSPECTIVES

1. Conclusions

This research highlighted the importance of understanding and quantifying snow contribution to catchment hydrology in the Moroccan High Atlas Mountains. There is therefore a need to better estimate snowmelt component contribution to runoff. In this context, modeling snowmelt and snow water equivalent (SWE) provides important and useful guidance for water managers and decisions maker in these mountainous areas, especially in a limited data availability context.

In this sense, four empirical snowmelt models were tested and compared to simulate snowmelt and snow water equivalent (SWE) at both scales: (i) local at 'Oukaimeden-SM' station and (ii) spatial at 'Rheraya' basin in High Atlas Mountain. These empirical models used for snowmelt provides simplified process representations with lower data requirements. They are tested grow in complexity and physical realism from the simple, one-parameter TI model to the two-parameter ETI models while conserving a parsimonious data requirement, which is crucial for applications in the High Atlas.

The model performance was tested first at local scale by simulating snowmelt and snow water equivalent (SWE) at Oukaimeden-SM AWS. Due to the lack of long-term meteorological data, especially shortwave radiation and albedo, simple parameterizations were developed to represent these variables in the snowmelt models. The four models were subjected to different cross calibration-validation methods over the 2003–2010 period, and the parameter sensitivity and model transferability over time were assessed. The main results suggest: (i) when calibrated on a yearly basis, all models performed well (NSE > 0.93) in calibration mode, but the enhanced additive models performed better in validation mode (NSE = 0.68–0.74) than the TI and HTI models (NSE = 0.56) and were thus deemed to be better transferable over time. (ii) The leave-one-year-out cross-validation procedure showed that models are more transferable when calibrated on a longer period that includes some inter-annual climate variability; all models performed well in validation mode (NSE = 0.78–0.82), with the ETI-B model (NSE = 0.82) only slightly outperforming the simpler TI model (NSE = 0.81). Hence, temporal variations in snowmelt could be adequately reproduced when sufficiently long periods are available for calibration of the TI

model. (iii) Notable annual variations were found in yearly-calibrated model parameters and only marginal connections emerged between yearly-calibrated parameters and climate conditions. While the short period (5 years) inherently precludes a more conclusive analysis, it is suggested that the collinearity of air temperature and solar radiation are responsible for much of this variability; fitting collinear variables on observations affected by measurement uncertainties will cause large variations in calibrated parameters. This collinearity causes parameters to compensate each other and gives rise to equifinality between the temperature and radiation-based factors. This same equifinality may explain why different yearly-calibrated parameter combinations yield acceptable performance when transferred to other years. Despite the highlighted equifinality phenomenon, the ETI-B model stands out as the best model overall. While its performance was only marginally superior to the simple TI model when calibrated on multiyear intervals, it performed better than other models when calibrated on short (1-year) intervals.

At basin scale, a benchmark of the performance of enhanced models (ETI) including different treatments of solar radiation, relative to the reference temperature-index (TI) model to simulate spatially-distributed snowmelt, snow water equivalent (SWE), and snow cover area (SCA) within the Rheraya basin. A spatial distribution of forcing in-situ data used at local scale was done over Rheraya through an optimal spatialization methods (coupling Barnes objective scheme with lapse rate); the merge of both MODIS SCA products (Terra and Aqua) for model validation and, (e) the sensibility analysis of SWE-SCA conversion threshold. The main results show: (i) most of the snow cover variability is driven by elevation and that this trend was adequately captured by all four models. Hence the simple TI model could be sufficient for melt simulations at the basin scale, due to the strong dependence of temperature and related melt rates on elevation. The enhanced radiative models (ETI) improved the snow cover simulations, but given their significant extra computational cost, our results suggest that the simpler TI is adequate for operational snow simulations in the high Atlas Range. (ii) The inclusion of radiation patterns in the large Rheraya catchment has a small influence overall on basin-wide simulated average SWE and SCA. (iii) The influence of solar radiation on simulated SWE and melt rates is greatly suppressed when aggregating model outputs to MODIS resolution of 500 m, which smooths out radiation effects and brings the radiative models closer to simulations made with a simple temperature-based (TI) model. Our results support also the notion that in large basins (i.e. larger than the correlation length of the terrain), topographic-induced variations in solar radiation tend to average out so that mean

simulated melt rates, SWE and SCA do not differ greatly from using temperature alone to predict snowmelt. A more uniform distribution of slope aspects in a basin, such as observed here for Rheraya, will reinforce this phenomenon. In the context of operational flow forecasting in the High Atlas Range, simple temperature index models will thus provide sufficiently accurate snowmelt estimates.

This thesis underlined the importance of the available, longer, and higher quality data series at remote sites. In addition, it emphasizes the importance of the calibration period as a key in model parameters transferability over time. On the other hand, this dissertation outline that the simple TI model would be sufficient and adequate for operational snowmelt simulations at both local and spatial scale in High Atlas. Regarding remote sensing data, our findings call for caution when using medium resolution satellite products such as MODIS to validate spatially distributed snow models. The necessary aggregation of finer-scale model outputs to a resolution larger than key processes scales, such as that where interactions between topography and solar radiation are greatest, will suppress valid model information. According to our results, we suggest, in future studies, the use of other satellite data with higher resolution such as Landsat images which can provide more detailed snow observations to present more comprehensive evaluation and validation of the physical process of snow such as melt and SWE.

2. Perspectives

Some elements were not addressed in the framework of this Ph.D. thesis and several research perspectives can be proposed. The perspectives encompass the following aspects:

1. Due to the lack of in-situ data, particularly precipitation, the observed snow accumulation was derived from a previously estimated SWE, to force the models instead of measured precipitation, which introduces uncertainties to the snowmelt models. Therefore, there is a need to reinforce the network station in High Atlas Range, to better monitor, examine and ensure observation records, to avoid unreliable records and for better use in the outcoming projects.
2. Further investigation on the impact of the collinearity and transferability of melt model parameters is warranted, hopefully at sites with longer and higher quality data series.

3. The enhanced temperature index model that includes albedo (ETIB) was performed with parametrized albedo in this study. However, MODIS albedo was also investigated and tested, but not included. This is partly because, the snow albedo obtained from MCD43A3 product was found to exhibit low values, with a maximum of only 0.7 in winter over the entire Rheraya area. Considering the high albedo of fresh snow, between 0.75 and 0.98, this underestimation could be attributed to the contamination of land surfaces within mixed snow and land pixel. Further investigation of the unmixing issue is therefore required to incorporate MODIS Albedo into the ETI model.
4. The increasing availability of publicly available high-resolution snow cover maps imagery should progressively reduce our dependence on MODIS snow cover products and help crash-testing high-resolution snow models in the future.
5. The impact of including solar radiation patterns in snowmelt calculation on streamflow simulations should be investigated in a future study.

REFERENCES

Abermann, J., C. Kinnard and S. MacDonell (2014). "Albedo variations and the impact of clouds on glaciers in the Chilean semi-arid Andes." Journal of Glaciology 60(219): 183-191.

Abudu, S., C.-l. Cui, M. Saydi and J. P. King (2012). "Application of snowmelt runoff model (SRM) in mountainous watersheds: A review." Water Science and Engineering 5: 123-136.

Alpert, P. (1986). "Mesoscale indexing of the distribution of orographic precipitation over high mountains." Journal of climate and applied meteorology 25(4): 532-545.

Amri, R., M. Zribi, Z. Lili-Chabaane, B. Duchemin, C. Gruhier and A. Chehbouni (2011). "Analysis of Vegetation Behavior in a North African Semi-Arid Region, Using SPOT-VEGETATION NDVI Data." Remote Sensing 3(12): 2568-2590.

Anderton, S. P., S. M. White and B. Alvera (2004). "Evaluation of spatial variability in snow water equivalent for a high mountain catchment." Hydrological Processes 18(3): 435-453.

Arsenault, R., F. Brissette and J.-L. Martel (2018). "The hazards of split-sample validation in hydrological model calibration." Journal of hydrology 2018 v.566: pp. 346-362.

Baba, M. W., S. Gascoin, L. Jarlan, V. Simonneaux and L. Hanich (2018). "Variations of the Snow Water Equivalent in the Ourika Catchment (Morocco) over 2000–2018 Using Downscaled MERRA-2 Data." Water 10(9): 1120.

Baba, M. W., S. Gascoin, C. Kinnard, A. Marchane and L. Hanich (2019). "Effect of Digital Elevation Model Resolution on the Simulation of the Snow Cover Evolution in the High Atlas." Water Resources Research 55(7): 5360-5378.

Bacchi, B. and N. T. Kottegoda (1995). "Identification and calibration of spatial correlation patterns of rainfall." Journal of Hydrology 165(1-4): 311-348.

Barnes, S. L. (1964). "A technique for maximizing details in numerical weather map analysis." Journal of Applied Meteorology 3(4): 396-409.

Barnett, T. P., J. C. Adam and D. P. Lettenmaier (2005). "Potential impacts of a warming climate on water availability in snow-dominated regions." Nature 438(7066): 303-309.

Barnett, T. P., J. C. Adam and D. P. Lettenmaier (2005). "Potential impacts of a warming climate on water availability in snow-dominated regions." Nature 438: 303-309.

Bellaire, S., J. B. Jamieson and C. Fierz (2011). "Forcing the snow-cover model SNOWPACK with forecasted weather data." The Cryosphere 5(4): 1115-1125.

Bergström, S. (1976). Development and application of a conceptual runoff model for Scandinavian catchments.

Beven, K. (1993). "Prophecy , reality and uncertainty in distributed hydrological modeling." Advances in Water Resources 16: 41-51.

Beven, K. (2006). "A manifesto for the equifinality thesis." Journal of Hydrology 320: 18–36.

Bouamri, H., A. Boudhar, S. Gascoin and C. Kinnard (2018). "Performance of temperature and radiation index models for point-scale snow water equivalent (SWE) simulations in the Moroccan High Atlas Mountains." Hydrological Sciences Journal 63(12): 1844-1862.

Boudhar, L. Hanich, G. Boulet, B. Duchemin, B. Berjamy and A. Chehbouni (2009). "Evaluation of the Snowmelt Runoff Model in the Moroccan High Atlas Mountains using two snow-cover estimates." Hydrological Sciences Journal 54: 1094-1113.

Boudhar, A. (2009). Télédétection du manteau neigeux et modélisation de la contribution des eaux de fonte des neiges aux débits des Oueds du Haut Atlas de Marrakech. PhD, University Cadi Ayyad.

Boudhar, A., G. Boulet, L. Hanich, J. E. Sicart and A. Chehbouni (2016). "Energy fluxes and melt rate of a seasonal snow cover in the Moroccan High Atlas." Hydrological Sciences Journal 61: 931-943.

Boudhar, A., B. Duchemin, L. Hanich, G. Boulet and A. Chehbouni (2011). "Spatial distribution of the air temperature in mountainous areas using satellite thermal infra-red data." Comptes Rendus Geoscience 343(1): 32-42.

Boudhar, A., B. Duchemin, L. Hanich, L. Jarlan, A. Chaponnière, P. Maisongrande, G. Boulet and A. Chehbouni (2010). "Long-term analysis of snow-covered area in the Moroccan High-Atlas through remote sensing." International Journal of Applied Earth Observation and Geoinformation 12: S109-S115.

Boudhar, A., L. Hanich, G. Boulet, B. Duchemin, B. Berjamy and A. Chehbouni (2009). "Evaluation of the Snowmelt Runoff Model in the Moroccan High Atlas Mountains using two snow-cover estimates." Hydrological Sciences Journal 54: 1094-1113.

Boudhar, A., H. Ouatiki, H. Bouamri, Y. Lebrini, I. Karaoui, M. Hssaisoune, A. Arioua and T. Benabdelouahab (2020). Hydrological Response to Snow Cover Changes Using Remote Sensing over the Oum Er Rbia Upstream Basin, Morocco. Mapping and Spatial Analysis of Socio-economic and Environmental Indicators for Sustainable Development, Springer**:** 95-102.

Brock, B. W., I. C. Willis and M. J. Sharp (2000). "Measurement and parameterization of albedo variations at Haut Glacier d ' Arolla , Switzerland." Journal of Glaciology 46: 675-688.

Brubaker, K., A. Rango and W. Kustas (1996). "Incorporating radiation inputs into the snowmelt runoff model." Hydrological Processes 10: 1329-1343.

Buck, A. L. (1981). "New equations for computing vapor pressure and enhancement factor." Journal of applied meteorology 20(12): 1527-1532.

Carenzo, M., F. Pellicciotti, S. Rimkus and P. Burlando (2009). "Assessing the transferability and robustness of an enhanced temperature-index glacier-melt model." Journal of Glaciology 55(190): 258-274.

Cazorzi, F. and G. Dalla Fontana (1996). "Snowmelt modelling by combining air temperature and a distributed radiation index." Journal of Hydrology 181(1-4): 169-187.

Chaponnière, A., P. Maisongrande, B. Duchemin, L. Hanich, G. Boulet, R. Escadafal and S. Elouaddat (2005). "A combined high and low spatial resolution approach for mapping snow covered areas in the Atlas mountains." International Journal of Remote Sensing 26(13): 2755-2777.

Chehbouni, A., R. Escadafal, B. Duchemin, G. Boulet, V. Simonneaux, G. Dedieu, B. Mougenot, S. Khabba, H. Kharrou, P. Maisongrande, O. Merlin, A. Chaponnière, J. Ezzahar, S. Er-Raki, J. Hoedjes, R. Hadria, A. Abourida, A. Cheggour, F. Raibi, A. Boudhar, I. Benhadj, L. Hanich, A. Benkaddour, N. Guemouria, a. H. Chehbouni, A. Lahrouni, A. Olioso, F. Jacob, D. G. Williams and J. a. Sobrino (2008). "An integrated modelling and remote sensing approach for hydrological study in arid and semi-arid regions: the SUDMED Programme." International Journal of Remote Sensing 29: 5161-5181.

Clark, M. P., J. Hendrikx, A. G. Slater, D. Kavetski, B. Anderson, N. J. Cullen, T. Kerr, E. Örn Hreinsson and R. A. Woods (2011). "Representing spatial variability of snow water equivalent in hydrologic and land-surface models: A review." Water Resources Research 47(7).

Cohen, J. (1960). "A coefficient of agreement for nominal scales." Educational and psychological measurement 20(1): 37-46.

Collados-Lara, A. J., E. Pardo-Igúzquiza, D. Pulido-Velazquez and J. Jiménez-Sánchez (2018). "Precipitation fields in an alpine Mediterranean catchment: Inversion of precipitation gradient with elevation or undercatch of snowfall?" International Journal of Climatology 38(9): 3565-3578.

Comola, F., B. Schaefli, P. D. Ronco, G. Botter, M. Bavay, A. Rinaldo and M. Lehning (2015). "Scale-dependent effects of solar radiation patterns on the snow-dominated hydrologic response." Geophysical Research Letters 42(10): 3895-3902.

Coron, L., Andre, V. Andreassian, C. Perrin, J. Lerat, J. Vaze, M. Bourqui and F. Hendrickx (2012). "Crash testing hydrological models in contrasted climate conditions: An experiment on 216 Australian catchments." Water resources research 48: 1-17.

Cudennec, C., C. Leduc and D. Koutsoyiannis (2007). "Dryland hydrology in Mediterranean regions — a review." Hydrological Sciences 52: 1077-1087.

Dai, A., K. E.Trenberth and T. R.Karl (1999). "Effects of clouds , soil moisture , precipitation , and water vapor on diurnal temperature range." Journal of Climate 12: 2451-2473.

Daly, C., W. P. Gibson, G. H. Taylor, G. L. Johnson and P. Pasteris (2002). "A knowledge-based approach to the statistical mapping of climate." Climate research 22(2): 99-113.

Daly, C., R. P. Neilson and D. L. Phillips (1994). "A statistical-topographic model for mapping climatological precipitation over mountainous terrain." Journal of applied meteorology 33(2): 140-158.

De Jong, C., S. Cappy, M. Finckh and D. Funk (2008). "A transdisciplinary analysis of water problems in the mountainous karst areas of Morocco." Engineering Geology 99: 228-238.

De Jong, C., D. Lawler and R. Essery (2009). "Mountain hydroclimatology and snow seasonality - Perspectives on climate impacts, snow seasonality and hydrological change in mountain environments." Hydrological Processes 23: 955-961.

DeBeer, C. M. and J. W. Pomeroy (2009). "Modelling snow melt and snowcover depletion in a small alpine cirque, Canadian Rocky Mountains." Hydrological Processes 23(18): 2584-2599.

DeWalle, D. and A. Rango (2008). "Principles of Snow Hydrology." 428.

Dietz, A. J., C. Kuenzer and C. Conrad (2013). "Snow-cover variability in central Asia between 2000 and 2011 derived from improved MODIS daily snow-cover products." International journal of remote sensing 34(11): 3879-3902.

Dietz, A. J., C. Wohner and C. Kuenzer (2012). "European Snow Cover Characteristics between 2000 and 2011 Derived from Improved MODIS Daily Snow Cover Products." Remote Sensing 4(12): 2432-2454.

Dingman, S. L., D. M. Seely-Reynolds and R. C. Reynolds III (1988). "Application of kriging to estimating mean annual precipitation in a region of orographic influence 1." JAWRA Journal of the American Water Resources Association 24(2): 329-339.

Dozier, J. (1989). "Spectral signature of alpine snow cover from the landsat thematic mapper." Remote Sensing of Environment 28: 9-22.

Dozier, J., E. H. Bair and R. E. Davis (2016). "Estimating the spatial distribution of snow water equivalent in the world's mountains." Wiley Interdisciplinary Reviews: Water 3(3): 461-474.

Dozier, J. and T. H. Painter (2004). "Multispectral and Hyperspectral Remote Sensing of Alpine Snow Properties." Annual Review of Earth and Planetary Sciences 32(1): 465-494.

Draper, N. R. and H. Smith (1998). Applied regression analysis 3rd edition, John Wiley & Sons, Inc.

Dressler, K. A., G. H. Leavesley, R. C. Bales and S. R. Fassnacht (2006). "Evaluation of gridded snow water equivalent and satellite snow cover products for mountain basins in a hydrologic model." Hydrological Processes 20(4): 673-688.

Duethmann, D., J. Peters, T. Blume, S. Vorogushyn and A. Güntner (2014). "The value of satellite-derived snow cover images for calibrating a hydrological model in snow-dominated catchments in Central Asia." Water resources research 50(3): 2002-2021.

Dunn, S. and R. Colohan (1999). "Developing the snow component of a distributed hydrological model: a step-wise approach based on multi-objective analysis." Journal of Hydrology 223(1-2): 1-16.

Eeckman, J., P. Chevallier, A. Boone, L. Neppel, A. De Rouw, F. Delclaux and D. Koirala (2017). "Providing a non-deterministic representation of spatial variability of precipitation in the Everest region." Hydrology and Earth System Sciences 21(9): 4879-4893.

Egli, L., T. Jonas and R. Meister (2009). "Comparison of different automatic methods for estimating snow water equivalent." Cold Regions Science and Technology 57(2-3): 107-115.

Fassnacht, S. R., J. López-Moreno, C. Ma, A. Weber, A. Pfohl, S. Kampf and M. Kappas (2017). "Spatio-temporal snowmelt variability across the headwaters of the Southern Rocky Mountains." Frontiers of Earth Science 11(3): 505-514.

Fassnacht, S. R., H. N. B. Venable , J. Khishigbayar and M. Cherry (2013). "The probability of precipitation as snow derived from daily air temperature for high elevation areas of Colorado, United States."

Fayad, A., S. Gascoin, G. Faour, J. I. López-moreno, L. Drapeau, M. L. Page and R. Escadafal (2017). "Snow hydrology in Mediterranean mountain regions: a review." Journal of Hydrology.

Feiccabrino, J., W. Graff, A. Lundberg, N. Sandström and D. Gustafsson (2015). "Meteorological Knowledge Useful for the Improvement of Snow Rain Separation in Surface Based Models." Hydrology 2(4): 266-288.

Finger, D., F. Pellicciotti, M. Konz, S. Rimkus and P. Burlando (2011). "The value of glacier mass balance, satellite snow cover images, and hourly discharge for improving the performance of a physically based distributed hydrological model." Water Resources Research 47(7).

Follum, M. L., C. W. Downer, J. D. Niemann, S. M. Roylance and C. M. Vuyovich (2015). "A radiation-derived temperature-index snow routine for the GSSHA hydrologic model." Journal of Hydrology 529: 723-736.

Follum, M. L., J. D. Niemann and S. R. Fassnacht (2019). "A comparison of snowmelt-derived streamflow from temperature-index and modified-temperature-index snow models." Hydrological Processes 33(23): 3030-3045.

Franz, K. J., P. Butcher and N. K. Ajami (2010). "Addressing snow model uncertainty for hydrologic prediction." Advances in Water Resources 33(8): 820-832.

Franz, K. J. and L. R. Karsten (2013). "Calibration of a distributed snow model using MODIS snow covered area data." Journal of hydrology 494: 160-175.

Froyland, H. K. (2013). Snow loss on the san francisco peaks: Effects of an elevation gradient on evapo-sublimation. Master of Science, Northern Arizona University.

Gabbi, J., M. Carenzo, F. Pellicciotti, A. Bauder and M. Funk (2014). "A comparison of empirical and physically based glacier surface melt models for long-term simulations of glacier response." Journal of Glaciology 60(224): 1140-1154.

Gafurov, A. and A. Bárdossy (2009). "Cloud removal methodology from MODIS snow cover product." Hydrology and Earth System Sciences 13(7): 1361-1373.

Gao, J., M. W. Williams, X. Fu, G. Wang and T. Gong (2012). "Spatiotemporal distribution of snow in eastern Tibet and the response to climate change." Remote Sensing of Environment 121: 1-9.

Gao, Y., H. Xie, T. Yao and C. Xue (2010). "Integrated assessment on multi-temporal and multi-sensor combinations for reducing cloud obscuration of MODIS snow cover products of the Pacific Northwest USA." Remote Sensing of Environment 114(8): 1662-1675.

Gascoin, S., O. Hagolle, M. Huc, L. Jarlan, J. F. Dejoux, C. Szczypta, R. Marti and R. Sánchez (2015). "A snow cover climatology for the Pyrenees from MODIS snow products." Hydrology and Earth System Sciences 19(5): 2337-2351.

Gascoin, S., S. Lhermitte, C. Kinnard, K. Bortels and G. E. Liston (2013). "Wind effects on snow cover in Pascua-Lama, Dry Andes of Chile." Advances in water resources 55: 25-39.

Ginot, P., C. Kull, M. Schwikowski, U. Schotterer and H. W. Gäggeler (2001). "Effects of postdepositional processes on snow composition of a subtropical glacier (Cerro Tapado, Chilean Andes)." Journal of Geophysical Research: Atmospheres 106(D23): 32375-32386.

Gladkova, I., M. Grossberg, G. Bonev, P. Romanov and F. Shahriar (2012). "Increasing the Accuracy of MODIS/Aqua Snow Product Using Quantitative Image Restoration Technique." IEEE Geoscience and Remote Sensing Letters 9(4): 740-743.

Gottardi, F., C. Obled, J. Gailhard and E. Paquet (2012). "Statistical reanalysis of precipitation fields based on ground network data and weather patterns: Application over French mountains." Journal of Hydrology 432-433: 154-167.

Grünewald, T., Y. Bühler and M. Lehning (2014). "Elevation dependency of mountain snow depth." The Cryosphere 8(6): 2381-2394.

Grünewald, T., M. Schirmer, R. Mott and M. Lehning (2010). "Spatial and temporal variability of snow depth and ablation rates in a small mountain catchment." The Cryosphere 4(2): 215-225.

Gupta, R., A. Ghosh and U. Haritashya (2007). "Empirical relationship between near-IR reflectance of melting seasonal snow and environmental temperature in a Himalayan basin." Remote Sensing of Environment 107(3): 402-413.

Hajhouji, Y., V. Simonneaux, S. Gascoin, Y. Fakir, B. Richard, A. Chehbouni and A. Boudhar (2018). "Modélisation pluie-débit et analyse du régime d'un bassin versant semi-aride sous influence nivale. Cas du bassin versant du Rheraya (Haut Atlas, Maroc)." La Houille Blanche(3): 49-62.

Hall, D. K. and G. A. Riggs (2007). "Accuracy assessment of the MODIS snow products." Hydrological Processes: An International Journal 21(12): 1534-1547.

Hall, D. K. and G. A. Riggs (2016). MODIS/Terra Snow Cover Daily L3 Global 0.05 Deg CMG, Version 6, NASA National Snow and Ice Data Center Distributed Active Archive Center, Boulder, Colorado, USA.

Hall, D. K., G. A. Riggs and V. V. Salomonson (1995). "Development of methods for mapping global snow cover using moderate resolution imaging spectroradiometer data." Remote sensing of Environment 54(2): 127-140.

Hall, D. K., G. A. Riggs, V. V. Salomonson, N. E. DiGirolamo and K. J. Bayr (2002). "MODIS snow-cover products." Remote sensing of Environment 83(1-2): 181-194.

He, Z., J. Parajka, F. Tian and G. Blöschl (2014). "Estimating degree day factors from MODIS for snowmelt runoff modeling." Hydrology & Earth System Sciences Discussions 11(7).

He, Z. H., J. Parajka, F. Q. Tian and G. Blöschl (2014). "Estimating degree-day factors from MODIS for snowmelt runoff modeling." Hydrology and Earth System Sciences 18(12): 4773-4789.

Heidke, P. (1926). "Berechnung des Erfolges und der Güte der Windstärkevorhersagen im Sturmwarnungsdienst." Geografiska Annaler 8(4): 301-349.

Herrero, J. and M. J. Polo (2016). "Evaposublimation from the snow in the Mediterranean mountains of Sierra Nevada (Spain)." The Cryosphere 10(6): 2981-2998.

Herrero, J., M. J. Polo, A. Moñino and M. A. Losada (2009). "An energy balance snowmelt model in a Mediterranean site." Journal of Hydrology 371(1-4): 98-107.

Hock, R. (1998). Modelling of glacier melt and discharge, ETH Zurich.

Hock, R. (1999). "A distributed temperature-index ice-and snowmelt model including potential direct solar radiation." Journal of Glaciology 45: 101-111.

Hock, R. (1999). "A distributed temperature-index ice-and snowmelt model including potential direct solar radiation." Journal of Glaciology 45(149): 101-111.

Hock, R. (1999). "A distributed tetn.perature-index ice- and snowrnelt tn.odel including potential direct solar radiation." Journal of Glaciology 45: 101-111.

Hock, R. (2003). "Temperature index melt modelling in mountain areas." Journal of hydrology 282: 104-115.

Hock, R. (2005). "Glacier melt : a review of processes and their modelling." Progress in Physical Geography 29: 362-391.

Hock, R. and B. Holmgren (2005). "A distributed surface energy-balance model for complex topography and its application to Storglaciaren,Sweden." Journal of glaciology 51: 25-36.

Hock, R. and C. Noetzli (1997). "Areal melt and discharge modelling of StorglacHiren , Sweden." International Glaciological Society 24.

Hock, R. and C. Tijm-Reijmer (2012). "A Mass-Balance, Glacier Runoff and Multi-Layer Snow Model." Program documentation and users manual. University of Alaska Fairbanks and Utrecht University, The Netherlands. Vers 27: 88.

Homan, J. W., C. H. Luce, J. P. McNamara and N. F. Glenn (2011). "Improvement of distributed snowmelt energy balance modeling with MODIS-based NDSI-derived fractional snow-covered area data." Hydrological Processes 25(4): 650-660.

Hublart, P., D. Ruelland, I. G. D. Cortázar-atauri, S. Gascoin, S. Lhermitte and A. Ibacache (2016). "Reliability of lumped hydrological modeling in a semi-arid mountainous catchment facing water-use changes." Hydrology and Earth System Sciences 20: 3691-3717.

Hultstrand, D. M. (2006). Geostatistical methods for estimating snowmelt contribution to the seasonal water balance in an alpine watershed. Master of Science, Colorado State University.

Huss, M., M. Funk and A. Ohmura (2009). "Strong Alpine glacier melt in the 1940s due to enhanced solar radiation." Geophysical Research Letters 36(23).

Jarlan, L., S. Khabba, S. Er-Raki, M. Le Page, L. Hanich, Y. Fakir, O. Merlin, S. Mangiarotti, S. Gascoin, J. Ezzahar, M. H. Kharrou, B. Berjamy, A. Saaïdi, A. Boudhar, A. Benkaddour, N. Laftouhi, J. Abaoui, A. Tavernier, G. Boulet, V. Simonneaux, F. Driouech, M. El Adnani, A. El Fazziki, N. Amenzou, F. Raibi, A. El Mandour, H. Ibouh, V. Le Dantec, F. Habets, Y. Tramblay, B. Mougenot, M. Leblanc, M. El Faïz, L. Drapeau, B. Coudert, O. Hagolle, N. Filali, S. Belaqziz, A. Marchane, C. Szczypta, J. Toumi, A. Diarra, G. Aouade, Y. Hajhouji, H. Nassah, G. Bigeard, J. Chirouze, K. Boukhari, A. Abourida, B. Richard, P. Fanise, M. Kasbani, A. Chakir, M. Zribi, H. Marah, A. Naimi, A. Mokssit, Y. Kerr and R. Escadafal (2015). "Remote sensing of water resources in semi-arid mediterranean areas: the joint international laboratory TREMA." International Journal of Remote Sensing 36: 4879-4917.

Kampf, S. K. and E. E. Richer (2014). "Estimating source regions for snowmelt runoff in a Rocky Mountain basin: tests of a data-based conceptual modeling approach." Hydrological Processes 28(4): 2237-2250.

King, J., C., J. Pomeroy, D. M. Gray, C. Fierz, P. Föhn, R. Harding, R. Jordan, E. Martin and C. Plüss (2008). Snow-atmosphere energy and mass balance. Snow and Climate: Physical Processes, Surface Energy Exchange and Modelling. E. B. Richard L. Armstrong, Cambrige University Press**:** 70-124.

Klein, A. and A. Barnett (2003). "Validation of daily MODIS snow cover maps of the Upper Rio Grande River Basin for the 2000–2001 snow year." Remote Sensing of Environment 86(2): 162-176.

Klemeš, V. (1986). "Operational testing of hydrological simulation

models." Hydrological Sciences Journal 31(1): 13-24.

Knippertz, P., M. Christoph and P. Speth (2003). "Long-term precipitation variability in Morocco and the link to the large-scale circulation in recent and future climates." Meteorology and Atmospheric Physics 83(1-2): 67-88.

Kunkel, K. E. (1989). "Simple procedures for extrapolation of humidity variables in the mountainous western United States." Journal of Climate 2(7): 656-669.

Kustas, W. P. and A. Rango (1994). "A simple energy budget algorithm for the snowmelt runoff model." Water Resources Research 30: 1515-1527.

Lang, H. and L. Braun (1990). "On the information content of air temperature in the context of snow melt estimation." IAHS Publ 190: 347-354.

Lehning, M., I. Völksch, D. Gustafsson, T. A. Nguyen, M. Stähli and M. Zappa (2006). "ALPINE3D: a detailed model of mountain surface processes and its application to snow hydrology." Hydrological Processes 20(10): 2111-2128.

Letsinger, S. L. and G. A. Olyphant (2007). "Distributed energy-balance modeling of snow-cover evolution and melt in rugged terrain: Tobacco Root Mountains, Montana, USA." Journal of Hydrology 336(1-2): 48-60.

Li, L. and J. W. Pomeroy (1997). "Estimates of threshold wind speeds for snow transport using meteorological data." Journal of Applied Meteorology 36(3): 205-213.

Li, X. and M. W. Williams (2008). "Snowmelt runoff modelling in an arid mountain watershed , Tarim Basin , China." Hydrological Processes 22: 3931-3940.

Liang, T., X. Huang, C. Wu, X. Liu, W. Li, Z. Guo and J. Ren (2008). "An application of MODIS data to snow cover monitoring in a pastoral area: A case study in Northern Xinjiang, China." Remote Sensing of Environment 112(4): 1514-1526.

Liston, G. E. (1999). "Interrelationships among snow distribution, snowmelt, and snow cover depletion: Implications for atmospheric, hydrologic, and ecologic modeling." Journal of applied meteorology 38(10): 1474-1487.

Liston, G. E. and K. Elder (2006). "A distributed snow-evolution modeling system (SnowModel)." Journal of Hydrometeorology 7(6): 1259-1276.

Liston, G. E. and K. Elder (2006). "A Distributed Snow-Evolution Modeling System (SnowModel)." JOURNAL OF HYDROMETEOROLOGY 7.

Liston, G. E. and K. Elder (2006). "A meteorological distribution system for high-resolution terrestrial modeling (MicroMet)." Journal of Hydrometeorology 7(2): 217-234.

Liston, G. E., R. B. Haehnel, M. Sturm, C. A. Hiemstra, S. Berezovskaya and R. D. Tabler (2007). "Instruments and Methods Simulating complex snow distributions in windy environments using SnowTran-3D." Journal of glaciology 53: 241-256.

López-Moreno, J. I., S. Gascoin, J. Herrero, E. A. Sproles, M. Pons, E. Alonso-González, L. Hanich, A. Boudhar, K. N. Musselman, N. P. Molotch, J. Sickman and J. Pomeroy (2017). "Different sensitivities of snowpacks to warming in Mediterranean climate mountain areas." Environmental Research Letters 12.

López-Moreno, J. I., S. Goyette and M. Beniston (2009). "Impact of climate change on snowpack in the Pyrenees: Horizontal spatial variability and vertical gradients." Journal of Hydrology 374: 384-396.

López-Moreno, J. I. and M. Stähli (2008). "Statistical analysis of the snow cover variability in a subalpine watershed: Assessing the role of topography and forest interactions." Journal of Hydrology 348(3-4): 379-394.

MacDonell, S., C. Kinnard, T. Mölg, L. Nicholson and J. Abermann (2013). "Meteorological drivers of ablation processes on a cold glacier in the semi-arid Andes of Chile." The Cryosphere 7(5): 1513.

Magand, C., A. Ducharne, N. Le Moine and S. Gascoin (2014). "Introducing Hysteresis in Snow Depletion Curves to Improve the Water Budget of a Land Surface Model in an Alpine Catchment." Journal of Hydrometeorology 15(2): 631-649.

Marchane, A., L. Jarlan, L. Hanich, A. Boudhar, S. Gascoin, A. Tavernier, N. Filali, M. L. Page, O. Hagolle and B. Berjamy (2015). "Assessment of daily MODIS snow cover products to monitor snow cover dynamics over the Moroccan Atlas mountain range." Remote Sensing of Environment 160: 72- 86.

Margulis, S. A., G. Cortés, M. Girotto and M. Durand (2016). "A Landsat-Era Sierra Nevada Snow Reanalysis (1985–2015)." Journal of Hydrometeorology 17(4): 1203-1221.

Marks, D., A. Winstral, M. Reba, J. Pomeroy and M. Kumar (2013). "An evaluation of methods for determining during-storm precipitation phase and the rain/snow transition elevation at the surface in a mountain basin." Advances in Water Resources 55: 98-110.

Marshall, S. and R. J. Oglesby (1994). "An improved snow hydrology for GCMs. Part 1: Snow cover fraction, albedo, grain size, and age." Climate Dynamics 10(1-2): 21-37.

Marti, R., S. Gascoin, E. Berthier, M. de Pinel, T. Houet and D. Laffly (2016). "Mapping snow depth in open alpine terrain from stereo satellite imagery." The Cryosphere 10(4): 1361-1380.

Martinec, J. and A. Rango (1986). "Parameter values for snowmelt runoff modelling." Journal of hydrology 84(3-4): 197-219.

Maurer, E. P., J. D. Rhoads, R. O. Dubayah and D. P. Lettenmaier (2003). "Evaluation of the snow-covered area data product from MODIS." Hydrological Processes 17(1): 59-71.

Mazurkiewicz, A. B., D. G. Callery and J. J. McDonnell (2008). "Assessing the controls of the snow energy balance and water available for runoff in a rain-on-snow environment." Journal of Hydrology 354: 1-14.

McCabe, G. and D. Wolock (1999). "Future snowpack conditions in the western United States derived from general circulation model climate simulations." Journal of the American Water Resources Association 35(1): 473-471,484.

Metsämäki, S. J., S. T. Anttila, H. J. Markus and J. M. Vepsäläinen (2005). "A feasible method for fractional snow cover mapping in boreal zone based on a reflectance model." Remote Sensing of Environment 95(1): 77-95.

Molotch, N. P., M. T. Colee, R. C. Bales and J. Dozier (2005). "Estimating the spatial distribution of snow water equivalent in an alpine basin using binary regression tree models: the impact of digital elevation data and independent variable selection." Hydrological Processes 19(7): 1459-1479.

Moore, R., J. Trubilowicz and J. Buttle (2012). "Prediction of Streamflow Regime and Annual Runoff for Ungauged Basins Using a Distributed Monthly Water Balance Model 1." JAWRA Journal of the American Water Resources Association 48(1): 32-42.

Muñoz, E., J. L. Arumı, D. Rivera, M. Aldo, M. B. Habil and A. César (2012). "Gridded data for a hydrological model in a scarce-data basin." Water Management: 1-10.

Nash, J. E. and J. V. Sutcliffe (1970). "River flow forecasting through conceptual models part I—A discussion of principles." Journal of hydrology 10(3): 282-290.

Nepal, S., P. Krause, W. A. Flügel, M. Fink and C. Fischer (2014). "Understanding the hydrological system dynamics of a glaciated alpine catchment in the Himalayan region using the J2000 hydrological model." Hydrological Processes 28(3): 1329-1344.

Neumann, T. A., M. R. Albert, C. Engel, Z. Courville and F. Perron (2009). "Sublimation rate and the mass-transfer coefficient for snow sublimation." International Journal of Heat and Mass Transfer 52(1-2): 309-315.

Ninyerola, M., X. Pons and J. M. Roure (2000). "A methodological approach of climatological modelling of air temperature and precipitation through GIS techniques." International Journal of Climatology: A Journal of the Royal Meteorological Society 20(14): 1823-1841.

Nolin, A. W. (2010). "Recent advances in remote sensing of seasonal snow." Journal of Glaciology 56(200): 1141-1150.

Notarnicola, C., M. Duguay, N. Moelg, T. Schellenberger, A. Tetzlaff, R. Monsorno, A. Costa, C. Steurer and M. Zebisch (2013). "Snow Cover Maps from MODIS Images at 250 m Resolution, Part 2: Validation." Remote Sensing 5(4): 1568-1587.

Ohumura, A. (2001). "Physical basis for the temperature-based melt-index method." Journal of Applied Meteorology 40: 753-761.

Oke, T. (1987). "Boundary Layer Climates, Methuen & Co." Ltd, London.

Olyphant, G. A. (1984). "Insolation topoclimates and potential ablation in alpine snow accumulation basins: Front Range, Colorado." Water Resources Research 20(4): 491-498.

Painter, T. H., D. F. Berisford, J. W. Boardman, K. J. Bormann, J. S. Deems, F. Gehrke, A. Hedrick, M. Joyce, R. Laidlaw and D. Marks (2016). "The Airborne Snow Observatory: Fusion of scanning lidar, imaging spectrometer, and physically-based modeling for mapping snow water equivalent and snow albedo." Remote Sensing of Environment 184: 139-152.

Painter, T. H., K. Rittger, C. McKenzie, P. Slaughter, R. E. Davis and J. Dozier (2009). "Retrieval of subpixel snow covered area, grain size, and albedo from MODIS." Remote Sensing of Environment 113(4): 868-879.

Parajka, J. and G. Blöschl (2006). "Validation of MODIS snow cover images over Austria." Hydrol. Earth Syst. Sci. 10(5): 679-689.

Parajka, J. and G. Blöschl (2008). "The value of MODIS snow cover data in validating and calibrating conceptual hydrologic models." Journal of Hydrology 358(3-4): 240-258.

Parajka, J. and G. Blöschl (2012). "MODIS-based snow cover products, validation, and hydrologic applications." Multiscale Hydrologic Remote Sensing: Perspectives and Applications, edited by: Chang, N.-B. and Hong, Y.

Paton, F. L., H. R. Maier and G. C. Dandy (2013). "Relative magnitudes of sources of uncertainty in assessing climate change impacts on water supply security for the southern Adelaide water supply system." Water Resources Research 49(3): 1643-1667.

Pellicciotti, F., B. Brock, U. Strasser, P. Burlando, M. Funk and J. Corripio (2005). "An enhanced temperature-index glacier melt model including the shortwave radiation balance : development and testing for Haut Glacier d'Arolla, Switzerland." Journal of Glaciology 51: 573-587.

Pellicciotti, F., J. Helbing, A. Rivera, V. Favier, J. Corripio, J. Araos, J.-E. Sicart and M. Carenzo (2008). "A study of the energy balance and melt regime on Juncal Norte Glacier, semi-arid Andes of central Chile, using melt models of different complexity." Hydrological Processes 22(19): 3980-3997.

Pellicciotti, F., T. Raschle, T. Huerlimann, M. Carenzo and P. Burlando (2011). "Transmission of solar radiation through clouds on melting glaciers : a comparison of parameterizations and their impact on melt modelling." Journal of glaciology 57: 367-381.

Phillips, D. L., J. Dolph and D. Marks (1992). "A comparison of geostatistical procedures for spatial analysis of precipitation in mountainous terrain." Agricultural and forest meteorology 58(1-2): 119-141.

Pimentel, R., J. Herrero and M. J. Polo (2015). "Snow evolution in a semi-arid mountainous area combining snow modelling and Landsat spectral mixture analysis." Proceedings of the International Association of Hydrological Sciences 368: 33-39.

Pimentel, R., J. Herrero and M. J. Polo (2017). "Quantifying Snow Cover Distribution in Semiarid Regions Combining Satellite and Terrestrial Imagery." Remote Sensing 9(10).

Pomeroy, J. and E. Brun (2001). "Physical properties of snow." Snow ecology: An interdisciplinary examination of snow-covered ecosystems: 45-126.

Pomeroy, J., D. Gray, K. Shook, B. Toth, R. Essery, A. Pietroniro and N. Hedstrom (1998). "An evaluation of snow accumulation and ablation processes for land surface modelling." Hydrological Processes 12(15): 2339-2367.

Quick, M. C. and A. Pipes (1977). "U.B.C. WATERSHED MODEL / Le modèle du bassin versant U.C.B." Hydrological Sciences Bulletin 22(1): 153-161.

Raleigh, M. S. and J. D. Lundquist (2012). "Comparing and combining SWE estimates from the SNOW-17 model using PRISM and SWE reconstruction." Water Resources Research 48(1).

Rango, A. and J. Martinec (1995). "REVISITING THE DEGREE-DAY METHOD FOR SNOWMELT COMPUTATIONS1." JAWRA Journal of the American Water Resources Association 31(4): 657-669.

Réveillet, M., S. MacDonell, S. Gascoin, C. Kinnard, S. Lhermitte and N. Schaffer (2020). "Impact of forcing on sublimation simulations for a high mountain catchment in the semiarid Andes." The Cryosphere 14(1): 147-163.

Réveillet, M., C. Vincent, D. Six and A. Rabatel (2017). "Which empirical model is best suited to simulate glacier mass balances?" Journal of Glaciology 63(237): 39-54.

Richard, C. and D. J. Gratton (2001). "The importance of the air temperature variable for the snowmelt runoff modelling using the SRM." Hydrological Processes 15(18): 3357-3370.

Riggs, G. A. and D. K. Hall (2004). Snow mapping with the MODIS Aqua instrument. Proceedings of the 61st Eastern Snow Conference, Portland, ME, USA.

Riggs, G. A. and D. K. Hall (2015). "MODIS Snow Products Collection 6 User Guide."

Riggs, G. A., D. K. Hall and M. O. Román (2015). "VIIRS Snow Cover Algorithm Theoretical Basis Document (ATBD)." NASA VIIRS project document [https://modis-snowice. gsfc. nasa. gov.

Rittger, K., T. H. Painter and J. Dozier (2013). "Assessment of methods for mapping snow cover from MODIS." Advances in Water Resources 51: 367-380.

Rochdane, S., B. Reichert, M. Messouli, A. Babqiqi and M. Y. Khebiza (2012). "Climate Change Impacts on Water Supply and Demand in Rheraya Watershed (Morocco), with Potential Adaptation Strategies." Water 4(4): 28-44.

Roe, G. H. and M. B. Baker (2006). "Microphysical and geometrical controls on the pattern of orographic precipitation." Journal of the Atmospheric Sciences 63(3): 861-880.

Rolland, C. (2003). "Spatial and seasonal variations of air temperature lapse rates in Alpine regions." Journal of Climate 16(7): 1032-1046.

Romanov, P. (2003). "Mapping and monitoring of the snow cover fraction over North America." Journal of Geophysical Research 108(D16).

Salomonson, V. V. and I. Appel (2004). "Estimating fractional snow cover from MODIS using the normalized difference snow index." Remote Sensing of Environment 89(3): 351-360.

Salomonson, V. V. and I. Appel (2006). "Development of the Aqua MODIS NDSI fractional snow cover algorithm and validation results." IEEE Transactions on geoscience and remote sensing 44(7): 1747-1756.

Schneider, C., R. Kilian and M. Glaser (2007). "Energy balance in the ablation zone during the summer season at the Gran Campo Nevado Ice Cap in the Southern Andes." Global and Planetary Change 59: 175-188.

Schulz, O. and C. de Jong (2004). "Snowmelt and sublimation : filed experiments and modelling in the Hight Atlas Mounatains of Morocco " Hydrology and Earth System Sciences 8(6): 1076-1086.

Senzeba, K. T., A. Bhadra and A. Bandyopadhyay (2015). "Snowmelt runoff modelling in data scarce Nuranang catchment of eastern Himalayan region." Remote Sensing Applications: Society and Environment 1: 20-35.

Singh, P. (2001). Snow and glacier hydrology, Springer Science & Business Media.

Singh, P. and L. Bengtsson (2003). "Effect of warmer climate on the depletion of snow-covered area in the Satluj basin in the western Himalayan region." Hydrological Sciences Journal 48(3): 413-425.

Singh, P. and S. K. Jain (2003). "Modelling of streamflow and its components for a large Himalayan basin with predominant snowmelt yields." Hydrological Sciences Journal 48(2): 257-276.

Singh, P. and S. K. Jain (2003). "Modelling of streamflow and its components for a large Himalayan basin with predominant snowmelt yields." Hydrological Sciences Journal 48: 257-276.

Song, K., Y. Zhang, C. Jin, S. Yan and L. S. Chiu (2008). "Seasonal Snow Monitoring in Northeast China Using Space-borne Sensors: Preliminary Results." Annals of GIS 14(2): 113-119.

Tarboton, D. G. and C. H. Luce (1996). Utah Energy Balance Snow Accumulation and Melt Model (UEB). Utah Water Research Laboratory Utah State University.

Tekeli, A. E., Z. Akyürek, A. Arda Şorman, A. Şensoy and A. Ünal Şorman (2005). "Using MODIS snow cover maps in modeling snowmelt runoff process in the eastern part of Turkey." Remote Sensing of Environment 97(2): 216-230.

Tekeli, A. E., Z. Akyürek, A. Şensoy, A. A. Şorman and A. Ü. Şorman (2005). "Modelling the temporal variation in snow-covered area derived from satellite images for simulating/forecasting of snowmelt runoff in Turkey/Modélisation de la variation temporelle de la surface enneigée à partir d'images satellitaires pour la simulation/prévision de l'écoulement de fonte nivale en Turquie." Hydrological Sciences Journal 50(4).

Tominaga, Y., T. Okaze and A. Mochida (2011). "CFD modeling of snowdrift around a building: An overview of models and evaluation of a new approach." Building and Environment 46(4): 899-910.

Verseghy, D. L. (1991). "Class-A canadian land surface scheme for GCMS. I. Soil model." International Journal of Climatology 11: 111-133.

Vicente-Serrano, S. M., M. A. Saz-Sánchez and J. M. Cuadrat (2003). "Comparative analysis of interpolation methods in the middle Ebro Valley (Spain): application to annual precipitation and temperature." Climate research 24(2): 161-180.

Vicuña, S., R. D. Garreaud and J. McPhee (2011). "Climate change impacts on the hydrology of a snowmelt driven basin in semiarid Chile." Climatic Change 105(3-4): 469-488.

Vincent, C. (2002). "Influence of climate change over the 20th Century on four French glacier mass balances." Journal of Geophysical Research 107(D19).

Viviroli, D. and R. Weingartner (2008). "Water Towers"—A Global View of the Hydrological Importance of Mountains. Mountains: Sources of Water, Sources of Knowledge. E. Wiegandt. Dordrecht, Springer Netherlands: 15-20.

Vögeli, C., M. Lehning, N. Wever and M. Bavay (2016). "Scaling Precipitation Input to Spatially Distributed Hydrological Models by Measured Snow Distribution." Frontiers in Earth Science 4(108).

Wagener, T., N. McIntyre, M. J. Lees, H. S. Wheater and H. V. Gupta (2003). "Towards reduced uncertainty in conceptual rainfall-runoff modelling: dynamic identifiability analysis." Hydrological Processes 17(2): 455-476.

Wang, X. and H. Xie (2009). "New methods for studying the spatiotemporal variation of snow cover based on combination products of MODIS Terra and Aqua." Journal of Hydrology 371(1-4): 192-200.

Wang, X., H. Xie and T. Liang (2008). "Evaluation of MODIS snow cover and cloud mask and its application in Northern Xinjiang, China." Remote Sensing of Environment 112(4): 1497-1513.

Warren, S. G. (1982). "Ice and climate modeling: An editorial essay." Climatic Change 4(4): 329-340.

Willis, I. C., N. S. Arnold and B. W. Brock (2002). "Effect of snowpack removal on energy balance , melt and runoff in a small supraglacial catchment." Hydrlogical processes 16: 2721-2749.

Willis, I. C., M. J. Sharp and K. S. Richards (1991). "Studies of the water balance of Midtdalsbreen, Hardangerjökulen, Norway." Zeitschrift für Gletscherkunde und Glazialgeologie 27: 117-138.

Xiao, X., Q. Zhang, S. Boles, M. Rawlins and B. Moore (2004). "Mapping snow cover in the pan-Arctic zone, using multi-year (1998-2001) images from optical VEGETATION sensor." International Journal of Remote Sensing 25(24): 5731-5744.

Xie, H., X. Wang and T. Liang (2009). "Development and assessment of combined Terra and Aqua snow cover products in Colorado Plateau, USA and northern Xinjiang, China." Journal of Applied Remote Sensing 3(1): 033559.

Yasutomi, N., A. Hamada and A. Yatagai (2011). "Development of a long-term daily gridded temperature dataset and its application to rain/snow discrimination of daily precipitation." Global Environmental Research 15(2): 165-172.

Yin, D., X. Cao, X. Chen, Y. Shao and J. Chen (2013). "Comparison of automatic thresholding methods for snow-cover mapping using Landsat TM imagery." International Journal of Remote Sensing 34(19): 6529-6538.

Zappa, M. (2008). "Objective quantitative spatial verification of distributed snow cover simulations—an experiment for the whole of Switzerland / Vérification quantitative spatiale objective de simulations distribuées de la couche de neige—une étude pour l'ensemble de la Suisse." Hydrological Sciences Journal 53(1): 179-191.

Zaramella, M., M. Borga, D. Zoccatelli and L. Carturan (2019). "TOPMELT 1.0: a topography-based distribution function approach to snowmelt simulation for hydrological modelling at basin scale." Geoscientific Model Development 12(12): 5251-5265.

Zhang, F., H. Zhang, S. C. Hagen, M. Ye, D. Wang, D. Gui, C. Zeng, L. Tian and J. Liu (2013). "Snow cover and runoff modelling in a high mountain catchment with scarce data: effects of temperature and precipitation parameters." Hydrological Processes 29(1): 52-65.

Zhang, H., F. Zhang, G. Zhang, T. Che, W. Yan, M. Ye and N. Ma (2019). "Ground-based evaluation of MODIS snow cover product V6 across China: Implications for the selection of NDSI threshold." Sci Total Environ 651(Pt 2): 2712-2726.

Zhang, Y., S. Yan and Y. Lu (2010). "Snow Cover Monitoring Using MODIS Data in Liaoning Province, Northeastern China." Remote Sensing 2(3): 777-793.

Zhou, H., E. Aizen and V. Aizen (2013). "Deriving long term snow cover extent dataset from AVHRR and MODIS data: Central Asia case study." Remote Sensing of Environment 136: 146-162.

Zuzel, J. F. and L. M. Cox (1975). "Relative importance of meteorological variables in snowmelt." Water Resources Research 11: 174-176.

APPENDIX

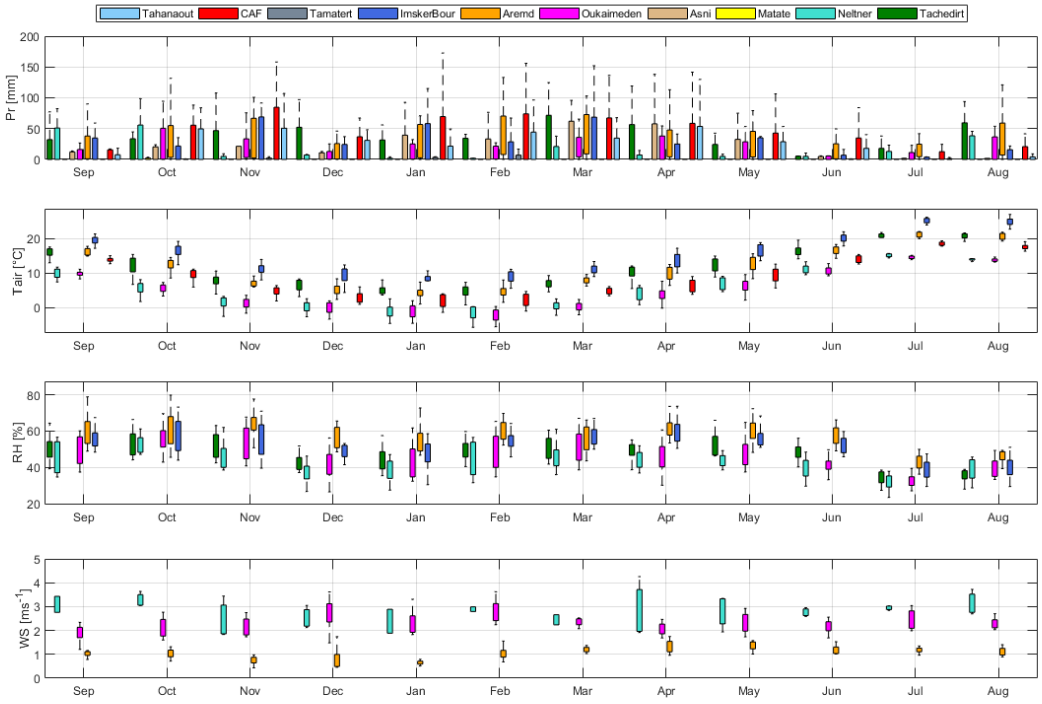

Figure 44: Inter-annual mean monthly meteorological variables available in all stations at Rheraya watershed starting from 2001 to 2016

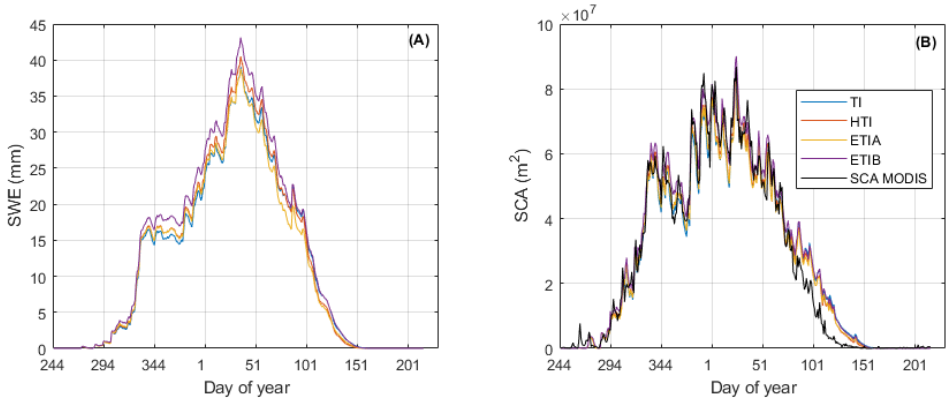

Figure 45: Daily mean variability of simulated SWE and SCA over all the period 2003-2016 in Rheraya

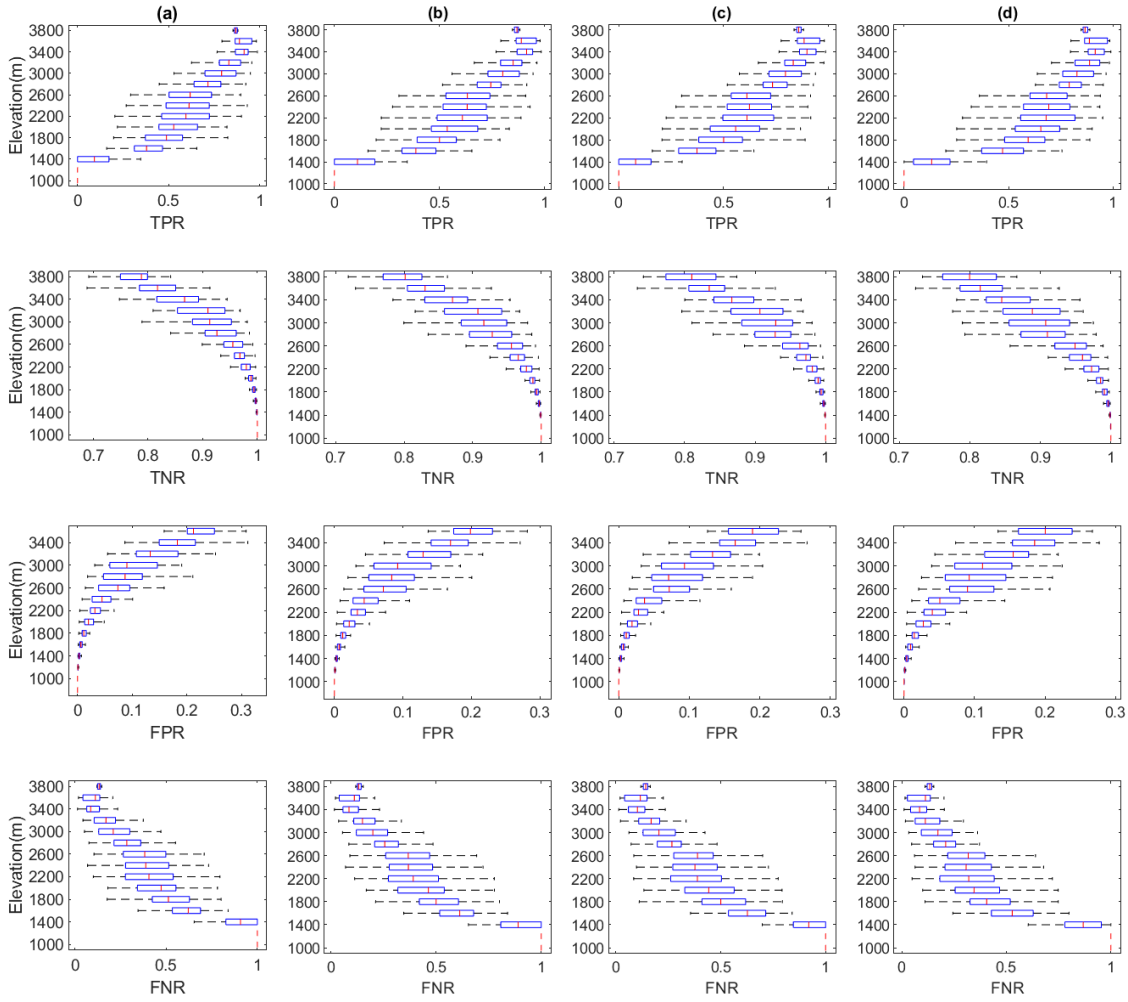

Figure 46: Rates of confusion matrix per elevation range in Rheraya watershed. TPR (True positive rate), TNR (true positive rate), FPR (false positive rate) FNR (false-negative rate). (a) TI, (b) HTI, (c) ETI-A, and (d) ETI-B model.

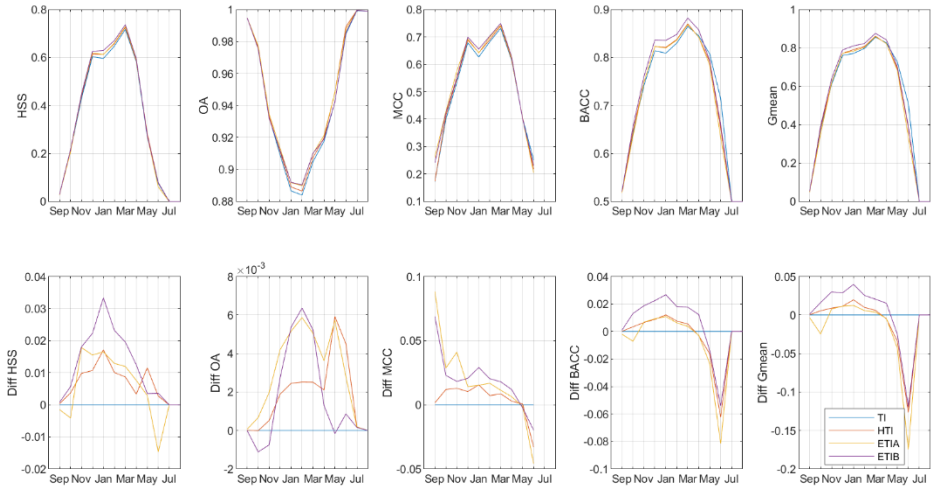

Figure 47: Global classification metrics assessing spatial model performances over Rheraya basin

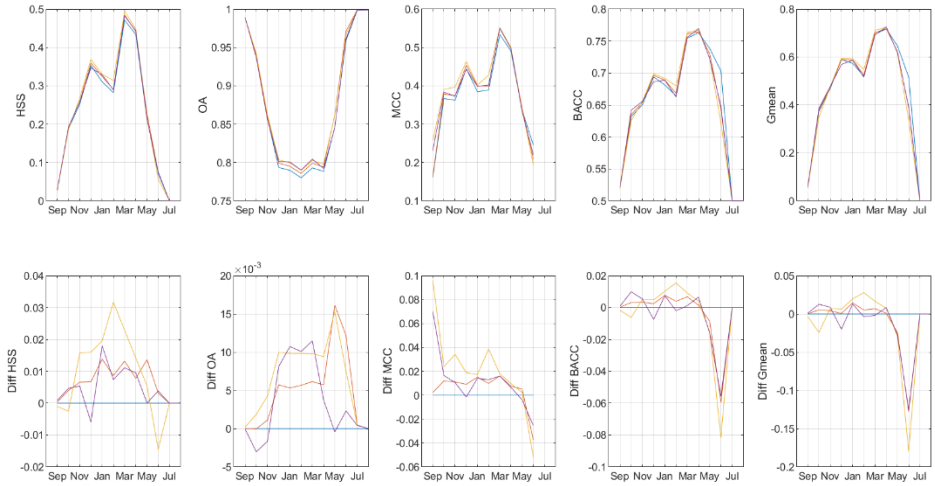

Figure 48: Global classification metrics assessing spatial model performances over higher elevation (Z>2500m) in Rheraya basin

Table 16: Instrumentation at the OukaimdenSM weather station and their specifications (2003–2010) given by (Boudhar et al. 2016)

Quantity	Instrument type	Measurement range	Period
Air temperature, (°C)	Vaissala HMP45C	(-40°C to 60°C)	2003-2010
Humidity, (%)	Vaissala HM45C	0% to 100%	2003-2010
Rain, (mm)	Pluviometer TE525WS-L	Infinite in increments of tip (least count) of rainfall.	2003-2010
Precipitation, (mm)	Geonor T-200B	600 mm	2009-2010
SWR INCI , (W m^{-2})	CNR1 Kipp & Zonen	$0.305< \lambda <2.8$ µm	2009-2010
SWR REFL, (W m^{-2})	CNR1 Kipp & Zonen	$0.305< \lambda <2.8$ µm	2009-2010
LWR INCI, (W m^{-2})	CNR1 Kipp & Zonen	$5< \lambda < 50$ µm	2009-2010
LWR REFL, (W m^{-2})	CNR1 Kipp & Zonen	$5< \lambda < 50$ µm	2009-2010
Snow depth, (cm)	Sonic CR50	0.5 to 10 m	2003-2010
SWR INCI, (W m^{-2})	Pyranometer Skye	$0.4 < \lambda <1.1$ µm	2003-2009
SWR REFL, (W m^{-2})	Pyranometer Skye	$0.4 < \lambda <1.1$ µm	2004-2005; 2008-2009
Surface temperature (°C)	SI-111 Infrared Radiometer	(-40°C to 70°C)	2008-2009
Wind speed (m s^{-1})	Anémomètre A100R	0-45 m s^{-1}	2003-2009

Table 17: All climatic parameters recorded in Rheraya weather stations

Stations	Sensors	Parameters	Availability	Pas de temps	Type	Elevation (m)	X	Y
Aremd	Aremd_M_ITair_(°C)	Température	From 21/01/2003 to 25/12/2016	30 min	AWS	1940	259296	61946
	Aremd_M_IRg_(W/m2)	Rayonnement global						
	Aremd_M_IHr_(%)	Humidité relative						
	Aremd_M_IDv_(°)	Direction du vent						
	Aremd_M_IVv_(m/s)	Vitesse du vent						
	Aremd_P_IP30m_(mm)	Pluie 30 minutes						
Asni	Asni_P_IP30m_(mm)	Pluie 30 minutes	From 07/01/2004 to 10/01/2017	30 min	pluviographe	1170	254025	75869
Imskerbour	Imskerbour_M_ITair_(°C)	Température	From 10/05/2007 to 27/04/2016	30 min	pluviographe + T+HR	1404	257883	70991
	Imskerbour_M_IHr_(%)	Humidité relative						
	Imskerbour_P_IP30m_(mm)	Pluie 30 minutes						
Neltner	Neltner_M_IDv_(°)	Direction du vent	From 27/07/2007 to 29/10/2016	30 min	pluviographe + T+HR	3207	257543	55355
	Neltner_M_IHr_(%)	Humidité relative						
	Neltner_M_ITair_(°C)	Température						
	Neltner_M_IVv_(m/s)	Vitesse du vent						
	Neltner_P_IGecm_(mm)	Précipitations géonor en cm						
	Neltner_P_IP30m_(mm)	Pluie 30 minutes						
Oukaimeden-SM	Oukaimeden_M_IDv_(°)	Direction du vent	From 04/11/2009 to 06/12/2016	30 min	AWS	3230	264837	68057
	Oukaimeden_M_IG3d_(W/m2)	Longue longueur d'onde réfléchie non corrigé						
	Oukaimeden_M_IG3dc_(W/m2)	Longue longueur d'onde réfléchie corrigé						
	Oukaimeden_M_IG3u_(W/m2)	Longue longueur d'onde incidente non corrigée						
	Oukaimeden_M_IG3uc_(W/m2)	Longue longueur d'onde incidente corrigé						
	Oukaimeden_M_IHr_(%)	Humidité relative						
	Oukaimeden_M_IM3d_(W/m2)	courte longueur d'onde réfléchie						
	Oukaimeden_M_IM3u_(W/m2)	Courte longueur d'onde incidente						
	Oukaimeden_M_IRg_(W/m2)	Rayonnement global						

	Oukaimeden_M_ISav_(m)	Hauteur de neige moyenne						
	Oukaimeden_M_ITair_(°C)	Température						
	Oukaimeden_M_Ivmx_(m/s)	Direction du vent max						
	Oukaimeden_M_IVv_(m/s)	Vitesse du vent						
	Oukaimeden_P_IGecm_(mm)	Précipitations géonor en cm						
	Oukaimeden_P_IGemm_(mm)	Précipitations géonor en mm						
	Oukaimeden_P_IP30m_(mm)	Pluie 30 minutes						
	Tachedert_P_IP30m_(mm)	Pluie 30 minutes						
Tachedert	Tachedert_M_ITair_(°C)	Température	From 12/05/2007 to 03/07/2016	30 min	pluviographe + T+HR	2343	266678	65228
	Tachedert_M_IHr_(%)	Humidité relative						
Tamatarte	Tamatarte_Pluie H(mm)	Pluie horaire (1heure)	From 13/10/2012 to 03/07/2016	1heure	Pluviomètre	1924	261029	63911
Matate	Matate_Pluie_H(mm)	Pluie horaire (1heure)	From 12/10/2012 to 13/10/2015	1heure	Pluviomètre	1825	257242	65656
Tahnaout	Tahanaout_P_JABHT(mm)	Pluie journalière (1 jour)	From 01/09/1971 to 31/12/2009	1 jour	Pluviomètre	1064	255900	80400
	Tahanaout_D_JABHT(m3/s)	Débit journalière (1 jour)	From 01/03/1962 to 31/08/2009	1 jour	Débimètre			
CAF	Température journalière(°C)	Température maximale (1 jour)	From 10/03/1988 to 05/12/2009	1 jour	pluviographe + T	2612	265309	70830
	Température journalière min (°C	Température minimale (1 jour)	From 10/03/1988 to 05/12/2009	1 jour				
	Neige équivalent eau journalier_(mm)	Neige (mm) (1 jour)	From 10/03/1988 to 15/06/2011	1 jour				
	Pluie journalière_(mm)	Pluie journalière (1 jour)	From 10/03/1988 to 15/06/2011	1 jour				